Vortex Phenomena in Unconventional Superconductors

Curran, Peter

Award date:
2013

Awarding institution:
University of Bath

Vortex Phenomena in Unconventional Superconductors

submitted by

Peter John Curran

for the degree of Doctor of Philosophy

of the

University of Bath

Department of Physics

December 2012

Abstract

Unconventional superconductors are those which are not described by the BCS theory, and for which no known theoretical description currently exists. The careful study of the behaviour of superconducting vortices in such systems yields crucial insights into the underlying physics of these exciting materials. This thesis describes a series of magnetometry experiments conducted on three different unconventional superconductors: Sr_2RuO_4, MgB_2 and $Bi_2Sr_2CaCu_2O_{8+\delta}$; utilising two techniques: Scanning Hall probe microscopy and magneto-optical imaging.

An exotic p-wave chiral order parameter is thought to exist in Sr_2RuO_4 and is expected to produce several identifiable magnetic signatures. A search for these signals via scanning Hall probe measurements failed to detect any such signatures, but did capture a structural transition of the vortex lattice that is consistent with the proposed chiral order parameter. Studies of several samples also suggest that the vortex behaviour is strongly modified with even tiny amounts of disorder, a conclusion that has important consequences for interpretations of vortex patterns in Sr_2RuO_4.

Several recent experiments have reported vortex configurations consistent with a competing short-range repulsion and long-range attraction in the inter-vortex interaction in MgB_2 single crystals. We observe the spontaneous formation of vortex chains and labyrinths in a 160nm MgB_2 thin-film that are suggestive of a non-monotonic vortex interaction, but perhaps more indicative of an intermediate-range attraction in harness with short and long-range repulsions. The suitability of seven potential mechanisms of vortex attraction in MgB_2 are reviewed in light of the unusually short electronic mean-free path of our sample.

Finally, magneto-optical imaging has been used to study the penetration of flux into regular polygon-shaped $Bi_2Sr_2CaCu_2O_{8+\delta}$ platelets with various geometries. The variation of H_P with geometry qualitatively contradicts conventional estimates of demagnetisation factors based on equivalent ellipsoids using inscribed circles. This work has important implications for the estimation of appropriate effective demagnetisation factors in arbitrarily shaped superconducting bodies.

Contents

Acknowledgements

The research conducted over the last three and a half years and presented in this thesis would not have been possible without the help and support of many people. Firstly I would like to thank the technical staff at the University of Bath, Department of Physics, who seemed to know the solutions to my many problems before they arose, and demonstrated admirable patience and perseverance in helping me overcome them.

Harry Bone, Simon Dodd, Bob Draper, Cathy Dyer, Adrian Hooper, Wendy Lambson, Spartaco Landi, Paul Reddish, Sivapathasundaram Sivaraya (Electrical Engineering), Peter Sykes, Stephen Wedge.

Secondly I would like to thank several postdoctoral researchers and PhD students within the Nanoscience group, some of whom have since moved on, who helped smooth my learning curve in the early stages of my PhD, as I burdened them with many hours of equipment training and scientific discussions.

Malcolm Connolly, Sara Dale, Miles Engbarth, Andriy Moskalenko, Andre Mueller.

And finally, I would like to thank my supervisor, Professor Simon Bending, for constantly providing instant support and expert guidance throughout my PhD, which, along with the neccessary space to learn from my own mistakes and develop my own ideas, has helped me become a better scientist.

Chapter 1

Overview

1.1 Motivation

In the late 19^{th}, early 20^{th} century, the scientific understanding of the mechanism behind electrical conductivity was incomplete. It was well established that electrical resistance fell with temperature[1] but the question as to how this trend continued far below room temperature remained open and extremely important. In 1908 the Dutch physicist Heike Kamerlingh Onnes succeeded in liquefying Helium [2], the last remaining natural gas to be condensed, and so opened up a new temperature range in the vicinity of absolute zero. The investigation of electrical conduction at these temperatures (c.a. 1K) was expected to yield one of three potential results:

1. Resistance would fall continuously to zero with temperature.
2. Resistance would fall but reach a non-zero minimum, possibly determined by sample purity.
3. Resistance would tend to infinity as temperature approached zero, reflecting the hypothesis that all electrons would be bound to their atoms.

Onnes' initial experiments on Gold and Platinum at liquid Helium temperature immediately affirmed hypothesis 2. Driven to find purer and purer samples, Onnes next chose Mercury, an element that he could purify through a process of multiple distillation. It was during these measurements on Mercury that Onnes

first witnessed the absence of all electrical resistance (within the resolution of the experimental setup). This was an effect not in itself altogether surprising due to the high purity of his sample, but remarkable for the fact that the transition took place in a very sharp jump, over a few hundredths of a degree and not in a steady gradual reduction proposed by the existing vibrational theory. This dramatic sudden fall in resistance at a critical temperature, T_c suggested a change in state had taken place and led Onnes to dub this phenomenon: The Superconducting State.

The subsequent years saw an explosion of research into this field and the remainder of the 20^{th} century was littered with major successes, most notably in the development of the London, Ginzburg-Landau and BCS theories (discussed later) and more recently with the discovery (1986) of the so called High Temperature Superconductors (HTS). HTS are materials that remain superconducting at temperatures (in some cases) in excess of 77K, the boiling point of Nitrogen, and hence, due to the much lower costs associated with liquefying Nitrogen, constituted a major leap forward towards the widespread commercial exploitation of superconductors.

As of today, superconductors have a variety of applications in society, most notably in the generation of extremely large, stable and uniform magnetic fields utilised in: Magnetic Resonance Imaging scanners, high energy particle colliders and magnetic levitation trains. In addition to uses stemming from powerful magnetic fields, the list of applications continues with ultra-efficient electric generators, highly sensitive flux sensing devices for biomagnetic applications, high frequency filters in use in the mobile phone industry, magnetic sorters in recycling centres and superconducting x-ray and light detectors in use in the space industry.

One major obstacle to further applications is the economic expense associated with cooling superconductors below their critical temperature. This makes ventures such as lossless transmission lines commercially challenging. HTS promised a solution to this problem, but the complicated growth techniques and highly anisotropic crystalline structure makes them somewhat unsuitable for flexible wires and circuitry etc. Early theoretical descriptions were remarkably successful in explaining many facets of the observed behaviour. However, many problems remain unsolved. For example, although HTS are in widespread use, a complete

description of the mechanism behind superconductivity remains elusive. Further developments in the field have been steady but new superconductors are being serendipitously discovered, rather than following the more desireable process of prediction and fabrication. In order to make scientific progress towards more widespread applications throughout society, a more complete understanding of the physics behind superconductivity is required.

The direct imaging of vortex matter (c.f.2.5) in superconductors provides an extremely fertile ground for probing and testing current theories and, as such, is a useful tool for developing them further towards a complete physical description of the superconducting state. Observations of the penetration of flux into carefully fabricated mesoscopic samples allows systematic study of the interplay of surface/energy barriers, and demagnetizing effects, that together control flux entry. Once flux is inside a sample, the search for *unconventional* vortex behaviour can lead to important insights into the underlying symmetry of the superconducting order parameter, (knowledge of which is crucial for attempts to develop a theoretical binding mechanism) and also speak for radical new theories of superconductivity.

The focus of this PhD thesis is to observe and understand vortex behaviour and elucidate clues that will hopefully unlock the mechanisms behind superconductivity and pave the way for designer materials, materials whose propeties can be predicted beforehand, and subsequently engineered to meet specific needs.

1.2 Structure

This thesis describes the experimental research into superconductivity conducted between September 2008 and September 2012, predominantly at the University of Bath, but also partly at the University of Tokyo, and wholly under the supervision of Professor Simon Bending. Chapter 2 introduces the fundamentals of superconducting theory, a continuation of, and overlapping with, material that is commonly found on undergraduate physics programmes. This section is by no means exhaustive but aims to provide a solid base from which to provide a suitable context for the experimental results that follow. Chapter 3 describes the experimental techniques used in the acquisition of this data. Chapters 4, 5 and 6 contain the experimental results and analysis from multiple experiments,

involving three different materials and can be read as stand-alone sections. The general theory introduced in chapter 2 is relevant to all three, but further specific theory required for an understanding of each experiment is contained at the start of each experimental chapter. Each experimental chapter also contains its own conclusion but a more general summary of the research, and ideas for further extensions of this work are contained in chapter 7 which closes the thesis.

Chapter 2

Introduction to Superconductivity

Superconductivity is characterised by two distinct electrodynamic phenomena. The first is *zero resistance* below a certain critical temperature (T_c), first observed in mercury by Onnes in 1911 [2]. Onnes went on to discover the same effect in Tin and Lead at T_cs that were characteristic for each material. Indeed, in the subsequent years hundreds of materials have been found to superconduct; elemental, alloy and more exotic crystalline structures, each with its own unique T_c. The normal state ($T>T_c$) behaviour of a material can not be relied upon as an indicator of its ability to superconduct. Copper and gold for instance, both excellent electrical conductors don't superconduct at all.

It was some years later in 1933 that the second characteristic of superconductivity, *perfect diamagnetism*, was discovered by Meissner and Oschenfeld [3]. That is the ability of a superconductor to completely expel the magnetic flux of an applied external field from its interior up to a certain critical field. This exclusion occurs regardless of whether the field is applied before or after cooling; which is a non-trivial distinction. If the field is applied *after* cooling below T_c, then one would expect the creation of induction currents as the field is switched on, set up so as to produce a field equal and opposite to the external one in accordance with Lenz's law. These currents would continue to flow as persistent currents due to the condition that R=0, and hence the expulsion could be viewed as simply a phenomenon of zero resistance. However, if the field is switched on *before* cooling below T_c, there is no reason for the creation of persistent currents and one now

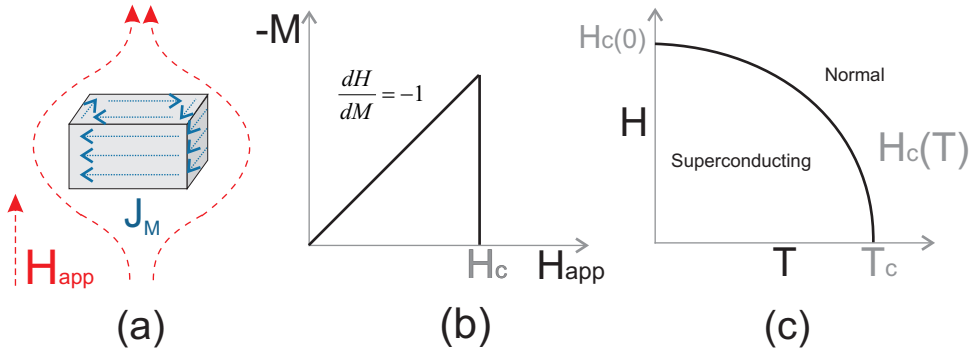

Figure 2-1: (a) The Meissner Effect in Type-I superconductors. All magnetic flux is expelled from the interior of the Superconducting sample by a spontaneous Meissner current (J_M) that flows on the surface of the sample. The magnetic induction (B) is forced to distort and curve around the superconducting sample. (b) The perfect diamagnetism ($\chi = -1$) survives up to a critical value of external field (H_c), when superconductivity is abruptly destroyed and the sample is driven normal. (c) The empirically obtained temperature dependence of H_c.

realises it is an entirely independent effect. This is called the Meissner effect and is illustrated in figure 2-1. Empirically, H_c has been found to display the temperature dependence shown by the curve in 2-1(c) and described to a good approximation by equation 2.1 below.

$$H_c(T) = H_c(0)\left[1 - \left(\frac{T}{T_c}\right)^2\right]. \tag{2.1}$$

Outside the Meissner regime, the state of a superconducting material depends on its thermodynamic path. It's existence suggests that flux exclusion is a true thermodynamic state and therefore allows the application of equilibrium thermodynamics to the superconducting phase transition.

Any material that acquires a magnetisation (M) in the presence of an applied field (H_a) changes its Helmholtz free energy density (f) by

$$f(H_a) = -\mu_0 \int_0^{H_a} M dH. \tag{2.2}$$

Therefore, for a superconductor in the Meissner state, ($\mathbf{M} = -\mathbf{H_a}$) f is given by

$$f(H_a) = \frac{1}{2}\mu_0 H_a^2. \tag{2.3}$$

At the thermodynamic critical field H_c, the magnetic energy per unit volume of the spontaneous internal magnetisation $f(H_a)$ exactly equals the difference in energy between the superconducting (f_s) and normal (f_n) states and is known as the condensation energy of superconductivity.

$$f_n - f_s = \frac{1}{2}\mu_0 H_c^2. \tag{2.4}$$

2.1 London Equations

The first phenomenological theoretical description of the Meissner effect emerged in 1935 as a result of the combined efforts of the London brothers [4]. They realised that the currents responsible for the Meissner effect don't emerge naturally from Maxwell's equations so set about altering them. Starting from the postulate that a certain density (n_s) of electrons in a superconductor experience zero scattering ($R = 0$), the microscopic force equation loses its dissipative term and becomes

$$m\frac{dv_s}{dt} = eE. \tag{2.5}$$

Here m and e are electronic mass and charge respectively, v_s is the super-electron velocity and E is the electric field. Combining equation 2.5 with the supercurrent density, $J_s = n_s e v_s$, we arrive at the first London equation

$$\frac{dJ_s}{dt} = \frac{n_s e^2}{m}E. \tag{2.6}$$

This equation unsurprisingly yields the expected consequence of infinite conductivity; an applied electric field produces a constant linear acceleration of the superconducting charge carriers. We progress towards the second London equation (eqn 2.10), and a description of the Meissner effect, by successively substituting 2.6 into Maxwell III (equation 2.7) and Maxwell IV (equation 2.8) to arrive at the result shown in equation 2.9.

$$\nabla \times \mathbf{E} = -\frac{\partial \mathbf{B}}{\partial t} \tag{2.7}$$

$$\nabla \times \mathbf{B} = \mu_0 \mathbf{J_s}, assuming\, (\mathbf{J_s} \gg \partial \mathbf{D}/\partial t) \tag{2.8}$$

$$\frac{\partial \mathbf{B}}{\partial t} = \frac{m}{\mu_0 n_s e^2} \nabla^2 \frac{\partial \mathbf{B}}{\partial t} \tag{2.9}$$

It was the London brothers central conjecture that the same equation (2.9) applies to $\mathbf{B}$(x) and so they postulated their second equation,

$$\nabla^2 \mathbf{B} = \frac{\mathbf{B}}{\lambda_L^2}, \tag{2.10}$$

where,

$$\lambda_L = \sqrt{\frac{m}{\mu_0 n_s e^2}} \tag{2.11}$$

To appreciate the consequences of this equation, it helps to first solve it for a simple geometry. By considering a superconductor that extends infinitely in x and z, with a superconducting/normal boundary at $y = 0$, in an applied field $\mathbf{B_a} = B_a \hat{z}$, equation 2.10 reduces to:

$$\frac{\partial^2 B_z}{\partial y^2} = \frac{B_z(y)}{\lambda_L^2} \tag{2.12}$$

Which has the solution:

$$B_z(y) = B_a e^{-\frac{y}{\lambda_L}} \tag{2.13}$$

Taking a closer look we now notice that λ_L has dimensions of length. Hence, rather than being completely screened, external applied magnetic fields decay into the superconductor over this characteristic lengthscale, λ_L, which is known as the *London penetration depth*. A visual representation of λ_L is given in figure 2-2. By inserting 2.13 into Maxwell IV (equation 2.8) we can define the resulting supercurrent:

$$J_s(y) = \frac{B_a}{\mu_0 \lambda_L} e^{-\frac{y}{\lambda_L}} \hat{x} \tag{2.14}$$

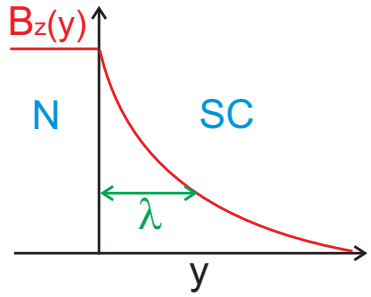

Figure 2-2: A normal/superconducting boundary (y=0) in the presence of an applied external magnetic field. The field decays into the superconductor over a characteristic lengthscale λ_L known as the London penetration depth. Ensuing supercurrents flowing in this surface layer generate an internal magnetisation that opposes and expels the applied field from the centre of the sample, a phenomenon known as the Meissner effect.

Equation 2.14 tells us that the internal magnetisation opposing and expelling the applied external field is generated by screening currents that flow in this surface layer. In other words, the Meissner effect arises naturally out of the London equations.

2.2 Ginzburg-Landau Theory

Although highly successful in describing the spatial variation of magnetic flux in a superconductor, the London equations fail to consider the spatial variation of the superconducting charge carriers (n_s) over a sample. Among other work, the detailed investigations of the magnetic state of a sphere in 1947 [5] brought this shortcoming to the fore when they revealed complex normal/superconducting domain formation in applied fields near H_c, giving a clear indication that n_s is varying spatially. The situation where normal regions coexist side by side with superconducting ones has since been intensively studied and is known as the *intermediate state*. The Ginzburg-Landau (GL) theory [6] addressed this inadequacy when it was published in 1950. Regarded as an outstanding success today, enthusiasm for GL theory was slow to catch on due to its phenomenological origins.

Quite separate to superconductivity, Lev landau had been developing a theory of 2nd order phase transitions in the early to mid-20th century. The theory intro-

duced two key concepts. The first was an *order parameter* that characterised the phase transition, and the second was a simple postulated form of an expansion of the free energy of the system, as a function of the order parameter. Originally intended for work on structural transitions it has since been generalised and found to be successful in treating many types of phase transition: Ferromagnetic, ferroelectric etc. The key insight of GL theory was to realise that in superconductivity the order parameter was a macroscopic quantum mechanical "wavefunction" with a maximum at $T = 0$ and varied continously to 0 at $T = T_c$. This implied that the order parameter was complex, and that it varied in space. For superconductivity the order parameter ψ is connected to the density of superconducting charge carriers, $\mathrm{n_s}$, by the following relation,

$$|\psi|^2 = n_s, \tag{2.15}$$

and the Helmholtz free energy of the system (f) is expanded about ψ in the following Taylor series. One of the conditions of Landau's expansion is that it is only valid for very small ψ, i.e. $T \approx T_c$.

$$f(\psi) \approx f(\psi_0) + \frac{df(\psi_0)}{d\psi}(\psi - \psi_0) + \frac{1}{2!}\frac{d^2 f(\psi_0)}{d\psi^2}(\psi - \psi_0)^2 + ... \tag{2.16}$$

Where $\psi_0 = \psi(T_c)$. This expansion is reduced by noting that the free energy at $\mathrm{T_c}$ is simply the energy of the normal state (f_n) and also at $\mathrm{T_c}$, $\psi_0 = 0$.

$$f(\psi) = f_n + \frac{df(0)}{d\psi}\psi + \frac{1}{2!}\frac{d^2 f(0)}{d\psi^2}\psi^2 + ... \tag{2.17}$$

Which we can present in its more recognisable form in equation 2.20 after making the following substitutions and ignoring higher order terms.

$$\alpha(T) = \frac{d^2 f(0)}{d\psi^2} \tag{2.18}$$

$$\beta(T) = \frac{d^4 f(0)}{d\psi^4} \tag{2.19}$$

$$f_s = f_n + \alpha(T)\,|\psi|^2 + \frac{1}{2}\beta(T)\,|\psi|^4 \tag{2.20}$$

For a stable phase at the transition point $f_s(\psi)$ must be a minimum, therefore Landau theory disregards odd powers in the expansion. Substituting 2.15 into 2.20 and minimising the free energy with respect to the density of superconducting charge carriers we arrive at the following definition of n_s.

$$\frac{df_s}{dn_s} = \alpha(T) + \beta(T)n_s = 0, \tag{2.21}$$

$$n_s = -\frac{\alpha(T)}{\beta(T)} \tag{2.22}$$

In order to produce a minimum in energy below T_c the sign of $\alpha(T)$ must change at the transition. In fact a further intricacy of the Landau theory of 2nd order phase transitions was that the coefficients of the energy expansion could be themselves expressed as expansions in powers of (T-T_c), thereby including this requirement as a prerequisite.

The decisive extension of GL theory was to include two additional terms to the expansion shown in 2.20 to arrive at equation 2.25. The first is a 'kinetic energy' term included to account for spatial variations in the order parameter ($\psi(r)$). As mentioned GL theory assumes that the order parameter for superconductivity is a macroscopic wavefunction. Following this assumption further we notice that the kinetic energy term of the schrödinger equation (2.23) represents the additional energy due to spatial variations of the wavefunction. Finally, by considering the presence of magnetic fields we replace the momentum operator with the canonical momentum operator in a magnetic field 2.24 and add a fifth term accomodating the free energy density of the applied field. m_s and q_s are the mass and charge of the superconducting charge carriers. Note, closer inspection of 2.25 reveals that if $\psi = 0$ we are simply left with the normal state energy density.

$$-\frac{\hbar^2}{2m_s}\nabla^2\psi(\mathbf{r}) \tag{2.23}$$

$$-i\hbar\nabla \rightarrow -i\hbar\nabla - q_s\mathbf{A} \tag{2.24}$$

$$f_s(\mathbf{r},T) = f_n + \alpha(T)\left|\psi\right|^2 + \frac{1}{2}\beta(T)\left|\psi\right|^4 + \frac{1}{2m}\left|(i\hbar\nabla - q_s\mathbf{A})\psi\right|^2 + \frac{1}{2}\mu_0 H^2 \tag{2.25}$$

This Helmholtz free energy density expansion (equation 2.25) is the starting point of GL theory. Remembering that the premise behind GL theory is that the transition into the superconducting state lowers the overall system energy, the next logical step is the minimisation of the volume integral of 2.25 with respect to $\psi(\mathbf{r})$ and $\mathbf{A}(\mathbf{r})$. In the ordinary Landau theory f was simply a function of ψ. Now, since $f = f(\psi, \mathbf{A})$ minimisation must use the Euler-lagrange equations of the calculus of variations. Following such a standard variational procedure we find the two GL differential equations:

$$\alpha\psi + \beta\left|\psi\right|^2\psi + \frac{1}{2m_s}\left(-i\hbar - q_s\mathbf{A}\right)^2\psi = 0, \tag{2.26}$$

$$J_s = -\frac{iq_s\hbar}{2m_s}\left(\psi^*\nabla\psi - \psi\nabla\psi^*\right) - \frac{q_s^2}{m_s}\psi^*\psi\mathbf{A}. \tag{2.27}$$

Here α and β are the GL expansion coefficients, ψ is the macroscopic quantum mechanical wavefunction, m_s and q_s are the mass and charge of the superconducting charge carriers respectively, $\mathbf{A}$ is the magnetic vector potential and J_s is the supercurrent density. Equation 2.26 has the approximate form of the Schrödinger equation and governs the spatial variation of n_s throughout the sample. Equation 2.27 is a quantum mechanical description of the supercurrents.

Reflecting back to the point where GL theory diverged from the general Landau theory (Equation 2.25), the immediate physical consequence of the inclusion of a gradient term $(\nabla\psi)$ becomes apparent. The rapid spatial variation of the macroscopic wavefunction (ψ) in a superconductor is penalised by a large contribution to the free energy. In effect the distance over which ψ can vary is limited by a characteristic lengthscale. This lengthscale is given the symbol $\xi(T)$ and is known as the *coherence length*. We can gain an insight into the nature and origin of ξ through the simplification and reduction of the first GL equation (2.26) for a simple geometry.

Assuming magnetic fields and currents are zero, and only considering the one-dimensional case, 2.26 reduces to,

$$-\frac{\hbar^2}{2m_s}\frac{d^2\psi}{dx^2} + \alpha\psi + \beta\psi^3 = 0. \tag{2.28}$$

Applying appropriate boundary conditions, a solution to 2.28 is given by,

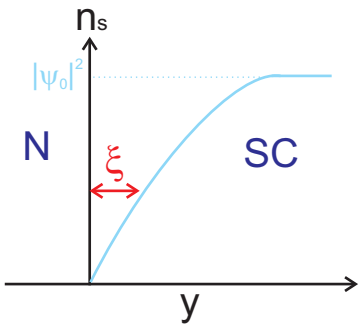

Figure 2-3: The density of superconducting charge carriers within a superconducting material can vary over a characteristic lengthscale (ξ) called the *coherence length*. ξ emerges from the Ginzburg-Landau theory and is defined in equation 2.30.

$$\psi = \psi_0 \tanh\left(\frac{x}{\xi\sqrt{2}}\right), \tag{2.29}$$

where the order parameter deep inside the superconductor is given by $\psi_0 = \sqrt{|\alpha|/\beta}$ and the following substitution has been made,

$$\xi(T) = \sqrt{\frac{\hbar^2}{2m_s\,|\alpha|}} \tag{2.30}$$

Figure 2-3 offers a visual representation of how ψ varies at a superconducting/normal boundary. It is now clear that GL theory achieves what it set out to do: characterise the spatial variation of ψ within a superconductor. As previously mentioned, the Ginzburg-Landau equations are phenomenological in origin but have since been proven to be a rigorous consequence of microscopic theory (c.f. section 2.6) in certain limits of temperature and applied field. As a result of years of subsequent research these limits are now well defined and, as the GL equations are much simpler than the microscopic theory, they are often used whenever possible.

Finally, by substituting the equation for the density of superconducting charge carriers (n_s) as a function of the GL coefficients (2.22) into the equation for the London penetration depth (λ_L) (2.11) we notice that both $\lambda_L(T)$ and $\xi(T)$ share the same temperature dependence of $|\alpha|$.

$$\lambda_L = \sqrt{\frac{m_e \beta}{2\,|\alpha|\,\mu_0 e^2}} \tag{2.31}$$

It is therefore useful to introduce the temperature independent *Ginzburg-Landau* parameter κ. This parameter is particulary useful for characterising the behaviour of superconductors, as we shall see in the next section.

$$\kappa = \frac{\lambda}{\xi} \tag{2.32}$$

2.3 The Superconducting/normal interface

Sections 2.1 and 2.2 introduced two characteristic length scales, $\lambda_L(T)$ and $\xi(T)$, that describe the spatial variation of an applied magnetic field and the density of superconducting charge carriers at a superconducting/normal (SN) boundary respectively. The Ginzburg-Landau parameter κ describes the relative magnitude of the lengthscales and one can immediately envisage the existence of two distinct regimes at the interface, as illustrated schematicaly in figure 2-4.

The physical repercussions of these distinct regimes becomes evident when we consider the energy cost of the interface. We have previously discussed the concept that the nucleation of the superconducting state lowers the overall system energy. By considering the fact that superconductivity is destroyed by a sufficiently large external field, from thermodynamics we defined this critical field (H_c) as being the point at which the energy density of the external field being screened is equal to the condensation energy of superconductivity, as captured by equation (2.4).

It is now clear that the superconducting state can not vanish abruptly at the SN boundary but falls continuously in the vicinity of the interface over a lengthscale given by ξ. The total system condensation energy is therefore increased due to the presence of the normal phase and this correction will result in a *positive* contribution to the interface energy. By a similar argument, we now understand that the applied field isn't completely screened from the sample but rather penetrates a distance λ_L into the superconducting phase. The magnetic energy density of the internal spontaneous magnetisation is therefore lower than we previously considered, and this results in a *negative* contribution to the total

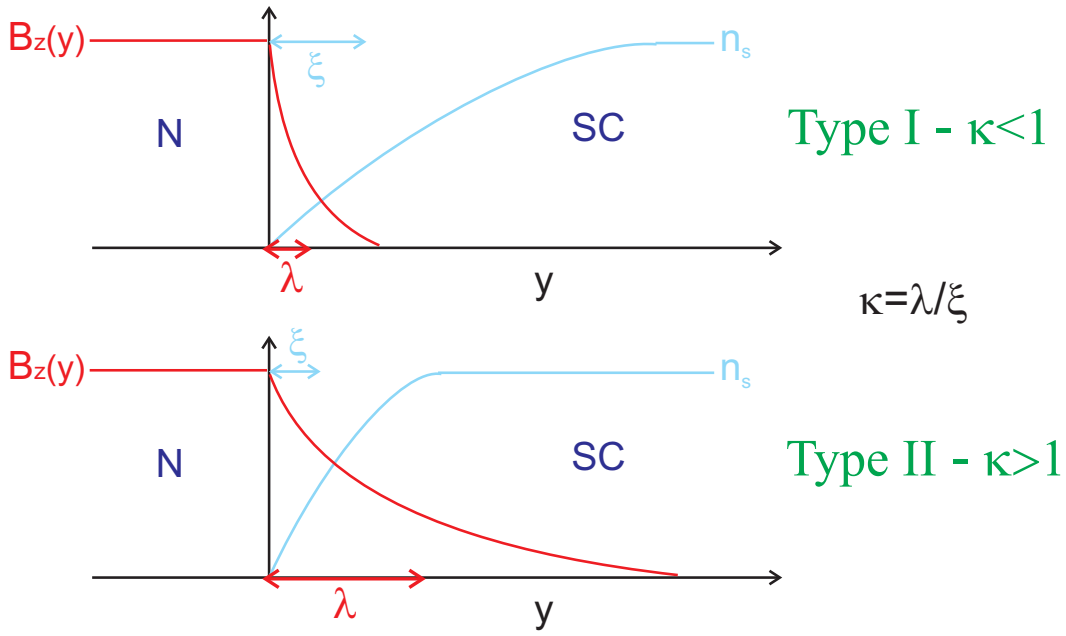

Figure 2-4: A normal (N) superconducting (SC) interface at y=0. The two regimes defined by the Ginzburg-Landau parameter κ represent *positive* (Type I) and *negative* (Type II) boundary energies, resulting in drastically different behaviours in external magnetic fields.

interface energy. Hence the net interface energy per unit area δ is defined as,

$$\delta = \frac{1}{2}\mu_0 H_c^2.(\xi - \lambda_L). \tag{2.33}$$

After inspection of equations 2.33 and 2.32, it becomes apparent that we can define two regimes $\kappa < 1$ and $\kappa > 1$ that correspond to SN boundaries with positive and negative energies respectively. (In fact a more rigorous analysis beyond the scope of this thesis defines the crossover to be at $\kappa = 1/\sqrt{2}$). And we can define two classes of superconductor called Type I and Type II respectively. In the Type I situation, nature abhors SN interfaces and avoids them at all cost, this results in the rather simplistic description of the Meissner effect illustrated in figure 2-1, whereby superconductivity comes to an abrupt and discontinuous end at the thermodynamic critical field H_c.

In Type II superconductors, the situation is rather more complicated. Here the presence of a SN boundary *lowers* the system energy. For applied fields in excess of H_{c1}, nature maximises the SN surface area by admitting flux in the smallest

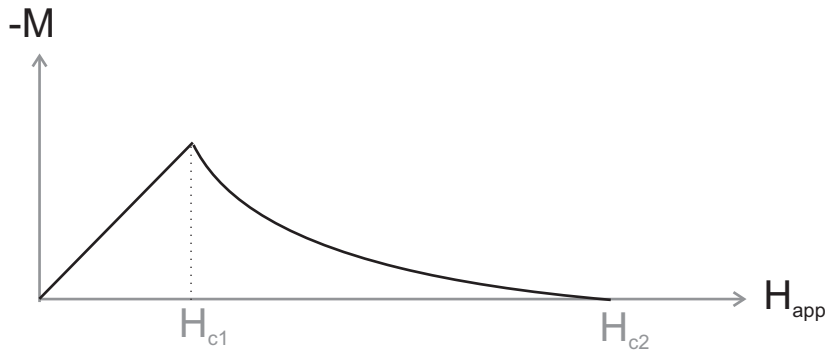

Figure 2-5: The magnetisation curve of a Type II superconductor. In order to lower the overall system energy, Type II superconductors maximise the surface area of the superconducting/normal interface by admitting flux in quantised amounts (vortices) above a lower critical field H_{c1}. The presence of vortices within a sample ($H_{app} > H_{c1}$) is known as the *mixed state*. Vortex entry continues, and superconductivity survives up until the second critical field H_{c2} when adjacent vortex cores overlap and the entire system becomes normal.

possible quantised flux tubes, known as vortices. This allows superconductivity to survive up to much higher critical fields and the presence of superconducting vortices (normal state regions) within a superconducting sample is termed the *mixed state*. The magnetisation curve of a type II superconductor is understandably different to that for Type I materials. The Meissner phase exists up to a lower critical field which we term H_{c1}. For applied field $H_a > H_{c1}$, the sample magnetisation falls gradually as vortices penetrate the sample, and survives up to a second, much higher critical field H_{c2}. c.f. figure 2-5.

2.4 Flux quantisation

The concept of quantisation of flux initially arose as a direct consequence of the postulates of the London theory, long before the emergence of the Ginzburg-Landau (GL) coherence length prompted a rigorous theoretical investigation of SN interface energy. Non-superconducting regions can form in a superconductor for a number of reasons. They can arise from extrinsic effects such as sample impurity and crystalline imperfection, or from the intrinsic physics such as the *Intermediate state* which arise because of strong demagnetisation effects. When considering the case of a normal inclusion in a superconducting material, c.f.

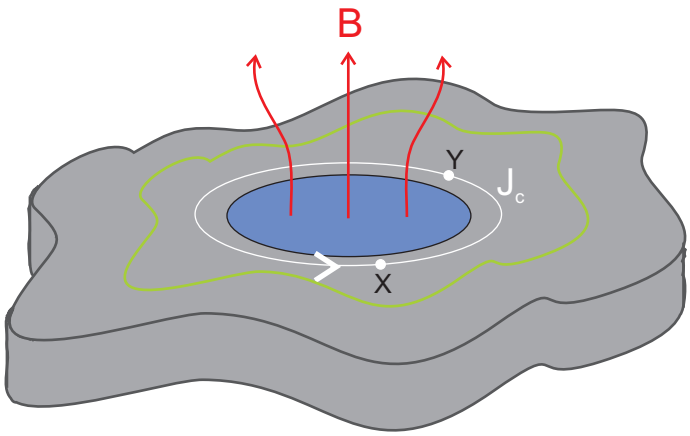

Figure 2-6: A normal inclusion (blue) in a bulk superconductor(grey). The resulting field (red) and supercurrent (white) distributions obey the second London equation. The abitrary path integral C (green) encloses the normal region and a surface area S as referred to in the text.

figure 2-6, the vortical currents, so named because they flow in closed loops around the normal inclusions, are represented in GL formulism by the order parameter in the following way.

$$\psi = |\psi| \, e^{\frac{i(\mathbf{P}\cdot r)}{\hbar}} \tag{2.34}$$

Inserting 2.34 into the second GL equation, assuming H=0 and working through we see that that 2.34 represents a current carrying state with current density,

$$J_s = \frac{q_s P}{m_s} |\psi|^2 \tag{2.35}$$

The closed loop of current flowing around the normal inclusion will have a phase difference ($\Delta\phi$) between points X and Y (fig. 2-6) described by,

$$\Delta\phi_{XY} = \phi_Y - \phi_X = \int_X^Y \frac{P}{\hbar} \cdot d\ell. \tag{2.36}$$

Where ℓ is an infinitesimal section of the current path connecting X and Y. Rearranging 2.35 for P and inserting into 2.36 we arrive at,

$$\Delta\phi_{XY} = \frac{m_s}{\hbar n_s q_s} \int_X^Y J_s \cdot d\ell. \tag{2.37}$$

Where we have recalled that $|\psi|^2 = n_s$.

In the presence of a magnetic field we have to replace $\mathbf{P}$ with the conjugate momentum $\mathbf{P} + q_s\mathbf{A}$ (where $\mathbf{A}$ is the vector potential $\mathbf{B} = \nabla \times \mathbf{A}$). The phase difference now has two components, the first due to the current flow and a second term due to the applied field.

$$\Delta\phi_{XY} = \frac{m_s}{\hbar n_s q_s} \int_X^Y J_s \cdot d\ell + \frac{q_s}{\hbar} \int_X^Y \mathbf{A} \cdot d\ell. \tag{2.38}$$

By definition, the quantum mechanical wave function used to describe the order parameter in GL theory must be single valued. Therefore the total phase difference around the entire current loop must be equal to $n2\pi$, where n is an integer.

$$\Delta\phi_{XY} = \frac{m_s}{\hbar n_s q_s} \oint J_s \cdot d\ell + \frac{q_s}{\hbar} \oint \mathbf{A} \cdot d\ell = n.2\pi \tag{2.39}$$

When considering the integral of a closed loop we can invoke stokes theorem to simplify matters.

$$\oint \mathbf{A}.d\ell = \int\int \nabla \times \mathbf{A}.d\mathbf{S} \tag{2.40}$$

By substituting $\mathbf{B} = \nabla \times \mathbf{A}$ and noticing that the surface integral of $\mathbf{B}.d\mathbf{S}$ is equal to the total flux enclosed within the contour used (Φ) we arrive at the penultimate equation for this section,

$$n.2\pi = \frac{m_s}{\hbar n_s q_s} \oint J_s \cdot d\ell + \frac{q_s}{\hbar}\Phi \tag{2.41}$$

Finally, with a little rearranging and defining $\Phi_0 = h/q_s$ we arrive at the final equation of this section.

$$\Phi = n\Phi_0 - \frac{m_s}{n_s q_s^2} \oint J_s \cdot d\ell \tag{2.42}$$

2.42 is a general statement of fluxoid quantisation. In practice it is possible

to reduce this further by assuming that $J_s = 0$. The vortical supercurrents decay over the lengthscale of the London penetration depth as we move away from the core. If we draw the contour sufficiently far away from the core we can justify the assumption the $J_s = 0$. Hence, we are left with the definition of the superconducting flux quantum, $\phi_0 = h/q_s$, which followed directly from the single valuedness of the superconducting order parameter. Note here that q_s is the charge of the superconducting charge carriers.

$$\Phi = n\Phi_0 \tag{2.43}$$

2.5 Vortex Matter

In section 2.3 we defined two regimes based on considerations of the overall system energy at the superconducting/normal (SN) interface. In the Type II situation, the SN boundary has negative energy and so nature acts to maximise the surface area of the interface by admitting flux (normal regions) into the sample where they coexist alongside Meissner screened areas of residual superconductivity. In light of the results discussed in the previous section (2.4) it is now clear that in order to minimise the total system energy (maximise the SN surface area), flux penetration will occur in the form of flux tubes containing quantised packets of flux (Φ_0) known as superconducting vortices. The microscopic structure of superconducting vortices is illustrated in figure 2-7(a). Conceptually they are no different to the SN boundary encountered previously, except now we have two interfaces (superconducting/normal/superconducting) separated by the smallest distance possible by nature, governed by the characteristic length scales λ_L and ξ. The density of superconducting charge carriers (n_s) falls to zero in the normal core of the vortex over the length ξ, where at the same time $\mathbf{B}$ rises gradually over the length λ_L. The penetration of the $\mathbf{B}$-field creates a resulting vortical supercurrent that flows around the normal core enclosing flux Φ_0. As two vortices are brought into close proximity, the flow of the supercurrent in the $\mathbf{B}$ of the neighbouring normal core realises a short range repulsion from the Lorentz force.

Consideration of the total energy of the SN interface provides an intuitive picture of the definition of the Type I and Type II regimes. However, the concept of Type II superconductivity was first introduced in 1957 when A. A. Abrikosov [7]

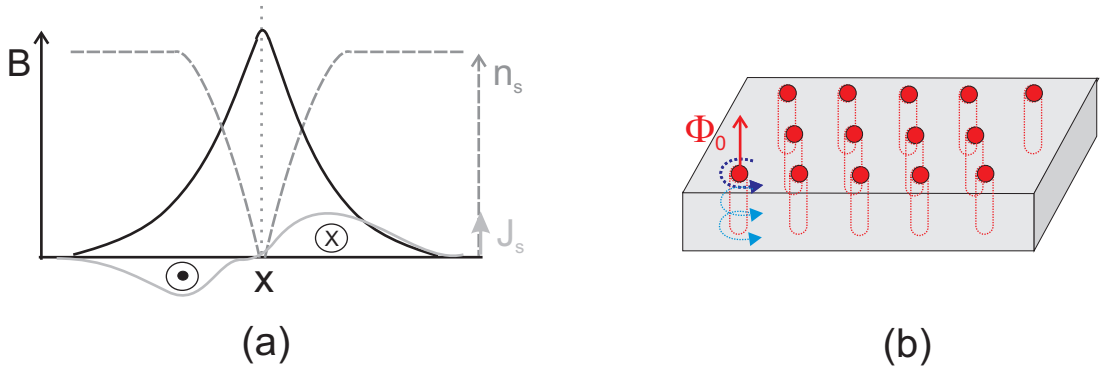

Figure 2-7: (a) The microscopic structure of superconducting vortices in Type II superconductors. The density of superconducting charge carriers n_s falls to zero over the shorter of the two length scales ξ, forming a normal core (diameter$\approx 2\xi$) where the **B**-field rises exponentially over the lengthscale λ_L. Resultant vortical supercurrents (defined by the London equations) circulate the normal core at a diameter of $\approx 2\lambda_L$ enclosing the superconducting flux quantum Φ_0.

published his formal solutions to the Ginzburg-Landau equations in the regime where κ is large ($\lambda > \xi$). His analysis defined the crossover between what he termed Type I and Type II to be exactly at ($\kappa = \lambda/\xi = 1/\sqrt{2}$). Secondly his findings predicted that the most stable configuration was achieved when vortices arranged in a triangular lattice, (2-7(b)), a result that was confirmed experimentally 10 years later by a magnetic decoration technique [8] and has since been observed and studied extensively. Finally, his landmark paper predicted that the vortices would carry a quantised amount of flux equal to,

$$\Phi_0 = \frac{h}{2e}. \tag{2.44}$$

We have seen in the previous section that the quantisation of flux was predicted by the London theory and published 7 years earlier in 1950 [9]. However, crucially the London analysis presented $\Phi_0 = h/q_s$. Where q_s is the charge of particles responsible for superconductivity. The London brothers had no reason to assume that this wasn't anything other than the charge on the electron, but here Abrikosov's result suggested that the charge carrier had a charge of 2e. However, the theoretical understanding of superconductivity was about to take a giant stride forward with the emergence of a radical new theory. Quite coincidentally, research published in 1957, the same year as Abrikosov's landmark paper,

described how the superconducting charge carriers were in fact, quite counter-intuitively, pairs of bound electrons. The theory is known as BCS theory and is described in the following section.

2.6 BCS theory

As early as 1922 Onnes was attempting to investigate the relationship between T_c and nuclear mass using isotopes of mercury. He was unable to detect any effect within the experimental resolution available to him at the time. However, with the advent of modern nuclear physics, the isolation of isotopes with large differences in mass became available and in 1950 a series of experiments on mercury and later tin revealed a power law dependence of T_c on nuclear mass m, $T_c \propto m^{-1/2}$, which became known as the isotope effect [10] [11].

2.6.1 The electron-electron interaction

The isotope effect offered a tantalising insight into superconductivity and suggested that it was inextricably linked to electronic interactions with the ionic lattice, i.e. phonons. It had in fact been predicted theoretically a few years previously by Frölich (1950) [12]. He suggested that an attractive component in the interaction between two electrons emerged as a result of phonon exchange. A simple schematic of such an interaction is shown in figure 2-8. Here the simple relations involving the momenta of two electrons ($\mathbf{k_1}$ and $\mathbf{k_2}$), exchanging a phonon of momentum $\mathbf{q}$,

$$\begin{aligned} \mathbf{k_1} + \mathbf{q} &= \mathbf{k_1'}, \\ \mathbf{k_2} - \mathbf{q} &= \mathbf{k_2'}, \end{aligned} \tag{2.45}$$

combine to demonstrate the conservation of momentum between the initial and final states.

$$\mathbf{k_1} + \mathbf{k_2} = \mathbf{k_1'} + \mathbf{k_2'} \tag{2.46}$$

Frölich argued that momentum need not neccessarily be conserved between

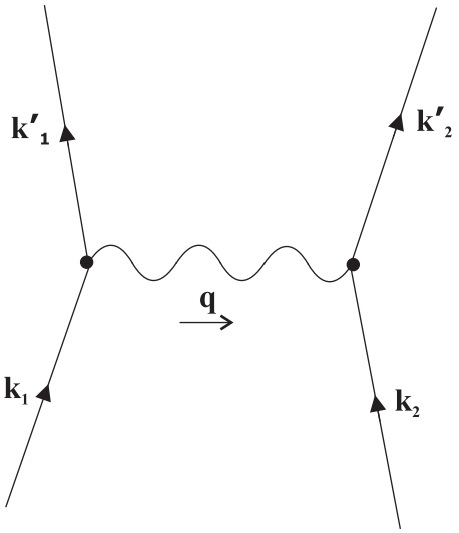

Figure 2-8: Schematic of the electron-electron interaction. The scattering of electrons from states $\mathbf{k_n}$ to $\mathbf{k_n'}$ via exchange of a virtual phonon $\mathbf{q}$ was shown to produce an *attractive* component to their interaction by Frölich [12]. The process was to later form the basis of the BCS theory of superconductivity.

the initial and intermediate states, (when the phonon emmitted by the first electron is yet to be absorbed by the second) or intermediate and final states because of the uncertainty relation $\Delta E.\Delta t \approx \hbar$. If the emission/absorption occurs very quickly, there is a large uncertainty in the energy and it need not be conserved. Such a process is known as *virtual*. The detailed quantum mechanical calculations are beyond the scope of this thesis but Frölich showed that the interaction is *attractive* if the change in energy of the first electron is less than the phonon energy i.e. $\epsilon_1 - \epsilon_1^{'} \leq h\nu_q$, where ϵ_1 and $\epsilon_1^{'}$ are the energies of the first electron before and after emission of a virtual phonon of frequency ν_q. Of course the overall potential landscape is yet to include the coulomb interaction, but the possibility of an attractive component was now apparent.

2.6.2 The Cooper Pair

In 1956, Cooper [13] developed Frölich's work further by considering what happens when two electrons are added to a metal at $T = 0$. He was able to show that they will always form a bound state provided an attractive potential, no matter how weak, is present. The two-particle wavefunction which contains the proba-

bility of finding one electron of momentum $\mathbf{k_1}$ at (x_1, y_1, z_1) and a second electron with $\mathbf{k_2}$ at (x_2, y_2, z_2) is given by the product of two one-particle wavefunctions:

$$\phi\left(x_1, y_1, z_1, \mathbf{k_1}, x_2, y_2, z_2, \mathbf{k_2}\right) = \psi\left(x_1, y_1, z_1, \mathbf{k_1}\right).\psi\left(x_2, y_2, z_2, \mathbf{k_2}\right) \tag{2.47}$$

Quantum mechanically the right-hand-side of equation 2.47 should be a product of spin- and space- wavefunctions. The spin- component is omitted in interests of brevity during this discussion but is treated in section 2.7, and shown to be of great relavance to this thesis. The ψ's are plane waves, and the effect of any scattering mechanism that effects their momenta, such as virtual phonon exchange, will be to "scramble" the wavefunctions such that the total wavefunction becomes a sum of many individual ψ's of varying $\mathbf{k}$'s.

$$\Phi\left(\mathbf{k_1}, \mathbf{k_2}\right) = \sum a_{ij}\phi\left(\mathbf{k_i}, \mathbf{k_j}\right). \tag{2.48}$$

Here the spatial co-ordinates have been left out in interests of brevity. Φ represents a wavefunction of two particles that are scattering repeatedly under the constraint of the conservation of momentum, $\mathbf{k_i} + \mathbf{k_j} = \text{constant} = \mathbf{K}$. $|a_{ij}|^2$ gives the probability of finding the electrons at any instant with momentum $\mathbf{k_i}$ and $\mathbf{k_j}$. If for now we assume this interaction is attractive, then every scattering event (virtual phonon exchange) lowers the system potential by $-V_{ij}$. *Therefore, the total decrease in system energy is proportional to the number of scattering events available (the number of pairs of* $\mathbf{k_i}$ *and* $\mathbf{k_j}$ *that can make up* Φ*)*, a fact that will become very important later. One of the key assumptions of Cooper's work is the simplification that this potential is constant for all scattering events $-V_{ij} = -V$. In fact the detailed QM theory shows that the probability of such a scattering event is neglible unless the difference in energy between the initial (ϵ_1) and final $(\epsilon_1^{'})$ states is small $\epsilon_1 - \epsilon_1^{'} \approx h\nu_q$. Since Cooper assumes the two electrons are added to a metal at $T = 0$ then obeying Pauli they must reside above the fermi level ϵ_f. The lowest values of ϵ_1 and $\epsilon_1^{'}$ that are above ϵ_f but meet the condition $\epsilon_1 - \epsilon_1^{'} \approx h\nu_q$, are those that reside within momentum $\mathbf{\Delta k} = mh\nu_L/\mathbf{k_f}$ of the fermi surface $(\mathbf{k_f})$ [14]. Where ν_L is the average phonon frequency of the ionic lattice. Re-stating the fact that the total momentum is conserved during each scattering event, $\mathbf{k_i} + \mathbf{k_j} = \mathbf{K}$, then all possible scattering events lie in the

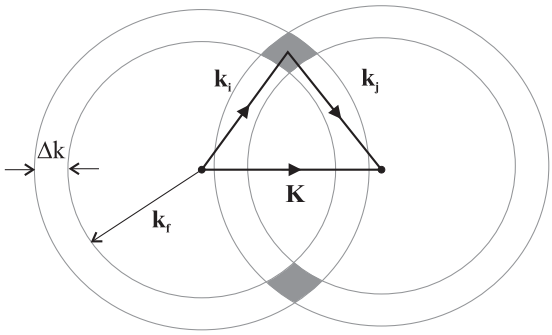

Figure 2-9: Schematic of the electron-electron interaction of two electrons added to a metal at $T = 0$. The available states with an appreciable probability of being occupied lie within a range $\Delta\mathbf{k}$ of the fermi-level $\mathbf{k_f}$. All pairs $(\mathbf{k_i}, \mathbf{k_j})$ that conserve momentum obey the constraint $\mathbf{k_i} + \mathbf{k_j} = \mathbf{K}$ and can be constructed as shown. The number of available pair states is proportional to the size of the shaded areas. For an attractive electron-electron interaction, each scattering event lowers the system energy by $-V$. The maximum number of scattering events is directly proportional to the number of available pair states and so occurs when $K = 0$ (maximising the shaded area). Thus, Cooper realised that the maximum number of scattering events yielding the maximum decrease in system energy occurs when electrons form a pair with equal and opposite momenta; The *Cooper pair* :- $\phi(\mathbf{k_i} \uparrow, \mathbf{k_i} \downarrow)$.

shaded areas of the schematic in figure 2-9. Here the number of scattering events is proportional to the volume of the rings. Since the decrease in total system energy is proportional to the number of scattering events (N, the number of $-V's$), nature would like to maximise N. An examination of figure 2-9 reveals that this maximum occurs when the constant $\mathbf{K} = 0$.

It was therefore the culmination of Cooper's analysis that, when adding two electrons to a metal at $T = 0$, the most energetically favourable state of the system is formed when the electrons form a bound state, just above ϵ_f, with equal and opposite momentum. Further detailed QM calculations revealed that the true minimum was achieved when the electrons had opposite spin too. Forming what became known as the *Cooper pair*, $\phi(\mathbf{k_i} \uparrow, \mathbf{k_i} \downarrow) = \psi(\mathbf{k_i} \uparrow)\psi(\mathbf{k_i} \downarrow)$.

2.6.3 The many-electron BCS ground state

Up until now the presence of a resultant attractive interaction has been assumed, but the decisive extension was made the following year when, as a culmination of

all of the rapid theoretical and experimental developments in the field, Bardeen, Cooper and Schriefer published their epoch-making BCS theory,[15] which tied all of the evidence together. BCS shows how an electron can deform the ionic lattice, increasing the local positive charge density and forming an attractive potential to a second electron, present later in time, sufficient enough to overcome the repulsive coulomb potential. This interaction with the lattice explains the isotope effect; clearly, altering the ionic mass will change the natural frequency of the lattice vibrations and impact on the interaction. It also helps to explain why some of the best normal state conductors (copper, gold etc) don't superconduct. Electrical resistance results from electron scattering caused by lattice phonons. Materials with a low normal state resistance therefore have a weak electron-phonon interaction, characterised by a small coupling constant. Superconductivity naturally requires a high electron-phonon coupling constant which manifests itself as higher electrical resistance in the normal state.

The theory of *Cooper pairing* somewhat unrealistically treated two electrons in isolation. BCS remedied this by treating all of the electrons on the same footing. A fundamental assumption of BCS is that in the superconducting state, the only interactions that matter are those involved in the individual Cooper pairs themselves. The only effect of the presence of multiple Cooper pairs is to reduce the number of available $(\mathbf{k}\uparrow, \mathbf{k}\downarrow)$ pairing states left. In fact, the pairing need not only concern electrons above the fermi level but we can take two electrons of $\epsilon < \epsilon_f$ and promote them above ϵ_f and form an energetically favourable state. The probability that state $\phi(\mathbf{k_i}\uparrow, \mathbf{k_i}\downarrow)$ is full at $T = 0$, is displayed alongside the conventional fermi-dirac distribution for an electron in a metal in figure 2-10. The key feature is that Cooper pair states above ϵ_f are occupied even at $T = 0$. BCS theory recognised that if we can promote one pair, then we can promote many pairs and lower the system energy even further and introduced the many-electron wavefuntion (Ψ) which is a product of many pair wavefunctions, where $\mathbf{r}$ is the positional vector (x, y, z) and $n/2$ is the total number of Cooper pairs.

$$\Psi\left(\mathbf{r_1}, \mathbf{r_2}..., r_n\right) = \Phi(\mathbf{r_1}, \mathbf{r_2})\Phi(\mathbf{r_3}, \mathbf{r_4})...\Phi(\mathbf{r_{n-1}}, \mathbf{r_n}). \tag{2.49}$$

The many-electron wavefunction simply gives the probability of finding an electron at $\mathbf{r_1}$ at the same time as another at $\mathbf{r_2}$, regardless of their momenta. By populating 2.49 with many Cooper pairs we can significantly lower the energy

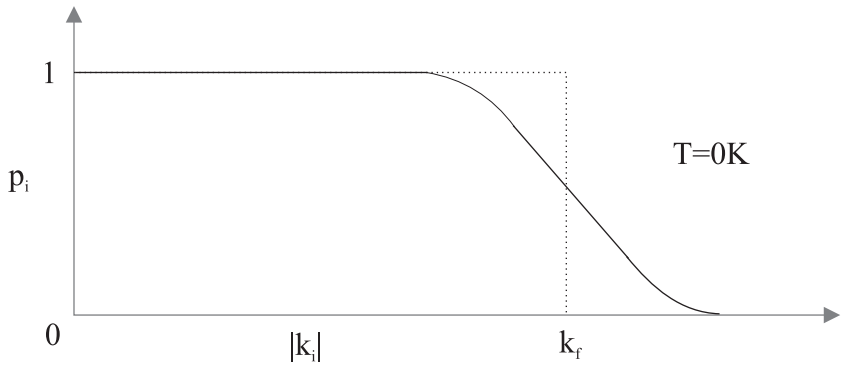

Figure 2-10: The probability p_i that the Cooper pair state $\phi(\mathbf{k_i} \uparrow, \mathbf{k_i} \downarrow)$ is occupied at $T = 0$. The conventional fermi-dirac distribution for electrons in a metal is also plotted (dotted line) for comparison. Note that even at $T = 0$, it is energetically favourable to promote some electrons above the fermi-energy k_f where they reduce the overall system energy by forming *Cooper pairs*.

of the system and we note, crucially, that the Cooper pairs have all formed the same quantum mechanical state, with the same energy, seemingly violating the Pauli exclusion principle. It is for this reason that Cooper pairs can be viewed as composite particles, bosons with mass $2m_e$ and charge 2e, that obey Bose-Einstein statistics. Superconductivity is thus referred to as a special case of *Bose-Einstein condensation*. Since all of the Cooper pairs share the same quantum state, they all have the same phase and as we have seen are represented by one wavefunction which is coherent over the entire superconducting sample, which in the case of a coil, could be many Km. Superconductivity is therefore described as macroscopic quantum mechanical effect and this long range coherence gives rise to many of the observed phenomena.

A key prediction to come out of BCS theory is that a minimum energy is required to break a Cooper pair. This *binding energy* immediately explained the energy gaps that had previously been observed experimentally by measurements of the electronic specific heat [16] [17] and later electromagnetic absorption [18, 19, 20], and one of the early successes of BCS was to predict these accurately. The energy gap also provided an explanation for zero resistivity; The Cooper pairs can not scatter off lattice phonons i.e. dissipate energy resulting in an observable electrical resistance, if the lattice phonons are below a threshold energy. As a superconducting material is cooled below T_c the lattice vibrations fall below this threshold and perfect conductivity ensues.

2.7 Unconventional Superconductivity

Throughout the discussion of the previous section (2.6) we have so far only considered an electron-pair wavefunction that contains information on the spatial extent of the pair. As briefly mentioned, a more thorough description requires a consideration of the spin-wavefunction so that the total wavefunction (Ψ) is a combination of spatial ψ and spin χ components. As we know, a complete description allows for current carrying states and includes a third component, described by GL theory 2.2, that concerns the centre-of-mass motion of the Cooper pair.

It is important to note here, that we have abandoned the formulism of the previous section so that now the many-electron wavefunction that describes the spatial extent of every Cooper pair in the superconductor is ψ (previously Ψ) and now Ψ represents the full pair wavefunction, a combination of spatial and spin components.

$$\Psi = \psi(\mathbf{r_1}, \mathbf{r_2}..., \mathbf{r_n}, \mathbf{k_1}, \mathbf{k_2}..., \mathbf{k_n}).\chi(\mathbf{s_1}, \mathbf{s_2}..., \mathbf{s_n}) \tag{2.50}$$

As in equation 2.49, $n/2$ is the number of Cooper pairs in the system. However, here the spatial component ψ is a function of position in space r_n and momentum (k_n) of each electron. Previously, in 2.49, we omitted the momentum parameters for brevity, but here we include them to allow for states other than the Cooper pair of equal and opposite momenta. Finally the spin-component is a function of the spin state (up or down) of each electron.

A key feature of BCS theory is that the Cooper pair has a quantum mechanical *symmetry*. Just as the spatial distributions of electrons bound to a hydrogen atom display symmetries, as defined by the spherical harmonic solutions to the schrödinger equation, so do the BCS wavefunctions. In a broad sense superconductivity is a sort of Bose-Einstein condensation and the Cooper pair (CP) can be thought of as a boson. A CP can therefore have integer total spin S=0 or 1. The particular BCS ground state ψ that was introduced in the previous section 2.6.3 has zero net angular momentum, c.f. figure 2-10 and so continuing the analogy with atomic orbitals is termed *s-wave* ($\ell = 0$). Heisenberg [21] was the first to note in 1926 that as a fermion (1/2 integral spin) the total wavefunction describing electronic states must be anti-symmetric. The ($\ell = 0$) s-orbital is spatially symmetric so the spin part of the full wavefunction is anti-symmetric. i.e.

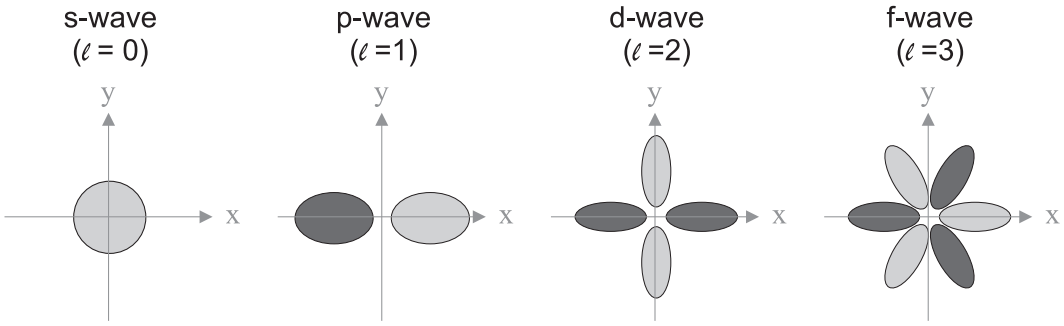

Figure 2-11: Two-dinemsional illustrative representations of Cooper pair spatial symmetries for angular momentum $\ell = 0..3$. The different shading reflects regions where the wavefunction has opposite sign.

Anti-parallel spins S=0, *spin-singlet* case. This pairing state is found in what are now termed *conventional* superconductors.

Now we relax the ($\ell = 0$) condition and consider that pairings can exist with $\ell = 0, 2$ (even) or $\ell = 1, 3$ (odd) angular momentum, forming states which will require spin-singlet (S= 0) or spin-triplet (S= 1) spin components respectively. 2D representations of the real space distributions of $\ell = 0..3$ bound states are illustrated in figure 2-11. Significantly, electrons in an s-wave pairing state have an isotropic probability distribution of very closely spaced, strongly overlapping electron states, whereas the spatial symmetries of non-zero angular momentum states have vanishing probabilities at their centre of mass (origin).

The Coulomb interaction is clearly a strong function of the spatial and spin symmetry of the CP. The strong repulsion of closely bound electrons in a conventional s-wave CP is overcome by the electron-phonon interaction as described by BCS theory.

The Coulomb repulsion in $\ell > 0$ bound states is minimised as the probability density falls to zero at short distances, and so electronic interactions clearly play an important role. In contrast to BCS theory of s-wave superconductivity no many-body theory exists to describe how ($\ell > 0$) CP bound states are stabilised by electron-electron interactions in crystalline materials. Superconducivity involving such $\ell > 0$ pairing is termed *unconventional*.

S-wave pairing is termed conventional for several reasons. Historically it was discovered first and indeed for the first 60 years of superconductivity all known superconductors were s-wave. Secondly, it is in some ways the simplest pairing

state. In $\ell > 0$ states the wavefuntion changes sign as illustrated by the shaded areas in figure 2-11. The spatial symmetry of the CP in real space is related to the superconducting gap function (c.f. section 2.6.3) $\Delta(\mathbf{k})$ in k-space by a Fourier transform. In reality, the magnitude of $\Delta(\mathbf{k})$ in s-wave pairing may vary slightly due to anisotropies of the crystal lattice but the *phase* is constant. For $\ell > 0$ there are sign changes in the phase which average to zero over the fermi surface. This leads to a more precise definition of *unconventional* superconductivity as,

$$\int \Delta(\mathbf{k}) d^3\mathbf{k} = 0 \tag{2.51}$$

Chapter 3

Experimental Techniques

Numerous techniques for detecting stray magnetic fields at the surface of superconducting samples have been developed in recent years. Most notably: Superconducting Quantum Interference Devices (SQUIDS), Magnetic Force Microscopy (MFM), Lorentz Force Microscopy (LFM), Bitter decoration, Magneto-Optical Imaging (MOI) and Scanning Hall Probe Microscopy (SHPM). Together they cover a wide range of spatial resolutions and minimum detectable fields. Each method has it's own advantages and limitations with respect to the others. A more thorough evaluation of each technique is presented in [22]. Here we focus on the methods used to acquire the data discussed in this thesis: SHPM and MOI.

3.1 Scanning Hall Probe Microscopy

3.1.1 The Hall effect

The Hall effect is a macroscopic manifestation of the Lorentz force; the well known phenomenom whereby the motion of a charged particle in a magnetic field results in a force (F_L) on a charge (q) described by:

$$\mathbf{F_L} = q\left(\mathbf{B} \times \nu_q\right), \tag{3.1}$$

where ν_q is the velocity of charge q moving through a region with a magnetic field B. An electric current confined by the free surfaces of a conductor will drift to one side under the Lorentz force, thereby setting up a voltage across the

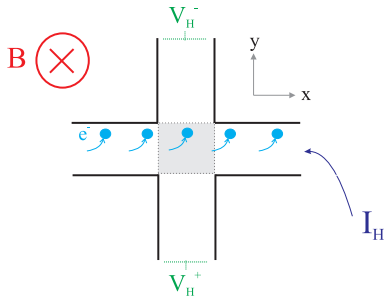

Figure 3-1: The Hall cross geometry provides a convenient way of measuring the Hall effect in a conductor. The motion of the electrons forming the Hall current (I_H) in the magnetic field B results in a Lorentz force (F_L), causing the charge carriers to drift to one side of the conductor. The resulting Hall voltage (V_H) across the Hall probe active area (shaded) can be measured across the second pair of leads.

conductor known as the Hall voltage (V_H).

In turn, the electric field associated with V_H itself exerts a force on the electrons and the system reaches equilibrium when these two forces, Lorentz and electric, balance.

$$\mathbf{E}q = q\left(\mathbf{B} \times \nu_q\right). \tag{3.2}$$

Substituting for the current density $J = -ne\nu_q$ and considering the specific geometry illustrated in figure 3-1 gives,

$$E_y = -\frac{J_x}{ne} B_z. \tag{3.3}$$

Making further assumptions that the applied Hall current I_H (contained in J_x) and physical size of the conductor are kept constant, we notice that V_H (contained in E_y) is directly proportional to the local magnetic induction B. V_H is an experimentally accessible quantity and so the Hall probe's suitability as a field sensing device becomes apparent. A particularly convenient Hall sensor geometry is the cross we have been considering in figure 3-1. A constant Hall current (I_H) is supplied along two opposing leads and experimental access to V_H across the *active* area (shaded) is afforded by the second pair of leads. In such a geometry, the spatial resolution of the Hall probe (HP) device is limited by the size of the cross-sectional active area. Another figure of merit for a HP, and one

which defines the minimum detectable field, is the Hall coeffiecient (R_H), found by re-arranging equation 3.4.

$$\frac{E_y}{J_x B_z} = -\frac{1}{n_{2D} e} = R_H. \tag{3.4}$$

Keeping J_x constant, 3.3 describes how a bigger R_H results in a larger V_H for a given measured magnetic field. In the presence of a constant mean noise level, a larger R_H allows detection of smaller fields and increases the sensitivity of the HP device. As such, recent research into Hall probe magnetometry has been heavily focussed on materials with extremely low carrier concentrations (n). Semi-metals such as Bismuth [23] and semiconductors such as Si-doped GaAs [24] are two such low-n candidates, but unfortunately as the active area is reduced to the order of $1\mu m^2$ (a must for the spatial resolution required to study vortex matter in superconductors) the resistance of these materials increases dramatically. Any gains in sensitivity offered by the small n can be offset by the related increase in Johnson noise and a lower SNR.

3.1.2 Semiconductor heterojunction Hall probes

In the particular case of Si-doped GaAs, the high resistance results from ionized impurity scattering between the electrons and their donor ions. An elegant solution to this problem was found in the development of modulation doped heterostructures, where the charge carriers are physically and permanently separated from their donor ions in a very low density two-dimensional electron gas (2DEG). These heterojunctions were first reported by Dingle *et al* in 1978 [25] and subsequently revolutionized the field. A schematic of the heterostructure and resulting conduction band (CB) edge energy is shown in figure 3-2. The conduction bands of GaAs and $Al_{0.3}Ga_{0.7}As$ lie at different energies but since the lattice constants are nearly identical the whole structure can be viewed as a single crystal with a modulated CB edge. The much larger band gap of $Al_{0.3}Ga_{0.7}As$ creates a V-shaped potential well at the interface of the $Al_{0.3}Ga_{0.7}As$ and GaAs lattices. In order to reach diffusive equilibrium the Fermi-level must be independent of position and as the electrons are thermally liberated from their Si donors they migrate to the lower energy CB of GaAs. The electrons are restricted to a narrow layer in the z direction but are free to move in $x - y$ and so this is

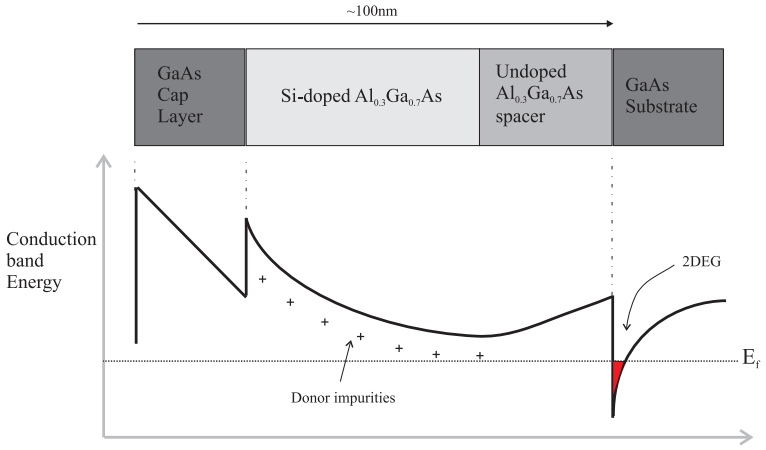

Figure 3-2: A schematic of the heterostructure and corresponding conduction band (CB) edge energy of a modulation-doped semiconductor heterostructure. The mismatched CB energies of $Al_{0.3}Ga_{0.7}As$ (higher) and GaAs (lower) creates a narrow triangular potential well at the lattice matched crystal interface. Electrons migrate from the Si-doped region into the potential well and crucially, remain irreversibly separated from their ionized donor impurities by the spacer layer. This realises extremely high mobilities of $\mu > 100m^2V^{-1}s^{-1}$ (4.2K). The electrons are trapped in a narrow region but are otherwise free to move in the horizontal plane of the superlattice. As such these charge carriers are termed a *two dimensional electron gas* (2DEG).

known as a 2DEG, and forms with typical densities of $n_{2D} = 10^{15}m^{-2}$. The key to the high mobility of these devices ($\mu > 100m^2V^{-1}s^{-1}$ at 4.2K) is the undoped spacer layer which separates the electrons from their ionised donors, drastically reducing ionised impurity scattering.

The low carrier density (large $R_H \approx 0.3\Omega/G$) and high mobility (low Johnson noise) make semiconductor modulation-doped heterojunctions ideal for high field sensitivity Hall probe devices. Wafers of $GaAs/Al_{0.3}Ga_{0.7}As$ are available commercially and are routinely patterned into sub-micron Hall cross geometries which realise minimum detectable fields of $10mG/Hz^{\frac{1}{2}}$. Fabrication involves a combination of conventional lithography (optical and/or electron-beam) and wet chemical etching. Ohmic contacts are made to the heterostructure through Au/Ge/Ti/Au pads. The whole process is described in more detail in [26]. An optical micrograph of one of the Hall probes used to collect data for this thesis is shown in figure 3-3. The sub-micron active area was originally defined as $1\mu m^2$ using electron-beam lithography, but it is estimated that edge depletion effects [22] occuring during

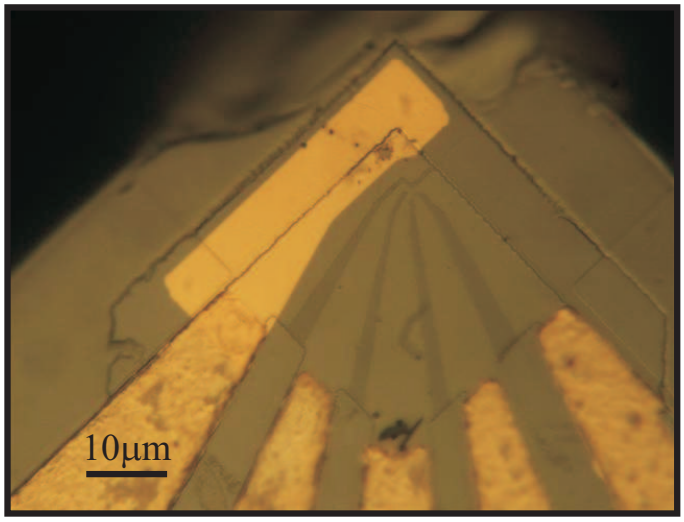

Figure 3-3: A photograph of an $Al_{0.3}Ga_{0.7}As/GaAs$ heterostructure Hall probe. Fabrication involves numerous steps of optical lithography, thermal deposition (Au,Ge and Ti) and wet chemical etching. Five gold contact leads are visible around the $1\mu m^2$ active area. Four comprise the Hall cross leads while the fifth connects an integrated tunnelling tip, used to detect the sample surface.

the chemical wet etching phase reduce this to $\approx 800 \times 800 nm^2$. The active area is surrounded by five fluted leads; four comprise the Hall cross leads and the fifth is connected to an integrated scanning tunneling tip (Ti/Au) which allows tracking of the sample surface through detection of a tunnel current.

The field sensitivity can be increased by passing larger Hall currents (I_H) through the device, as shown by equation 3.3. In practice however the low-frequency V_H becomes dominated by random telegraph-like noise at critical dc bias currents in excess of I_{max} which is presumably related to the thermionic trapping and emission of excited electrons from deep donor sites in the $Al_{0.3}Ga_{0.7}As$ layer. For $I_H < I_{max}$ and at T<100K the sensitivity is approximately limited by the Johnson noise of the voltage contacts ($V_J = (4k_BTR_V\Delta f)^{1/2}$) where R_V is the two contact resistance of the Hall cross and Δf is the measurement bandwidth. For leads of width w and length l the signal-to-noise ratio (SNR) is therefore defined as:

$$SNR = \frac{I_H R_H B}{(4k_BTR_v\Delta f)^{1/2}} \approx (\frac{\mu}{n_{2D}})^{1/2}(\frac{w}{4k_BTel\Delta f})^{1/2} I_H B \qquad (3.5)$$

Keeping all other factors constant we see that SNR$\propto (\mu/n_{2D})^{1/2}$ which be-

comes a useful figure of merit for a HP device in addition to R_H. Consequently, typical values of I_H $\approx$10μA and lead resistance R_V $\approx$1.5KΩ (4.2K) realise minimum detectable fields of $\sim$10mG/Hz$^{1/2}$ and HP active areas of 800$\times$800 nm^2 realise minimum flux resolution of $\sim 1 \times 10^{-5}\Phi_0/\text{Hz}^{1/2}$.

In practice, V_H has a strongly temperature dependent offset, notionally due to slight asymmetry of the Hall cross geometry but in reality arising from microscopic inhomogeneities in the 2DEG heterostructure. This potential difference across the HP shares the same T-dependence as the charge mobility (μ) and so subtraction of this signal is required after changes in temperature. For this reason HPs are unable to measure *absolute* B and strictly speaking record the local *relative* magnetic induction.

The spatial resolution is governed by the width of the Hall cross (w) or sample/sensor separation, whichever is the greater. The SNR falls with square root of w (equation 3.5) and given that 2DEG charge carrier densities of $n_{2D} \sim 10^{15}\text{m}^{-2}$ correspond to the presence of $\sim$10 electrons in a w =100nm HP, it is obvious that reducing w to around this size will lead to large noise levels due to statistical fluctuations in the instantaneous number of electrons in the active area. Furthermore, sample/sensor separations of order $\sim$500nm are required to ensure the safety of the HP while rastering over the sample surface. Therefore there is little to gain in patterning HP with w <500nm and the devices used in the collection of data for this thesis are typically w $\approx$800nm.

As the spatial resolution is of the order of the characteristic length scales of superconductivity, significant signal broadening occurs which has to be accounted for when making comparisons with theory. This procedure is discussed during the analysis of the results presented in chapter 4.

3.1.3 Microscope design

The low temperature Scanning Hall Probe Microscope used to acquire the data discussed in this thesis is the latest in a line of SHPM's to be developed at the University of Bath. Detailed information on the design, construction and operation of this instrument is contained in [27]. A brief summary of the main features is provided here.

Cryostat

Figure 3-4 contains a schematic and photograph of elements of the microscope design. A commercial ^{3}He refrigerator is mounted into a variable temperature insert (VTI) which forms part of a superconducting magnet system within an Oxford instruments ^{4}H cryostat (3-4). The VTI is inserted directly into a liquid Helium bath (4.2K - grey area) which itself sits in a bath of liquid Nitrogen (77K - not shown). A needle valve bleeds small amounts of ^{4}He into the VTI space (cyan), which, in unison with a rotary vacuum pump, allows controlled cooling of the VTI to a base temperature of $\approx 2K$. Extensive information on the workings of a ^{3}He refrigerator are available in the literature but a brief description is as follows. ^{3}He is liberated from it's charcoal reservoir by heating of the 'sorption pump. As the ^{3}He vapour pressure rises it flows down the VTI and condenses on the 1K plate and collects in the ^{3}He pot which is in good thermal contact with the sample. When all of the ^{3}He is liberated (typically 20 mins at 20 K) the ^{3}He pot is full and will typically have been cooled to $\sim$1.5K. The 'sorption pump heater is then ready to be turned off and once it cools to below $\sim$10K it reverses it's action; ^{3}He evaporates from the ^{3}He pot and is pumped back up to the reservoir where it is readily adsorbed by highly porous charcoal. The cooling power of this evaporation can in principle maintain a base temperature of 250mK for >24 hours but in practice, the heating power from the various electronics and the multiple cable connections to room temperature reduce this to 350mK for $\sim$10 hours.

Microscope head

The custom made microscope head is sketched in figure 3-4. It bolts directly onto the cold flange of the ^{3}He pot. The sample is stuck onto the sample holder (pictured) with silver paste, which not only secures the sample but, by carefully dragging the paste onto the sample surface, also assures the good electrical contact essential for application of a small sample voltage bias which aids detection of the sample surface via a tunnel current. The pin (pictured) connects the sample bias signal, and the copper braid is screwed directly onto the ^{3}He pot to assure good thermal contact. The Hall probe sits opposite the sample and is mounted on top of a large piezoelectric scanner tube. The tube consists of four

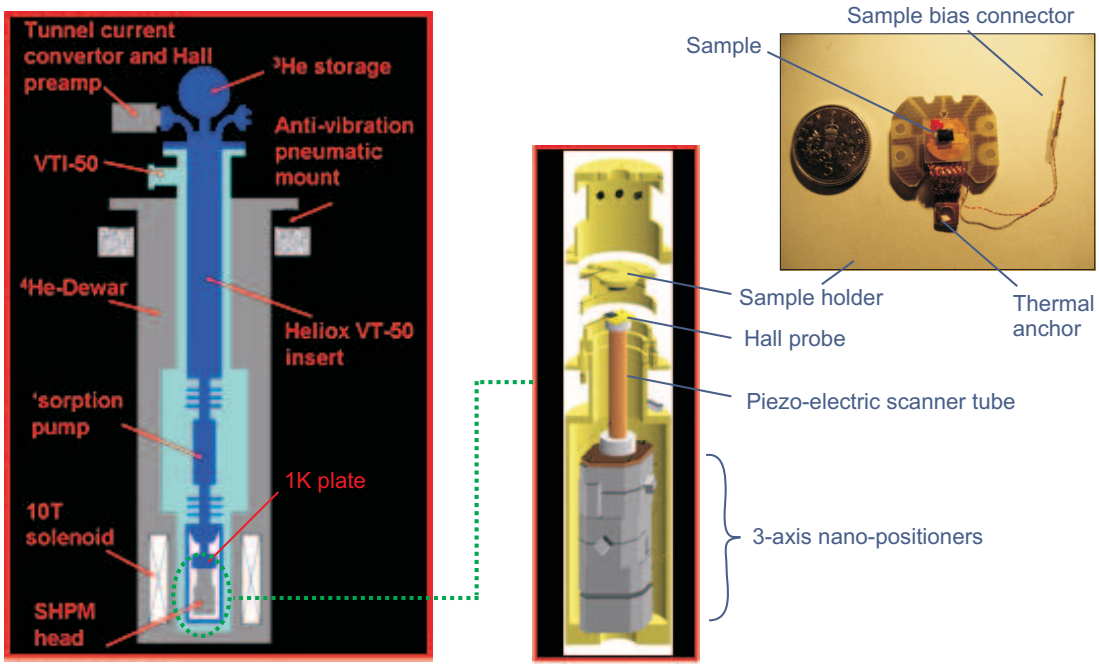

Figure 3-4: A schematic of the 300mK Scanning Hall Probe Microscope system used for the collection of data presented in this thesis. The custom-made SHPM head is attached directly onto the cold flange of a commercial ^{3}He refrigerator which itself is incorporated into a commercial variable temperature insert that sits in a liquid Helium cryostat.

electrode quadrants of piezoelectric material, a substance that contracts/expands with applied positive/negative voltage. The quad-electrode design facilitates HP movement in the $x-y$ plane through selectively applied voltages. Application of a common voltage to all four electrodes equally, results in extension/retraction in the z direction. The piezo-electric coefficient varies with temperature and this system achieves scanner ranges of 170 x 170 x 4.7 μm^3 at 300K down to 14 x 14 x 0.6μm^3 at 350mK. The scanner tube sits on three nano-positioners which afford coarse positioning in a 6x6x7 mm^3 volume.

Finally, great care has to be taken to set the tilt angle between the sample and Hall probe to ensure that the tunnelling tip is always closest to the sample. This is done manually on a work top bench using a microscope and the reflection of the Hall probe in the sample surface. Adjustment is made via 3 fine threaded screws to achieve an angle of $\approx 1^o$. The HP active area is approximately $5\mu m$ from the tunneling tip so an angle greater than this will increase the sample sensor separation and reduce the spatial resolution unneccesarily, or even worse, cause the un-coated edge of the GaAs wafer to contact the sample before the Au tunnel tip. Any less than this and we risk destroying the HP by crashing it into the surface on approach.

Control electronics

The whole system is controlled using a Nanomagnetics Instruments Ltd system. A schematic of the control electronics is displayed in figure 3-5. Automatic approach and sample surface detection is achieved by repeated cycles of: scanner tube extension, scanner tube retraction, followed by one nano-postioner coarse approach step. (The full scanner tube extension is much greater than one coarse forward step.) The sample is biased at 200mV and the tunnel current (I_t) is continuously monitored throughout. The cycle is interupted when I_t exceeds a pre-determined threshold and a feedback loop monitors I_t continuosly and adjusts the scanner voltages accordingly. Image acquisition can take place in tunnel contact ("STM tracking mode") if the scan speed is kept low $< 1\mu m s^{-1}$ but data collection is slow in this mode and there is a higher risk of a "head crash" caused by external vibrations. Since little spatial resolution is gained by reducing the sample/sensor separation to less than the width of the HP active area, there is scant reward for approaching less than $\sim 500nm$. For these reasons normal op-

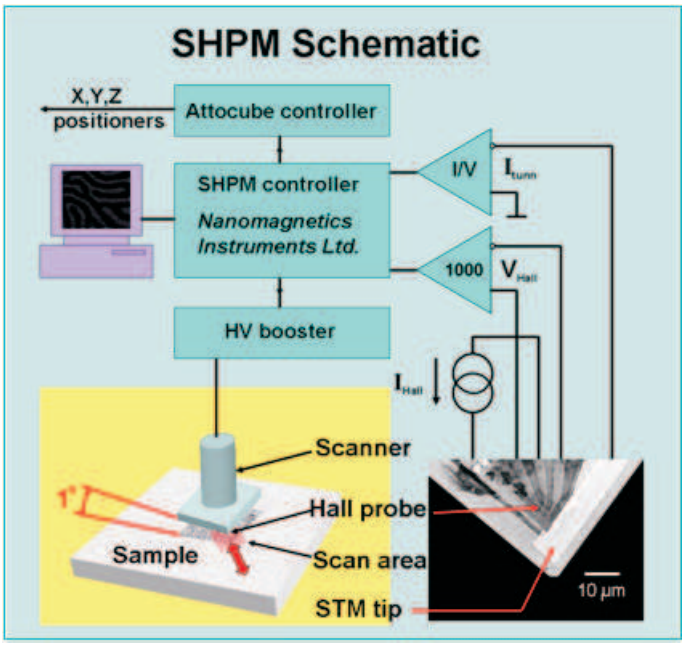

Figure 3-5: A schematic of the SHPM system including control electronics. The tunnel current between the biased sample and the integrated STM tip is sensed and controlled during coarse nano-positioner approach in order to bring the Hall probe into close proximity with the surface safely. The controller also generates the scanner voltages which are post-amplified and raster the Hall probe over the sample surface.

eration is in "flying mode" when the HP is retracted either by a single positioner step, or, for very fine adjustment, by a small "lift-off" voltage applied to the piezeotube, and is rastered across the sample at $14\mu ms^{-1}$

Performance

Table 3.1 summarises the key facts and figures for the mk-SHPM system at University of Bath Physics department.

3.2 Magneto-Optical Imaging

3.2.1 The Faraday effect

The suitability of magneto-optical imaging (MOI) as a technique for the detection of stray fields at the surface of a superconductor lies in the fundamental

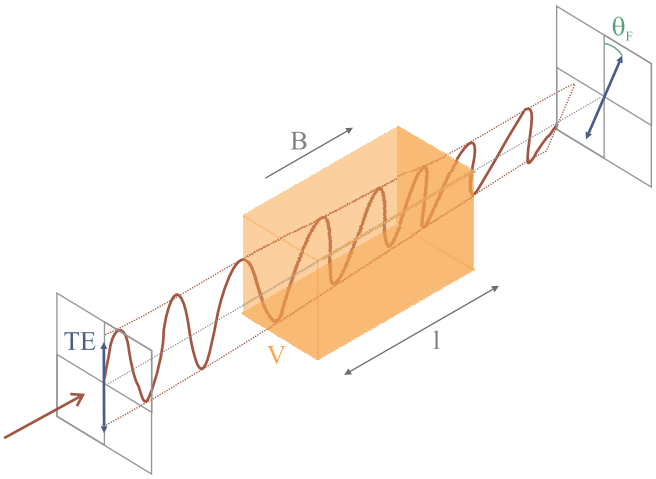

Figure 3-6: The Faraday effect. The transverse electric (TE) mode of plane polarised light rotates through angle θ_F as it propogates through a magnetically active medium of length l in the presence of parallel magnetic induction $\mathbf{B}$

physics behind the *Faraday effect*. First observed by Michael Faraday in 1845 [28], the phenomenon involves the rotation of the plane of linearly polarised light as it propagates through a medium with magnetisation parallel to the propagation vector. More specifically, the refractive indices of left and right circularly polarised light differ in the presence of a magnetic field applied in the direction of propagation ($\Delta n(\mathbf{B})$). Since plane polarised light is a superposition of left and right circularly polarised light, a phase shift introduced by $\Delta n(\mathbf{B})$ grows with the length of medium (l) the light has travelled through, with a resultant rotation of the plane of polarisation. This phenomenon is defined in equation 3.6 and illustrated schematically in figure 3-6.

Field resolution	10 $mG/Hz^{\frac{1}{2}}$
Spatial resolution	≈800*nm
2DEG μ (350mK)	100 $m^2V^{-1}s^{-1}$
n_{2D} (350mk)	3×10^{15} m^{-2}
Base temperature	≈300mK
Scan size (350mK)	14 × 14 μm^2

Table 3.1: A selection of key figures for the mK-SHPM system at the University of Bath. *Based on $1\mu m^2$ active area Hall probe fabricated with electron beam lithography used in the experiments described in this thesis.

$$\theta_F = VBl \tag{3.6}$$

Where the *Faraday rotation* (θ_F) is proportional to the length of the magnetised medium (l) in presence of magnetic induction **B**. The material dependent *Verdet constant* (V) is the figure of merit for a magneto-optically active material.

3.2.2 Magneto-optic layer

Since no superconductors have been found to be magnetically and optically active, the provision of a suitable medium, known as the magneto-optic layer (MOL), in intimate contact with the sample is required as a medium for a *Farady rotation* to occur if MOI is to be a useful tool for detecting flux structures in superconductors. A slightly different set-up to that shown in figure 3-6 is therefore necessary and is described in full in the following section. The effectiveness of MOI (field and spatial resolution) hinges on the choice of material (with its unique Verdet constant) for the Magneto-optic layer and so this area has been the focus of intense research and development in the last five decades. Alers (1957) [29] and De Sorbo (1960) [30] were the first to investigate the stray fields at the surface of superconductors in the intermediate state using $Ce(PO_3)_3$ and $Ce(NO_3)_3$ as MOL's and achieved moderate spatial resolutions of $\approx 200\mu m$. The field took a leap forward into the "high resolution" age when Kirchner (1969) [31] employed paramagnetic Europium Chalcogenides and Halogenides with Verdet constants two orders of magnitude greater than previously attained.

In 1989 Polyanskii [32] took a different approach and developed the technique with ferrimagnetic Bi- or Ge-doped Fe garnet films. These had the added advantage that they could be grown epitaxially and so were of high crystalline purity, but unfortunately the easy-axis of the internal magnetisation lay perpendicular to the plane of film (parallel to applied field) and so hampered measurements of absolute field strength. Stray fields were often inferred indirectly via observation of shifts in the domain patterns. Furthermore the labyrinthine domain structure limited spatial resolution to the order of the domain size ($\approx$2-30μm)[33] but nevertheless, large Faraday rotations of $\approx 4^o \mu m^{-1}$ were achievable [33]. The field progressed towards its current state-of-the-art in the mid-nineties when Wallenhorst [34] and Grechishkin [35] improved on the garnet films of Polyanskii by

tilting the easy axis of magnetisation into the plane of the film through critical doping with Bismuth. The Bi-doped Yttrium Iron garnet (Bi-YIG) films grown using liquid phase epitaxy have extremely high crystalline quality and, since they avoid the magnetic domain problems encountered previously, they enable field sensitivity of $\approx 10\mu T$ corresponding to *Faraday rotations* of order $\approx 7-9^o\mu m^{-1}$. The spatial resolution afforded by these films is now limited by the magnitude of experimental vibrations and sample flatness; ultimate resolution is governed by the sample/garnet separation. MOI reached its current zenith in 2001 when the first experiment with single vortex resolution was conducted by Goa [36].

3.2.3 Experimental set-up

As touched on in the previous section, a slightly different set-up to that shown in figure 3-6 is employed experimentally in order to accommodate the MOL. The system used in the collection of data presented here is based in the Department of Applied Physics, University of Tokyo. A brief introduction follows but a more thorough description is given elsewhere.[37] A carefully chosen MOL (with high V) is placed in intimate contact with the sample providing a suitable region for the *Faraday rotation* to occur. The experimental set-up is described in figure 3-7. The sample or sample substrate is held in place on a copper puck with a small amount of Apiezon grease. Three or four "pillars" of vacuum grease are carefully placed around the sample using a thin gauge copper wire. These "pillars" will support the garnet film so it is critical that they stand proud of the sample. The advantage of this method is that the vacuum grease contracts during cooling, pulling the Bi-YIG garnet film into intimate contact with the sample via surface tension. The sample puck is placed in direct contact with the cold flange of a commercial cryo-cooler unit that provides convenient control of temperature down to ≈10K. Optical access is afforded to the sample via a small glass window in the evacuated sample chamber and polarised light is shone onto the sample through the MOL, reflected and passed through a crossed analyser. Any light that makes it through the analyser must have been rotated, and since the rotation is proportional to the presence of a B-field, the stray fields at the sample surface can be mapped. A CCD (Charge-coupled device) camera and microscope optics capture the intensity map of the reflected and rotated light, and

powerful image acquisition software allows the user to observe flux penetration in real-time. In practice, *difference images*; subtractions of two images captured at different applied fields, yield more informative results as they elimate unwanted artefacts, such as scratches and blemishes in the MOL. The critical parameters: analyser angle, exposure time and image averaging can be adjusted to optimise conditions. An additional feature of this technique is the necessity of a small transverse field (≈2-3 Oe) to ensure the in-plane magnetisation of the Bi-YIG film. The garnet domain structure is different after each cool-down cycle and frequently proves problematic. If any domains cover regions of interest they are removed by simple tweaking of the in-plane field. This is achieved by manually adjusting the azimuthal angle of $\mathbf{B}_{//}$ with the turntable mounted Helmholtz coils, shown schematically and in the photograph in figure 3-7 (b) and (c).

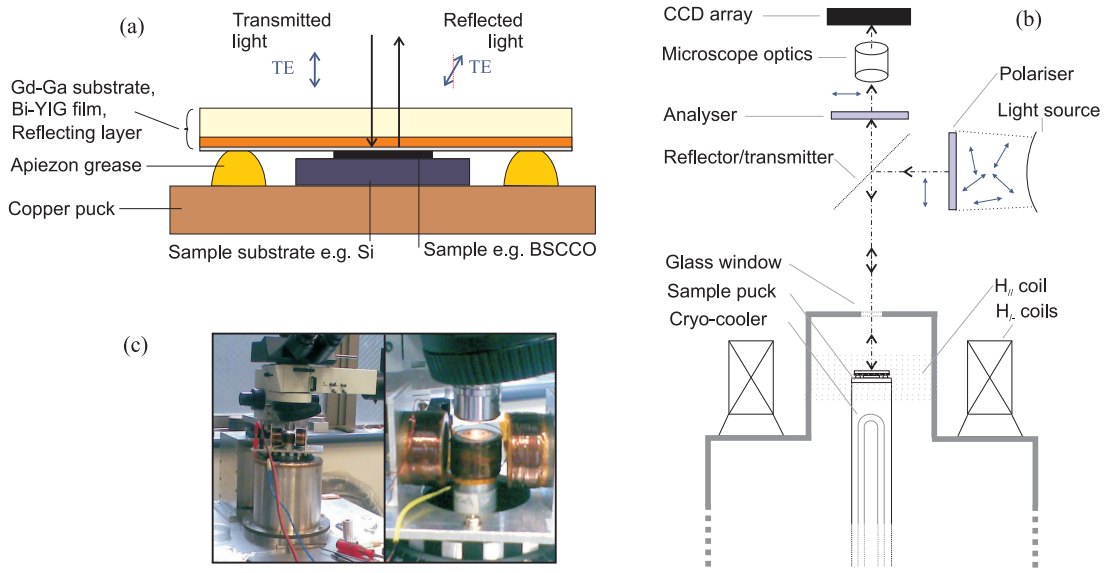

Figure 3-7: Experimental magneto-optical imaging. (a) Schematic of a sample mount. The sample substrate is secured on the copper puck (r≈1cm) with a small amount of vacuum grease (not shown) and the garnet film is then secured on top using carefully placed vacuum grease "pillars". The pillars contract during cooling, pulling the garnet into intimate contact with the sample. *Faraday rotation* occurs as light propagates through the Bismuth-doped Yttrium Iron garnet layer. (b) Schematic of the whole system. Incident light is plane polarised and directed onto the sample through a glass window. The reflected light passes through to a CCD array via a crossed polariser. The intensity of light incident on the CCD is dependant on the size of the *Faraday rotation*, and therefore is a strong function of magnetic field. Two opposing Helmholtz coils mounted on a rotatable turntable allow application of small in-plane fields crucial for MOI. c.f. 3.2.2. (c) Photographs of the experimental set-up.

Chapter 4

Vortex imaging in superconducting Sr_2RuO_4 single crystals

4.1 Motivation

Unconventional superconductors are those in which Cooper pairs of electrons occur with unusual symmetries (c.f. 2.7), and are of major interest to researchers in the field because of the potential for discovering new binding mechanisms that are radically different to the electron-phonon interaction of conventional spin-singlet s-wave materials (c.f. BCS theory 2.6). Strontium Ruthenate 214 (Sr_2RuO_4) has a highly two-dimensional layered perovskite structure (figure 4-1) and was discovered to be a $T_c \cong 1.5$K superconductor in 1994 [38]. It has a simliar crystal structure to the famous high-T_c cuprates and was the first perovskite superconductor found without the Cu-O planes that are critical to superconductivity in the high-T_c's. The substitution of Cu with Ru has the dramatic effect of reducing T_c and $\kappa(\approx 2.5)$ by two orders of magnitude from typical cuprate values. Given the combination of low T_c and a complex crystal structure that demands laborious growth techniques, Sr_2RuO_4 is not seen as a viable candidate for conventional applications of superconductivity such as power transmission or superconducting coils etc. However, intense scientific interest lies in the fact that it is a promising candidate host of spin-triplet, p-wave superconductivity. In this

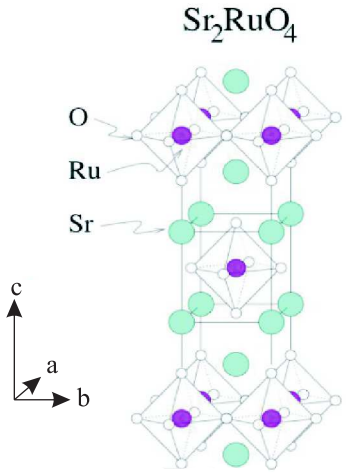

Figure 4-1: Sr_2RuO_4 shares the perovskite structure with the cuprate family of high-temperature superconductors. Ru-O planes take the place of the Cu-O layers in the high-T_c's. A T_c two orders of magnitude smaller (1.5K) than the Cuprates suggest a radically different binding mechanism is facilitating the Cooper pairing

respect Sr_2RuO_4 is by no means unique, spin-triplet superconductivity is thought to exist (with varying degrees of confidence) in: UPt_3,[39], $(TMTSF)_2PF_6$,[40], UGe_2,[41], URhGe,[42] and $ZrZn_2$.[43] Of this list, Sr_2RuO_4 provides perhaps the best opportunity for probing and understanding a spin-triplet superconducting system owing to the large, extremely pure single crystals produced by modern growth techniques. In addition to the prospect of investigating an alternative binding mechanism for the Cooper pair, the actual pairing is thought to be a unique and exotic form of *chiral* p-wave pairing that is predicted to give rise to a plethora of exciting phenomena such as Majorana fermions, particles that are their own anti-particles.[44] Much excitement is centred on the fact that such particles display non-Abelian statistics,[45] and could potentially find application as qubits in quantum computers.[46]

The current evidence indicating that the order parameter in Sr_2RuO_4 is chiral is strong, but a few outstanding questions remain. Such a system is predicted to host several exotic features such as chiral domain walls (CDWs) which, along with sample edges, should produce spontaneous fields (c.f., following section for an in depth discussion). The lack of real-space experimental evidence for these "smoking gun" signatures, which are linked to the observed TRSB in other measurements, is a major challenge for this field.[47, 48, 49, 50] Considerable uncertainty remains over the upper and lower bounds on possible chiral domain sizes, the expected signal strength and reasons for their apparent absence, as summarised in a recent review.[51] Artificially engineered pinning sites promise to overcome

some of these problems by trapping domain walls in known locations and increasing the probability of their observation. An array of holes $\approx 1\mu$m wide, $\approx 1\mu$m deep, micromachined into the a-b face of a single crystal by focussed ion beam milling returned a null result, but as these holes failed to trap single vortices, their effectiveness as pinning centres was questioned by the authors.[52] In this series of measurements a slightly different approach was taken and investigations of mesoscopic disks fabricated on the a-b surface of a Sr_2RuO_4 single crystal are presented in addition to imaging of unpatterned single crystals. The behaviour of vortices in mesoscopic samples is interesting in its own right, but here we combine the fertile ground of mesoscopic superconductivity with the sharp edges and pinning sites predicted to host interesting phenomena in Sr_2RuO_4.

It is against this rather uncertain background of disagreement between theory and experiment that the series of scanning Hall probe microscopy experiments described here was conducted. Section 4.4 presents results obtained from an unpatterned Sr_2RuO_4 single crystal and section 4.5 contains results of subsequent measurements on mesoscopic disks. The following section (4.2) introduces the theory of the chiral order parameter in more detail.

4.2 Theory of chiral spin-triplet pairing symmetry in Sr_2RuO_4.

Theoretical suggestions that Sr_2RuO_4 is a good candidate for spin-triplet pairing (parallel spins) mediated by ferromagnetic spin fluctuations emerged immediately after its discovery due to the occurrence of ferromagnetism in the closely related compound $SrRuO_3$.[53] The results of several experiments have subsequently supported this picture. The strong suppression of T_c by non-magnetic impurities indicated an unconventional non s-wave pairing [54] and subsequent NMR measurements of the Knight shift [55] and polarized neutron scattering [56] provided further strong evidence for spin-triplet superconductivity. For triplet pairing, p-wave order is most likely, although higher order odd pairing is also possible. Of the large number of possible p-wave states, five possible unitary order parameters are consistent with the D_{4h} point group symmetry of Sr_2RuO_4's perovskite lattice.[57] The detection of the spontaneous generation of flux in

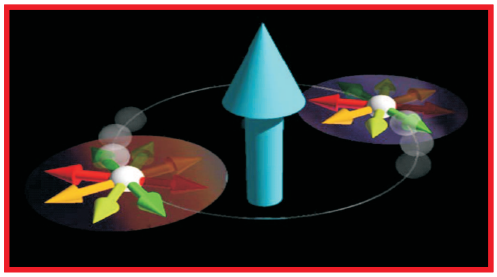

Figure 4-2: A schematic representation of the chiral p-wave order parameter ($d = \Delta_0(k_x \pm ik_y)\hat{z}$ in d-vector notation) that is believed to exist in Sr_2RuO_4. The electrons (white spheres) orbit a common centre of mass with angular momentum $\pm\hbar$ (large arrow) depending on the direction of rotation. The electron spins (small arrows) are parallel and lie in the plane of rotation.

μSR measurements below T_c [58] and later polar Kerr effect measurements in the superconducting state [59] pointed to the presence of time-reversal symmetry breaking (TRSB) in this material. This, in turn, implicates the two component chiral order parameter with d-vector $\hat{d} = \Delta_0(k_x \pm ik_y)\hat{z}$, pictured schematically in Fig. 4-2. In this scenario, the electrons (white spheres) have angular momentum of $\hbar$ and have degenerate states that orbit a common centre of mass in either direction, captured in d-vector notation as $\pm ik_y$. Samples can therefore form multiple domains of either chirality separated by chiral domain walls (CDWs). Even though CDWs have an energetic cost they can nucleate during cooling through T_c and be pinned by sample inhomogeneities and dislocations. More recent phase-sensitive measurements on Sr_2RuO_4 SQUIDs [60] and Josephson junctions [61] have supported the p-wave order parameter scenario, although the latter authors needed to invoke complex static and dynamic chiral domains to explain their data.

4.2.1 Spontaneous chiral fields

Since the Cooper pair carries angular momentum in the p-wave pairing state a characteristic signature of it would be the presence of spontaneous currents anywhere that translational symmetry is broken (e.g., at sample edges and chiral domain walls) as illustrated by the sketch in figure 4-3. These spontaneous currents should form on a lengthscale of the coherence length, ξ, and, although they will be screened by counter-propagating currents over the longer lengthscale of

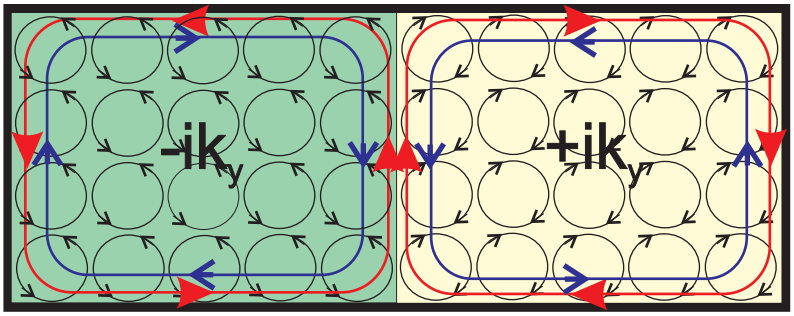

Figure 4-3: A chiral spin-triplet superconductor (black rectangle) can split into degenerate chiral domains where the Cooper pairs rotate with opposite sense. The broken translational symmetry at sample edges and chiral domain boundaries results in incomplete orbits and finite supercurrents that flow within ξ of the edge/domain wall (red line) and are screened by Meissner currents within a distance λ (blue line).

λ, should still generate readily detectible magnetic fields.[62, 63]

Exact numerical solutions to the inhomogeneous London equations of Matsumoto and Sigrist (M&S) are complex and cumbersome to derive.[62] Instead, figure 4-4 presents simulations of the stray fields we would expect to measure at chiral domain walls (CDWs) and chiral edge fields (CEFs) based on the fitting protocol of Bluhm[63] described by equation 4.1.

$$B_z(z=0)(x) = \frac{B_0}{1-\frac{\tilde{\xi}^2}{\tilde{\lambda}^2}} sgn(x)(e^{-\frac{|x|}{\tilde{\lambda}}} - e^{-\frac{|x|}{\tilde{\xi}}}), \tag{4.1}$$

where $\tilde{\lambda} = 2.2\xi$, $\tilde{\xi} = 1.5\xi$, B_0 is a fitting parameter and $sgn(x)$ is the *sign* funtion equal to: $-1(x < 0)$; $1(x > 0)$. Equation 4.1 strictly applies to fields at a CDW, CEFs are estimated by truncating the associated supercurrent ($J_y = 1/\mu_0 \nabla \times \mathbf{B_z}$) to zero for $x > 0$.

The M&S equations, and Bluhm's fit to them, predict the fields at the surface of the superconductor and so these fits are propogated to a height (z) using the well known relation,[64]

$$\tilde{B_z}(k_x, k_y, z) = \tilde{B_z}(k_x, k_y, z=0)e^{-kz}, \tag{4.2}$$

where $\tilde{B_z}$ is the two-dimensional fourier transform of B_z.

Additionally, fields at the surface are expected to be reduced from the bulk

values due to Meissner screening effects and so a further correction is made to account for this following the method of Kirtley *et al*,[48] as contained in equation 4.3 below where $k = \sqrt{k_x^2 + k_y^2}$ and $K = \sqrt{k^2 + \lambda^{-2}}$.

$$\tilde{B}_z(k_x, k_y, z) = \frac{K}{k + K}\tilde{B}_z(k_x, k_y, z = 0)e^{-kz} \tag{4.3}$$

Combining equations 4.1 to 4.3 and averaging over the Hall probe active width w, we arrive at the final equations used to model the CDW (4.4) and CEF (4.5) plotted in figure 4-4 where the field profiles have been evaluated over 100 integration steps in reciprocal space.

$$\begin{aligned} B_z^{CDW}(x, z) = \frac{B_0}{1 - \tilde{\xi}^2/\tilde{\lambda}^2} \cdot \frac{1}{2\pi w} \times \\ \int_{x-\frac{w}{2}}^{x+\frac{w}{2}} \int_0^{100} \left(\frac{2k}{\tilde{\lambda}^{-2} + k^2} - \frac{2k}{\tilde{\xi}^{-2} + k^2} \right) \times \\ \left(\frac{\sqrt{k^2 + \lambda^2}}{|k| + \sqrt{k^2 + \lambda^2}} \right) \cdot \sin(kx) \cdot e^{(-|k|z)} dx dk \end{aligned} \tag{4.4}$$

$$b_z^{cef1} = \int_{x-\frac{w}{2}}^{x+\frac{w}{2}} \int_0^{100} \left(\frac{-1}{1 + k^2\tilde{\lambda}^2} - \frac{-1}{1 + k^2\tilde{\xi}^2} \right) \left(\frac{\sqrt{k^2 + \lambda^{-2}}}{|k| + \sqrt{k^2 + \lambda^{-2}}} \right) \cdot \frac{\sin(kx)}{k} \cdot e^{(-|k|z)} dx dk \tag{4.5a}$$

$$b_z^{cef2} = \int_{x-\frac{w}{2}}^{x+\frac{w}{2}} \int_0^{100} \left(\frac{\tilde{\lambda}}{1 + k^2\tilde{\lambda}^2} - \frac{\tilde{\xi}}{1 + k^2\tilde{\xi}^2} \right) \left(\frac{\sqrt{k^2 + \lambda^{-2}}}{|k| + \sqrt{k^2 + \lambda^{-2}}} \right) \cdot \cos(kx) \cdot e^{(-|k|z)} dx dk \tag{4.5b}$$

$$B_z^{CEF}(x, z) = \frac{b_z^{cef1} + b_z^{cef2}}{2\pi} \cdot \frac{B_0}{1 - \tilde{\xi}^2/\tilde{\lambda}^2} \tag{4.5c}$$

Figure 4-4 contains plots of the above equations for a CDW and CEF where we have assumed $\lambda = 150nm$ and $\xi = 66nm$ and an active Hall probe width of 600nm, a scan height of 0.8μm and adopted Bluhm's fit parameters $\tilde{\lambda} = 2.2\xi$ and $\tilde{\xi} = 1.5\xi$. B_0 is an additional fitting parameter introduced by Bluhm which he took to be 87G in order to match the peak magnitude of the numerical calcula-

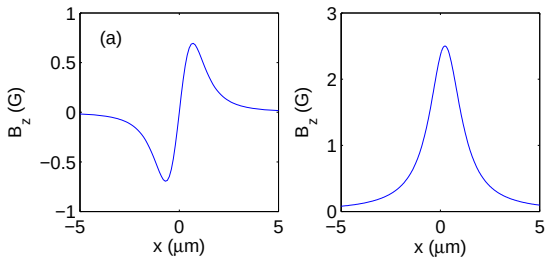

Figure 4-4: Simulations of an experimental Hall probe measurement of stray fields predicted to exist above a chiral p-wave superconductor (c.f. Fig. 4-3) at a height of 0.8μm due to chiral domain walls (a) and chiral edge fields (b) at x=0.

tions.

4.2.2 Unconventional vortex behaviour

In addition to the chiral fields, several other signatures are thought to exist that would corroborate the chiral p-wave order parameter in Sr_2RuO_4. Time-dependent two-component Ginzburg-Landau (TCGL) simulations [65] suggested that vortex ordering phenomena in a system of chiral domains in an applied c-axis magnetic field might also reflect the underlying domain structure. In their simulations these authors found that domain walls weakly pin the magnetic flux and vortices preferentially enter domains of one chirality and eventually move domain walls to expel the reverse domain as illustrated in figure 1 of Ichioka *et al*[65], a version of which is reproduced here in figure 4-5. They even observed the formation of a few 4π vortices (yellow dots) at the boundary of their sample which are essentially vortices containing two flux quanta. To date none of these predictions has been experimentally confirmed.

In contrast to these null results, neutron diffraction [66] and μSR [67] experiments have observed a stable square vortex lattice over most of the H-T phase space investigated in agreement with the prediction of two-component Ginzburg-Landau (TCGL) calculations including Fermi surface and order parameter anisotropies.[68] Such an arrangement is by no means unique in superconductivity but a specific prediction of the TCGL calculations, as yet unconfirmed

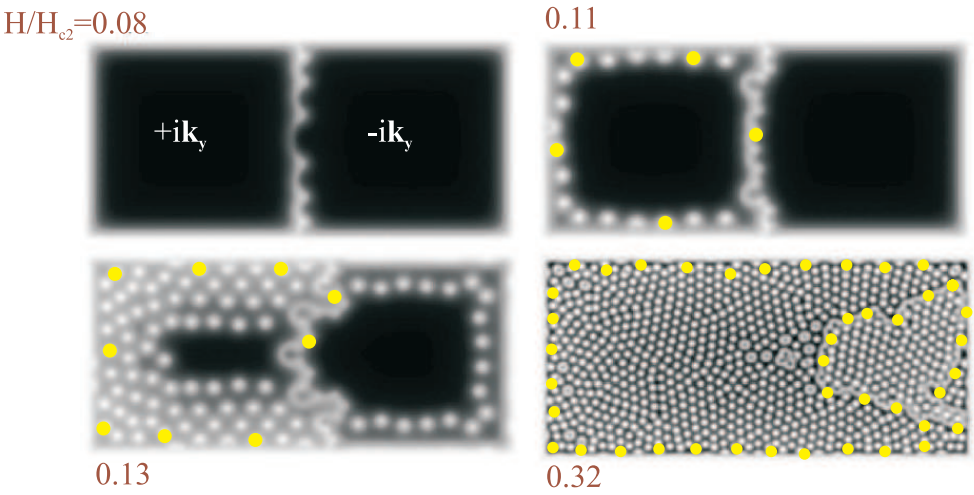

Figure 4-5: Time-dependent Ginzburg-Landau simulations of the vortex behaviour in a chiral spin-triplet superconductor. With increasing field, vortices enter along a chiral domain wall and preferentially populate one domain, eventually sweeping the CDW out of the sample. 4π vortices containing two flux quanta periodically line the sample perimeter (larger solid dots). This figure is a partial reproduction of figure 1 in Ichioka *et al.*[65]

by experiment, is the existence of a field driven transition of the vortex lattice from triangular to square at low fields as illustrated in figure 5 of Heeb and Agterberg[68], reproduced below in figure 4-6.

4.3 Experimental method

Superconducting single crystals were grown using the floating-zone technique with Ru self-flux in a commercial image furnace,[69] and annealed in air (1500 C for 3 days) to remove lattice defects and reduce vortex pinning. [70] Scanning Hall probe imaging has been performed on many different crystals from different growth batches. Section 4.4 presents results on two samples, grown under nominally identical conditions in different growth batches, that illustrate the extremes of behaviour observed. We attribute the pronounced differences in the vortex structures observed in the two crystals to slightly different Ru compositions in the two growth ingots. Figure 4-7 shows the real and imaginary components of ac susceptibility measurements on the two samples. The real part, $\chi^{'}$, indicates that $T_c \cong 1.5K$ in both cases with sample 2 displaying a slightly broader transi-

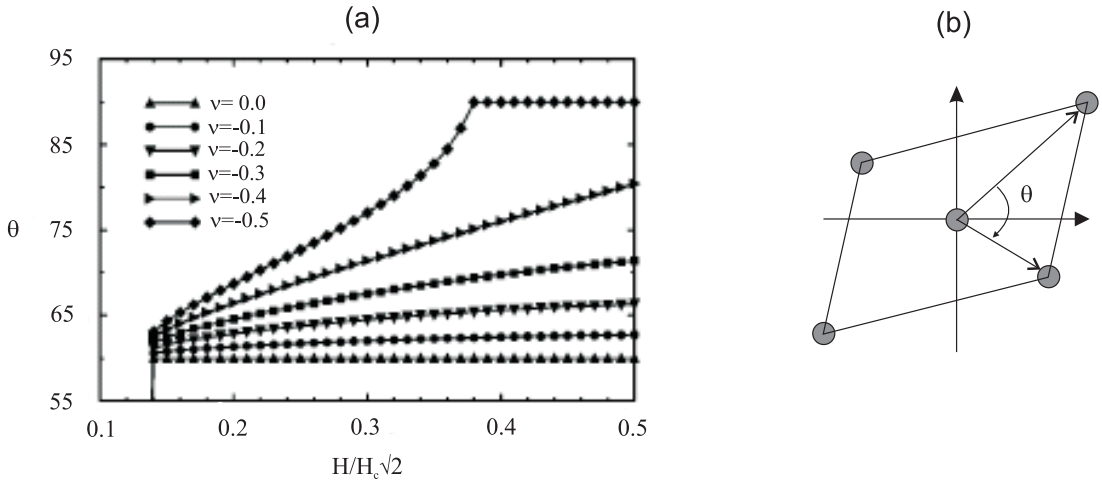

Figure 4-6: Theory of vortex ordering in a chiral spin-triplet superconductor predicts a field-driven transition of the vortex lattice from triangular to square order. The transition is sensitive to anisotropy of the Fermi surface (ν). Modified from figure 5 from Heeb and Agterberg.[68]

tion and slightly lower T_c. This trend is clearer in the imaginary component of susceptibility, χ'', plotted in the inset, which shows a clear shoulder in sample 2 in the range T=1.3-1.4K, indicative of the presence of small amounts of a second phase.

Due to the higher quality of sample 1 it was used for the extension of this work to mesoscopic disks. An array of shallow cylindrical pillars were etched into the cleaved a-b surface to a depth of 400nm using optical lithography and Argon ion milling techniques. Figure 4-8 contains an optical micrograph of the array of disk which have diameters (D) of 5, 10, 15 and 20 μm.

All of the following SHPM images have been captured above the a-b surface of Sr_2RuO_4 single crystals with the magnetic field applied parallel to the c-axis. If the field is increased after cooling through T_c the sample enters the critical state and flux enters the field of view through complex dynamics. Such flux jumps inhibit critical analysis of the vortex physics in Sr_2RuO_4 over the small field step sizes we wish to investigate. For this reason all of the following measurements involve a field-cooling protocol which allows the formation of flux patterns that more accurately reflect the equilibrium state.

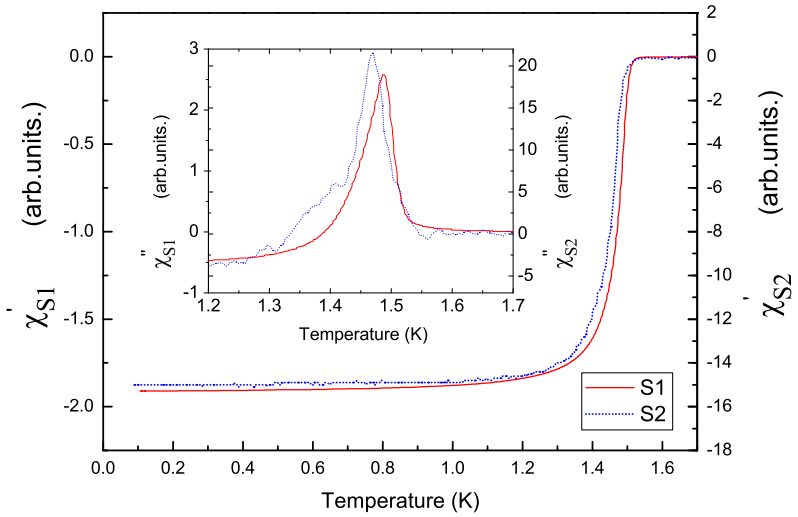

Figure 4-7: The real part of ac susceptibility ($\chi^{'}$) data measured through the critical temperature of the two crystals studied here. The inset shows the imaginary part of the ac susceptibility near T_c.

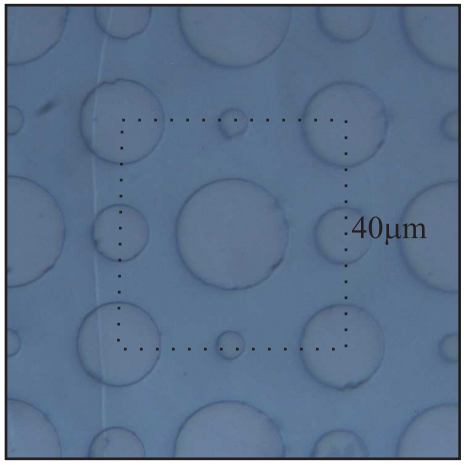

Figure 4-8: An optical micrograph of the mesoscopic disc array etched into the a-b face of the Sr_2RuO_4 single crystal. The disks have diameters of 5, 10, 15, 20 μm and a height of 400nm.

4.4 Vortex imaging and vortex lattice transitions in Sr_2RuO_4 single crystals

4.4.1 Results

Sample 1

Sample 1 has the highest critical temperature (T_c=1.5K) and a very sharp superconducting transition and is expected to exhibit the properties of a very highly ordered Sr_2RuO_4 single crystal. Fig. 4-9(a) shows a family of SHPM images captured parallel to the a-b crystal face, after field cooling to T≈300mK from above T_c (H // c-axis) in various cooling fields spanning H=0. A detailed analysis reveals no credible evidence for the presence of spontaneous currents/fields in these images for H≈0, nor indeed in any other of the several different regions of the sample explored. Hence we conclude that, if they are present, chiral domain walls are not observable within our experimental resolution. In practice the STM-tracking technique used here prevents us from mapping images across the edge of the crystal, so we are unable to draw any conclusions about the possible presence of spontaneous edge currents.

Recent scanning Hall [50] and SQUID [47, 71, 49] microscopy images from Sr_2RuO_4 single crystals have been interpreted in terms of vortex coalescence arising, possibly, from a weak long range vortex attraction at low fields. A careful analysis of all the images captured on sample 1 revealed no statistically significant evidence for clustering in the vortex patterns at low applied fields (Fig. 4-9(a)). To illustrate this point Fig. 4-9(b) presents a statistical analysis of nearest neighbour vortex-vortex distances after Delaunay triangulation of the image at 3.5 Oe. These data are well described by a single Gaussian fit, with no evidence for a second peak at short separations which would indicate the presence of vortex clustering.

Fig. 4-9(c) shows a fit to the profile across a well-isolated vortex measured at H = 0.2 Oe (see inset) based on the Clem variational model[72] modified to account for surface screening effects using an approach due to Kirtley *et al*,[48] (c.f., section 4.2.1) and assuming a variational coherence length ξ_v=66nm, λ=165nm and an active Hall probe width, w, of 600nm.

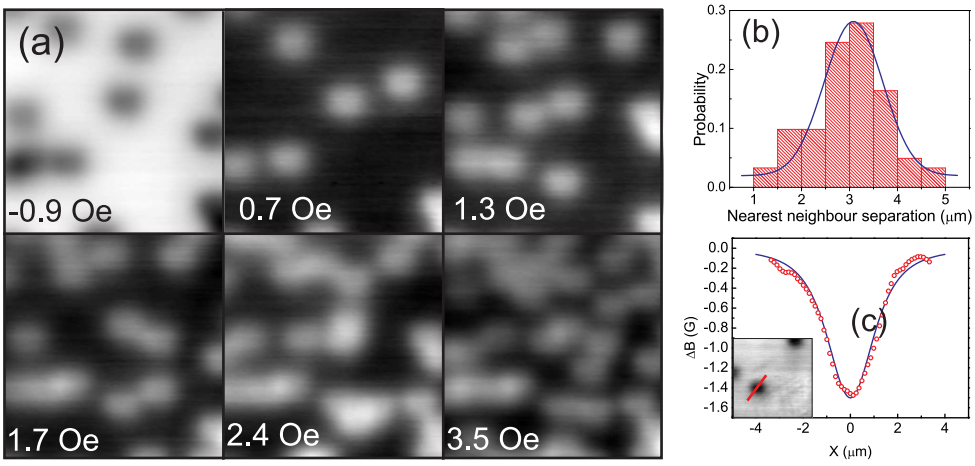

Figure 4-9: (a) SHPM images captured parallel to the a-b face of sample 1 after field-cooling from above T_c in the indicated applied fields (H // c-axis). Scan size $\approx$14μm $\times$ 14μm, T=330mK. (b) Statistical distribution of nearest-neighbour vortex distances for the image at H=3.5 Oe. The solid line is a Gaussian fit to the data (mean=2.95μm, σ=0.8μm). (c) Line profile across a well-isolated vortex in an image captured at H =0.2 Oe (see inset). The solid line is a fit to the Clem variational model with ξ_v=66nm, λ=300nm, w=600nm and h=0.8μm.

$$B(x,y,z) = \frac{\phi_0}{w^2}\int_{y-\frac{w}{2}}^{y+\frac{w}{2}}\int_{x-\frac{w}{2}}^{x+\frac{w}{2}}\int_{0}^{\infty}\frac{K_1\left(\sqrt{k^2+\lambda^{-2}}\xi_v\right)}{2\pi\lambda\left(\sqrt{k^2+\lambda^{-2}}+k\right)K_1\left(\xi_v/\lambda\right)} \times J_0\left(k\sqrt{x'^2+y'^2}\right)exp\left(-kz\right)kdkdx'dy', \quad (4.6)$$

where z is the sensor-sample separation. High field images (>20 Oe) captured during the same sequence that contained the isolated vortex scan demonstrated a spatial resolution of 0.8μm, which constitutes an upper-limit on z, c.f. section 3. Using z = 0.8μm, a good fit to the vortex profile was only achieved with λ =300nm. This is $\sim$2 times greater than estimates from the literature and it appears, therefore, that there is some as yet unexplained vortex broadening that is not included in the Clem model.

As we increase the applied field (H // c-axis) above 4 Oe we witness the emergence of first triangular and then square vortex order out of the essentially random low field distributions shown in Fig. 4-9(a). This is illustrated in Fig.

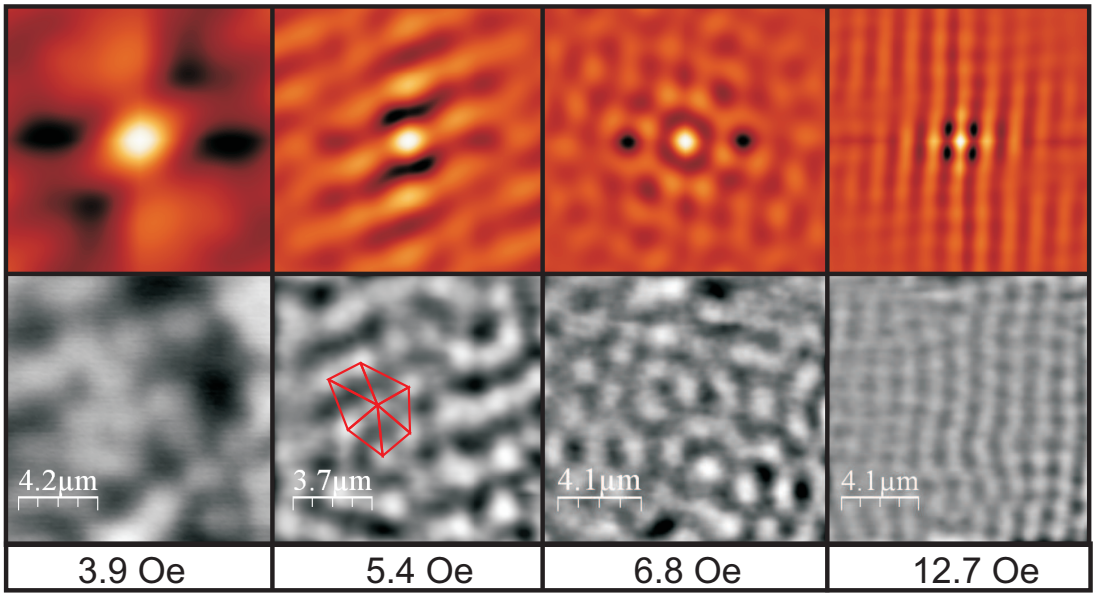

Figure 4-10: SHPM images captured parallel to the a-b face of sample 1 after field-cooling from above T_c in the indicated applied fields (H // c-axis). Scan size $\approx$14μm$\times$ 14μm, T=330mK. The upper row shows self-correlation plots of the raw images in the bottom row (vortices are white).

4-10 where we present direct SHPM images in tandem with their self-correlation (SC) plots, which are particularly useful tools for characterising vortex order. The first image at 3.9 Oe shows a rather random distribution of weakly pinned vortices, a fact reflected in the broadly featureless SC plot. However, upon increasing the field to just 5.4 Oe we start to see a pronounced degree of triangular order as evidenced by the hexagon of six bright spots in the centre of the SC plot (c.f., also the region of hexagonal mesh superimposed on the raw vortex image). This reflects the emergence of the usual triangular Abrikosov vortex lattice driven by vortex-vortex repulsion. Surprisingly the triangular lattice is lost again at 6.8 Oe when there appears to be some competition between two competing forms of order. Indeed for yet higher applied fields we find a transition to a square vortex lattice, which is almost complete in the rather well-ordered image shown at 12.7 Oe.

Figure 4-11 (a) shows that we observe a weakly disordered square vortex lattice with the same orientation as we increase the field further up to about 35 Oe where we lose the ability to resolve discrete vortices. Note that the lattice periodicity is clearer in the fast x-scan direction than the slow y-scan direction

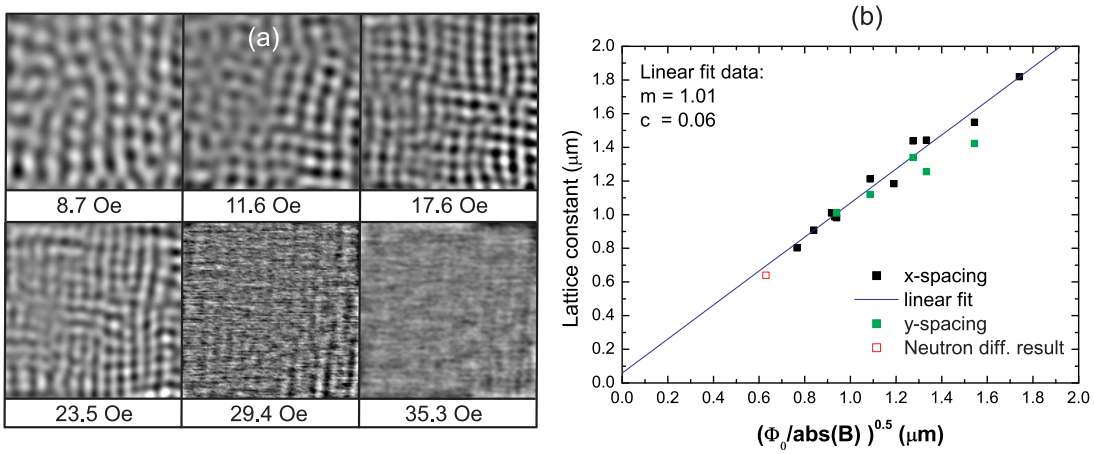

Figure 4-11: (a) SHPM images captured parallel to the a-b face of sample 1 after field-cooling from above T_c in the indicated applied fields (H // c-axis). Scan size ≈14μm × 14μm, T=330mK. (b) The square lattice spacing measured in the x- and y-scan directions plotted versus $(\Phi_0/|B|)^{0.5}$. The solid line is a linear regression fit to these data. Also shown (open square) is the lattice spacing estimated from neutron diffraction experiments at H =50Oe.[66]

at high fields due to the dominant low frequency noise in our Hall sensors. This gives the impression of vertically aligned vortex stripes or chains but after averaging several adjacent y-lines the underlying periodicity is revealed. Fig. 4-11(b) shows plots of the experimentally estimated lattice spacing for both x and y scan directions plotted as a function of $(\Phi_0/|B|)^{0.5}$. Linear regression of these data yield a fit with slope m=1.01 and y-axis intercept c=0.06μm, in excellent agreement with the expected line of unity slope passing through the origin for a perfect square vortex lattice. Also plotted on the figure are the lattice spacing inferred from neutron diffraction data at the lowest field measured.[66] The fact that the lattice spacing in both x- and y-scan directions lies on the same fit line, within the resolution of our experiment, also appears to rule out rectangular ordering, at least in fields up until 35.3 Oe.

Sample 2

The lower quality sample 2 ($T_c \cong$ 1.5K with a broader superconducting transition) displays markedly different behaviour to sample 1, even though both crystals were nominally grown under the same conditions. Fig. 4-12 shows two composites of several individual images captured at H=2.4Oe (a) and 15.7Oe (b). At low fields

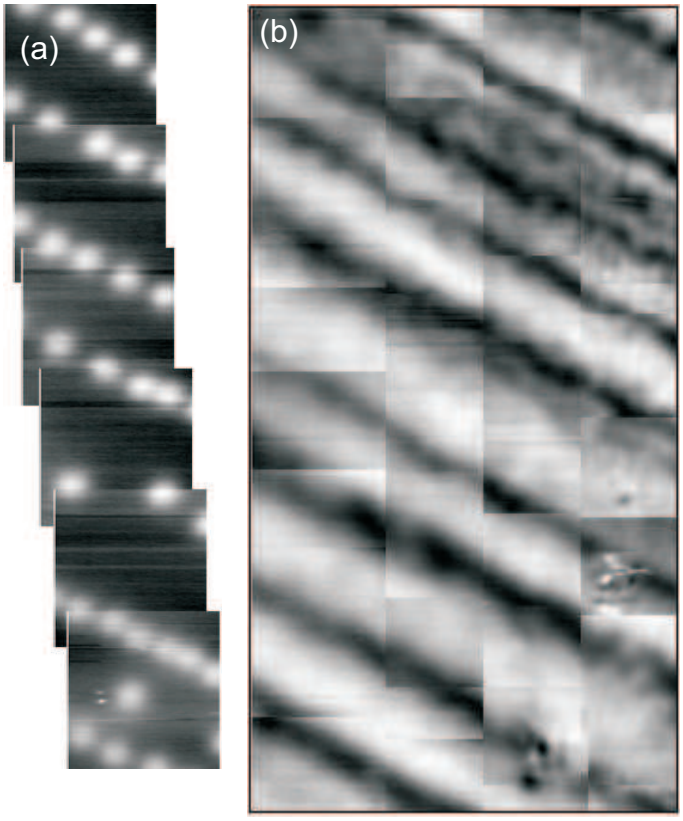

Figure 4-12: Composite SHPM images captured parallel to the a-b face of sample 2 after field-cooling from above T_c in applied fields (H // c-axis) (a) H=2.4 Oe ($\approx$20μm $\times$ 70μm) and (b) H=15.7 Oe ($\approx$45μm $\times$ 70μm). T=330mK.

(Fig. 4-12 (a)) we see that vortices occupy quasiperiodic chain structures that lie at 23^o (67^o) with respect to the scan axes. The chains are reasonably regularly spaced with a period of $\approx$10μm and are quite inhomogenously populated. At higher fields (Fig. 4-12(b)) these chains expand and form irregular bands.

Fig. 4-13(a) details one of the panels from the composite shown in Fig. 4-12(b) captured at H=15.7 Oe. Vertical chains are clearly visible parallel to the y-scan direction within the bright white vortex bands. Fig. 4-13(b) shows the average of a set of x-scan lines in the rectangular region indicated in Fig. 4-13(a), clearly revealing the presence of these vertical vortex chains. We believe that these short periodicity chains arise due to the same electronic anisotropies that lead to the formation of the square lattice in sample 1.

Figure 4-14 captures the evolution from sparse chains to bands over a broad range of fields until we begin to lose contrast for H>51 Oe. Note that the flux

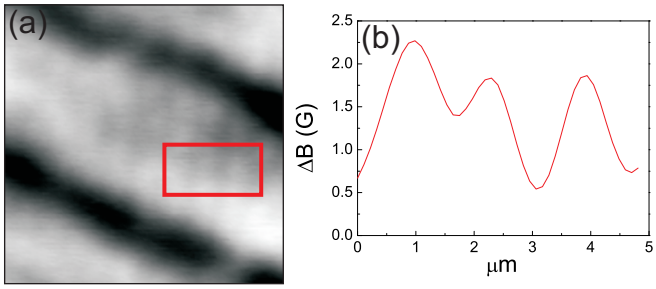

Figure 4-13: (a)SHPM image captured parallel to the a-b face of sample 2 after field-cooling from above T_c in H=15.7Oe (H // c-axis). Scan size ≈14μm × 14μm, T=330mK. (d) Average of the x-scan lines in the region indicated in (a) showing the presence of vortex chains within the bands.

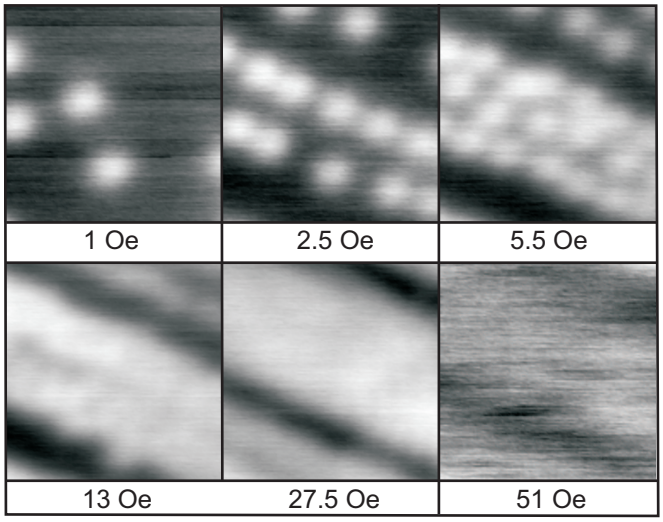

Figure 4-14: SHPM images captured parallel to the a-b face of the same region of sample 2 after field-cooling from above T_c in the indicated applied fields (H // c-axis). Vortices are white, scan size ≈14μm × 14μm, T =330mK. Greyscale (ΔB) spans 1.98G, 2.13G, 1.89G, 2.7G, 2.55G and 0.89G respectively.

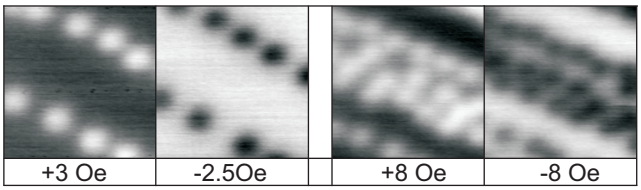

Figure 4-15: SHPM images captured parallel to the a-b face of the same region of sample 2 after field-cooling from above T_c in the indicated applied fields (H // c-axis). Scan size $\approx$14μm$\times$14μm, T =330mK.

expelling areas (black) are gradually squeezed smaller and smaller by increasing the number of vortices in the chains/bands. Note also that the greyscale of the images at high fields is much less than the peak contrast of a single vortex as well as the magnitude of the applied field. Hence we conclude that vortices are present everywhere, but have a lower density on the dark strips than in the bright bands between them.

Theoretical simulations based on time-dependent two component Ginzburg-Landau theory in a system of chiral order parameter domains [65] predict that vortices preferentially enter those domains with a matching chirality, i.e., up and down vortices preferentially penetrate different regions, c.f., section 4.2.2. If we assume that the order parameter is not influenced by small applied fields, an easy test of this prediction is to reverse the field and observe the preferred locations of vortices of opposite sign (c.f., Fig. 4-15). In all cases we see no difference in the preferred vortex locations within the resolution of a single vortex ($< 2\mu m$), which seems to rule out the possibility that the chain/band structure we see reflects an underlying chiral domain structure. Finally we note the interesting tendency for low field chains to be positioned along one edge of the emerging bands, not in the centre as one might expect. As a consequence the vortex bands tend to fill in from one side, and this evolution is the same side for both up and down vortices.

Assuming that the formation of these vortex chains/bands is related to the presence of some form of anisotropic pinning potential it is interesting to study their temperature dependence. The increased thermal energy at higher temperatures should allow vortices to overcome pinning potentials, freeing them up to move closer to their equilibrium configurations. Fig. 4-16 presents a sequence of vortex images captured at different temperatures after field-cooling to 327mK in H=2.4 Oe. As the temperature is increased we see that the mean vortex-vortex

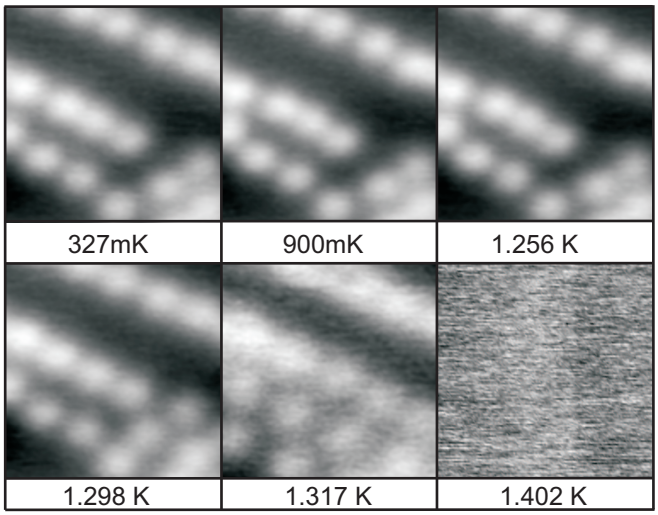

Figure 4-16: Temperature-dependence of SHPM images captured parallel to the a-b face of the same region of sample 2 after field-cooling from above T_c in H=2.4Oe (H // c-axis). Scan size ≈14μm × 14μm.

spacing increases (presumably due to the increasing penetration depth, λ(T)) and the chains broaden into lower density bands. Close to T_c at $T = 1.317K$ we see pronounced triangular vortex ordering, with a complete loss of vortex contrast for $T > 1.4K$.

4.4.2 Discussion

One of the key signatures of a chiral p-wave order parameter, which has so far eluded all real space magnetic imaging experiments, is the presence of spontaneous currents (fields) at sample edges, chiral domain boundaries or crystalline imperfections. The use of STM-based height control in our scanning system prevents us from imaging across the edge of the crystal. However, we find no credible evidence for spontaneous fields that we could attribute to either chiral domain walls or crystal defects anywhere within our samples at very low applied fields.

In figure 4-17 we plot the calculated chiral domain fields for various choices of the fitting parameter B_0, and show that the estimated signal would fall below the RMS noise floor of our measurements (≈0.014G) if, in practice, B_0 was ∼50 times smaller ($B_0 < 1.75G$) than that predicted by current theory. We therefore expect that we should have been able to detect magnetic signals from chiral domain walls with magnitudes as predicted by current theory.[63]

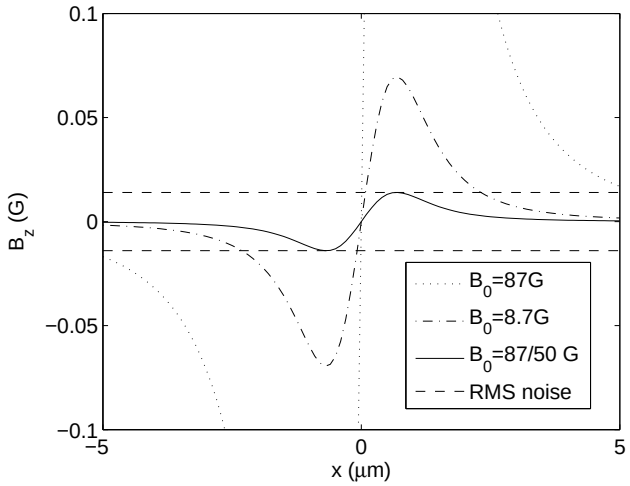

Figure 4-17: Simulations of the stray field along linescans perpendicular to an infinite chiral domain boundary (x-axis origin is at the centre of the wall) based on the fitting protocol of Bluhm[63] who took B_0 to be 87G. The fields have been calculated for various choices of B_0 and the RMS noise floor of our measurements (0.014G) is indicated by horizontal dashed lines.

Furthermore, upon field-cooling in small applied fields we find no evidence for enhanced vortex penetration along chiral domain walls or the preferential occupation of domains of a given chirality, although these phenomena may only become pronounced in zero field-cooled experiments. Very low field vortex structures were typically highly disordered in even the highest quality samples (c.f., Fig. 4-9(a)), and repeated images after field-cooling through T_c in the same field at the same location invariably revealed that the majority of vortices occupied the same positions, suggesting a fairly low density of rather strong pinning sites. Vortex pinning typically occurs anywhere that the superconducting order parameter is suppressed which, in a p-wave superconductor, could occur due to elastic scattering at crystal defects. If this is indeed the origin of the strong pinning forces it is somewhat at odds with other measurements (e.g., de Haas-van Alphen) [73] which find an extremely long carrier mean free path of the order of $\approx 1\mu$m in our best samples. Given that lattice imperfections are predicted to give rise to spontaneous fields we speculate that there could be a link between these strong pinning centres and the "broad distribution of fields from a dilute distribution of sources" detected by the μSR experiments.[58]

It is possible that our field-cooling experimental protocol has suppressed the chiral domain structure in measurements at higher fields. An applied field splits the degeneracy of the $J_z = \pm\hbar$ chiral states and might result in the formation of a predominantly single domain state.[65] This would dramatically reduce our chances of imaging a domain wall in the relatively small field of view available. However, we have performed several experiments in nominally zero field (after applying a small field to compensate for the Earth's field) which also yielded no evidence for domains. Kallin and Berlinsky[51] have carefully analysed all the available experimental data on Sr_2RuO_4 with a view to establishing upper and lower bounds on domain sizes. Estimated values vary dramatically from $< 1\mu$m[61] to $\approx 50\mu$m.[59] Given that there is still much debate about the expected 3D domain structure,[49] possible domain dynamics[61, 59] and the expected magnitude of spontaneous fields[74] it is premature to draw very robust conclusions from our images. Suffice it to say that we have not been able to observe chiral domain walls at lengthscales spanning 0.8μm to $\approx 14\mu$m with minimum detectable fields ≈ 0.014G at timescales slower than $\approx$1s (the time taken to scan a single line of the image).

The spatial resolution of SHPM is limited either by the lateral size of the Hall probe active area or the sample/sensor separation, whichever is greater. In our case we estimate that the active width of our square Hall probe is $\approx$600nm and sample/sensor spacing is likely to be the dominant limiting factor. In a sequence of images taken on the same day as the scan of the isolated vortex, with the same sample/sensor spacing we were able to resolve the square vortex lattice at $H_z \approx$ 35Oe. This clearly sets an upper bound on the actual scan height of $h \lesssim 0.8\mu$m, the vortex lattice spacing at this field. If we fix the scan height in the model to 0.8μm, we find that we need to increase the London penetration depth to $\approx$300nm to get a good fit, $\sim$2 times the accepted value of 165nm-190nm reported in the literature. It appears, therefore, that there is some as yet unexplained broadening in our vortex images that is not accounted for in the modified Clem model. We speculate that this could either be related to the presence of a free surface (e.g., some form of surface scattering) or the traps that act as strong vortex pinning centres. Alternatively it might reflect motional broadening due to vortex fluctuations about their pinning sites.

Vortex "coalescence" in Sr_2RuO_4 has been reported in previous scanning

SQUID imaging experiments.[47, 71, 49] Since the Ginzburg-Landau parameter for Sr_2RuO_4 $\kappa = \lambda/\xi \approx 2.5$ it represents a fairly weakly type II superconductor. Hence it is not inconceivable that the vortex-vortex interaction has a long range attractive component as observed in superconductors with κ close to $1/\sqrt{2}$ by Bitter decoration many years ago [75] or within the two band "Type 1.5" scenario proposed recently for very clean MgB_2 single crystals.[76] In this situation a nearest neighbour analysis of vortex separations will exhibit at least two peaks, one reflecting the intervortex spacing within clusters and one reflecting the inter-cluster spacing. The nearest neighbour separation histogram for the highly ordered sample 1 in Fig 4-9(b) can be well fitted by a single Gaussian curve and we find no evidence for clustering over the length scale of our field of view ($\approx 14\mu$m). In contrast, a similar analysis for images such as those shown in Fig. 4-12(a) for the slightly more disordered sample 2 would show a second peak corresponding to the chain separation. However, we believe that these chains have an extrinsic origin as discussed below, and are not intrinsic to the physics of Sr_2RuO_4.

Vortices in an isotropic s-wave superconductor are expected to arrange in a hexagonal lattice. It is, however, well established that Fermi surface and order parameter anisotropies can lead to other forms of vortex ordering, e.g., a square vortex lattice[57, 77]. Heeb and Agterberg[68] have used an extended London theory ($\kappa \gg 1$) for a two component p-wave order parameter, to investigate the ground state vortex structure in Sr_2RuO_4 as a function of Fermi surface anisotropy, $|\nu| \ll 1$, and applied field. They predict a continuous triangular $\rightarrow$ rectangular $\rightarrow$ square field-driven transition, with switching fields that are strongly dependent on the value of ν. Earlier μSR[78] and SANS[66] measurements have clearly demonstrated the existence of a square vortex lattice at high magnetic fields. The SANS measurements found square ordering everywhere the lattice could be resolved ($H_z > 50Oe$) and we believe that the hexagonal to square transition shown in Fig. 4-10 for the field range $5.4Oe \leq Hz \leq 12.7Oe$ is the first experimental evidence that the vortex lattice in Sr_2RuO_4 does indeed reorder at low fields. The extended London theory of Heeb and Agterberg assumes that $\kappa \gg 1$ and hence does not strictly apply to Sr_2RuO_4 ($\kappa \approx 2.5$) and we are unable to draw any quantitative conclusions about the magnitude of ν. Our observed crossover is at considerably lower fields than in the high κ ($\kappa = 5, \kappa = 25$)

simulations of Heeb and Agterberg, but the same authors note that the crossover to a square lattice would occur at lower applied fields and lower anisotropies for a superconductor with smaller κ.

Finally we discuss the quasiperiodic chaining/banding of vortices observed in sample 2. Some of the images shown in Figs. 4-12→4-16 appear, at least superficially, similar to previous scanning SQUID data from ref. [47] where the possibility of vortex "coalescence" associated with a chiral domain structure is suggested. Several observations lead us to believe that this is not the case in our experiments on this sample. Firstly the 'domain' boundaries we observe are fixed spatially and independent of cooling cycle, whereas one would expect the locations of chiral domain walls to vary randomly after repeatedly field-cooling through T_c. We also see no qualitative change to the quasiperiodic structure after cooling in quite high fields of either sign ($|H_z| \approx 50Oe$) when one would expect the degeneracy of domains to be lifted, favouring a single domain structure. It is possible that the chiral domain walls are strongly pinned, e.g., at lattice defects, but again we see no evidence for spontaneous currents(fields) at very low inductions (c.f., Fig. 4-14) that would indicate their presence. Instead, we speculate that the chaining/banding phenomenon is an extrinsic effect related to details of the growth of single crystal samples. The ac susceptibility data (Fig. 4-7) lend credence to this hypothesis as they show a significant difference in T_c, which is extremely sensitive to crystalline imperfection in an unconventional superconductor,[54] and so provides a good guide to sample quality. Defining T_c as when $\chi^{'}$ falls below 90% of the normal state susceptibility we estimate a $\Delta T_c = 0.012K$ (1.498K and 1.485K for sample 1 and 2 respectively). It is well established that Ru lamellae often arise from eutectic solidification during Sr_2RuO_4 crystal growth.[79] These structures can vary greatly in size and orientation but frequently have dimensions and spacings comparable to the period and width of chains/bands observed here. It is possible, therefore, that type I superconducting Ru lamellae are leading to local flux exclusion and a modulation of the vortex density in the way we observe. Ruthenium has $T_c \approx 0.5K$ and a critical field, $H_c = 69G$. This critical field is consistent with the observation that the banding is almost fully suppressed above $H_z = 51\ Oe$ as shown in Fig. 4-14. However, the critical temperature is too low to explain the chains/bands seen in Fig. 4-16 at $T = 0.9K$ and above. It is well known, however, that there is an interface phase between the lamellar Ru

and Sr_2RuO_4 with a much higher critical temperature of $T_c \approx 3K$[79] and it is possible that this is responsible for the effects we see at elevated temperatures. However, the expected signal is not present in ac susceptibility measurements and it would be hard to explain the complete loss of magnetic contrast far below 3K ($\approx 1.4K$, Fig. 4-16) if this were the case. While the T_c differences could be consistent with the presence of a second phase in the crystal, there are no further signalling features at 0.5K or 3K that indicate its presence. In addition, we have been unable to find traces of a 0.5K Ru phase in heat capacity or bulk magnetometry measurements, and these samples still exhibit very long carrier mean free paths ($\approx 1\mu m$) in de Haas-van Alphen measurements so the chaining/banding behaviour of vortices is very difficult to explain in terms of these two known phases. Lastly, we note that a careful analysis of the series of images illustrated in Fig. 4-14 reveals that the chains of vortices evolve asymmetrically into bands as the field is increased. Initial vortex entry occurs at one edge of the band, not in the centre as one might expect, and the band then fills out towards the low density direction, regardless of whether applied fields are positive or negative. A similar effect can be observed in the higher temperature images of Fig. 4-16. This suggests an asymmetric pinning potential for the vortices, possibly having a sawtooth-like profile along a direction perpendicular to the chains. In addition to these 'extrinsic' effects, we have also detected behaviour that we attribute to the 'intrinsic' underlying physics of Sr_2RuO_4 in sample 2. The chaining of vortices within the bands illustrated in Fig. 4-13(a) presumably arises from the same electronic anisotropies giving rise to a square vortex lattice in sample 1. However, the measured periodicity of these chains at $H_z = 15.7Oe$ (Fig. 4-13(b)) is nearly 40% larger than the expected square lattice spacing at this field (c.f., Fig 4-11(b)). We presume that this is the result of partial flux screening by the source of extrinsic disorder responsible for the diagonal banding. At medium fields (5.5 Oe in Fig. 4-14) there appears to be a degree of triangular ordering in vortex images but this cannot be concluded with any certainty since vortex structures are so heavily influenced by the extrinsic disorder. Finally, we note the transition from chain-like to hexagonal vortex order as the temperature is increased in Fig. 4-16. This suggests that vortex-vortex interactions start to dominate over the disorder potentials at high temperatures. This tendency for hexagonal ordering close to T_c is consistent with μSR measurements at $H_z = 150\ Oe$ which appear

to show a temperature-driven square → hexagonal lattice transition.[78]

4.4.3 Conclusion

We have performed scanning Hall probe magnetic imaging of several high quality Sr_2RuO_4 single crystals. In all cases we have failed to detect any magnetic signals that we can credibly attribute to the spontaneous magnetization predicted for a TRSB order parameter. We conclude that either Sr_2RuO_4 is not a chiral spin-triplet superconductor, or if it is, then chiral domains are formed on a scale below our spatial resolution ($\sim 0.8\mu$m); or the magnetic signal from them is $\sim$50 times smaller than predicted by current theory. Low field vortex distributions are consistent with the existence of strong pinning and we speculate that these pinning sites could be linked to the dilute distribution of field sources detected in μSR experiments.

We find no evidence of vortex clustering in our most highly ordered samples at low fields, but the field profiles of isolated vortices do reveal an unidentified source of broadening. We have resolved a field-driven triangular → square vortex lattice transition in our highest ordered samples at low fields, consistent with extended London theory calculations for a p-wave order parameter.

Slightly less well-ordered samples exhibit pronounced chaining/banding of vortices, which we attribute to an extrinsic sources of disorder, possibly the presence of Ru lamellae. The vortex-vortex interaction appears to dominate over this disorder potential at high temperatures close to T_c where pronounced hexagonal vortex ordering is recovered.

4.5 Vortex imaging and the search for chiral edge currents in mesoscopic Sr_2RuO_4 disks

The SHPM technique makes it difficult to scan over the edges of a single crystal, preventing us from making any statements about the existence of chiral edge fields in these samples. This section presents a series of SHPM measurements undertaken on an array of mesoscopic "disks" etched into the a-b surface of the highest quality sample (sample 1) as discussed previously in this chapter.

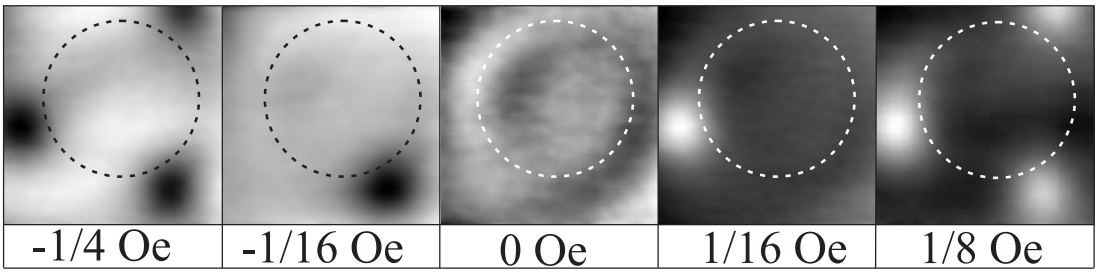

Figure 4-18: A sequence of scanning Hall probe microscope images (14μm $\times$ 14μm) of a mesoscopic Sr_2RuO_4 disk (D=10μm), spanning zero magnetic field. T=260mK. From left to right the grayscales (G) are: 0.6, 0.68, 0.27, 0.63 and 0.66.

4.5.1 Results

The presence of a magnetic field lifts the degeneracy of chiral domains in a $\hat{d} = \Delta_0(k_x \pm ik_y)\hat{z}$ superconductor, potentially resulting in a single domain sample.[80, 74] High enough fields can also rotate the d-vector so that the electron spins lie parallel with the applied field, lifting the degeneracy of $\pm L_z$ orbits.[81, 82] Such occurences would reduce the probability of detecting CDW signals in our samples, should they exist. Therefore, in order to favour the nucleation of chiral domain walls, the applied field was carefully adjusted until contributions from the Earth's field and cryostat remnant fields were carefully cancelled out to achieve as close to a true zero field as possible, as defined by vortex-free single images (14μm $\times$ 14μm). Such a sequence is displayed in figure 4-18 where the scan area has been centered over a D=10μm disk. At small fields, vortices are screened from the disk and nucleate at the edges where they are observed to arrange in an approximately triangular formation. At zero field, a weak magnetic contrast is seen to delimit the disk edge which is shown to be attributable to the gating effect by subtraction of a $T > T_c$ image. The SHPM technique requires the application of a small sample bias ($\sim$0.2V) to aid surface detection via tunnel currents. Owing to the topographic nature of the sample, the electric field present between sample and sensor modulates during scanning and creates an artificial signal known as the gating effect. A definitive test of whether image contrast is a real magnetic feature due to superconductivity, or simply a topographic gating signal is to scan the same area above T_c. Figure 4-19 contains such images and reveals that the feint disk outline observed at H_{eff} =0 is also present above

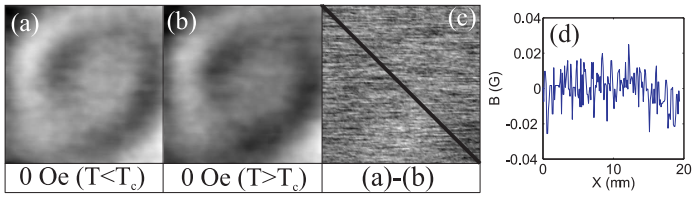

Figure 4-19: SHPM images (14μm $\times$ 14μm) of a Sr_2RuO_4 disk (D=$10\mu m$) in zero field, above [(b) 2.2K] and below [(a) 260mK] T_c. From left to right the grayscales (G) are: 0.27, 0.28 and 0.1. The similarity of the images above and below T_c highlights that any contrast in these images ((a) and (b)) is wholly attributable to the "gating" effect. The linescan of the subtraction (c) confirms the absence of any magnetic signal attributable to spontaneous chiral fields due to edges and domain walls in these images, above the RMS background noise of 0.014G.

T_c. Difference images subsequently confirm that there is no magnetic contrast in the zero field image attributable to chiral edge or domain wall currents above the measurement noise threshold. The background RMS noise of figure 4-9(c) is 0.014 G. A similar analysis was conducted for the 5μm disk and returned the same result.

Figure 4-20 contains images of the 10 μm disk after field-cooling in applied fields increasing up to 1.875 Oe. The number of vortices nucleating at the disk edge increases and the disk becomes clearly visible by virtue of its Meissner screening signature. Eventually, at 1.25 Oe a single vortex penetrates the disk, followed by a second at 1.5 Oe. Similar sequences for all four disk radii allow one to plot the variation of the vortex penetration field (H_p) with disk radius (R). One might expect such a relationship to have the form $H_p \propto (d/R)^{1/2}$ in accordance with several theories of energy barriers to flux penetration, as was shown to be the case for equivalent disk structures in the high-temperature superconducting system BSSCO-2212.[83, 84] Figure 4-21 displays H_p versus $(d/R)^{1/2}$ and, although the data set is limited with only four data points (some of which are subject to rather large error bars) it is clear that a straight line fit through the origin is not possible. In fact any linear fit would have a negative intercept that suggests H_p is 0 for disks above a certain critical radius, a situation that seems unphysical.

The influence of the disk edges on the vortex configuration is captured in the images of a 20μm disk shown in figure 4-22. 5 vortices are seen to form a pentagon at the centre of the disk, reflecting the symmetry of the mesostructure

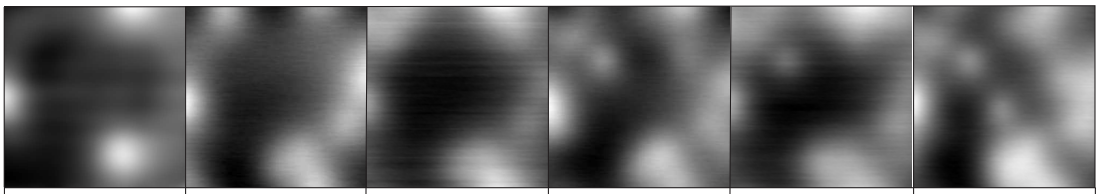

Figure 4-20: A sequence of SHPM images (14μm $\times$ 14μm) of a mesoscopic Sr_2RuO_4 disk (D=10μm) after field-cooling to T=300mK in magnetic fields up to 1.875 Oe. The penetration of individual vortices into the disk is captured at intermediate fields. T=260mK.

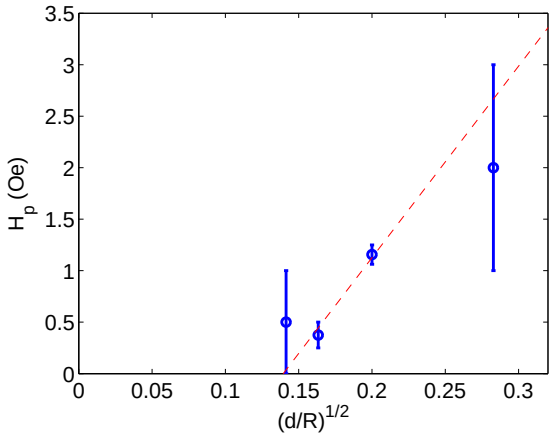

Figure 4-21: The field of first vortex penetration (H_p) into mesoscopic Sr_2RuO_4 disks versus $R^{-1/2}$ is plotted for comparison with the expected trend for energy barriers to flux entry.

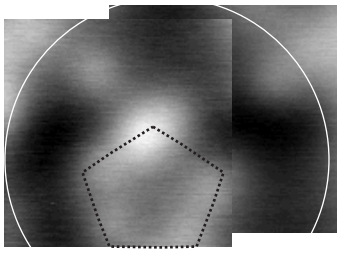

Figure 4-22: At low fields (1 Oe) sample boundaries are seen to influence the vortex configuration. Here several vortices form a pentagon at the centre of a 20 μm disk. T=1K.

in what looks like a discrete analog of Zeldov's continuous flux dome,[85] that is predicted to occur as a consequence of the *geometrical barrier* (GB). Presumably in this instance, the increased measurement temperature liberates vortices from any pinning sites, allowing them to form a configuration that reflects their mutual repulsion from each other and from Meissner currents flowing at the disk edges.

Returning to the 10μm disk, as the applied field is increased further up to 100 Oe (figure 4-23) a greater amount of flux penetrates the disk. At 20 Oe, even though the disk is presumed to be completely saturated with vortices, a rather inhomogeneous flux distribution is captured which is suggestive of the presence of strong bulk pinning forces in the sample. Then surprisingly, at 25 Oe the flux distribution inside the disk suddenly becomes completely homogeneous, within the resolution of the experiment. Flux continues to enter the disk homogeneously all the way to the highest measurement field of 100 Oe. The grayscale values shown in the caption of figure 4-23 illustrate the strength of the screening and are appreciably higher than single vortex value of $\sim$0.65 G for this experiment.

Linescans across the disk at the four highest fields (when the apparent flux distribution has become homogenous) reveal a steep edged and flat bottomed "top hat" shape to the field profile (fig. 4-24). Theoretical comparisons have been made by following the method of Clem and Sanchez,[86] whose model of the critical state in microscopic disks (equation 4.7) predicts that at these field strengths, and in these disks, the bulk critical current density J_c is flowing throughout the sample.[86]

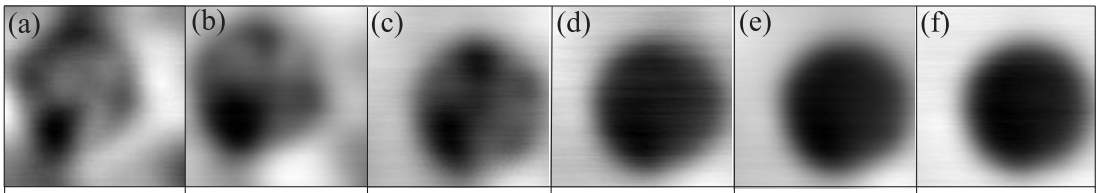

Figure 4-23: A sequence of SHPM images (14μm $\times$ 14μm) of a mesoscopic Sr_2RuO_4 disk (D=10μm) after field-cooling in magnetic fields up to 100 Oe. Penetrated flux forms a inhomogeneous distribution in the disk at fields $\leq$20 Oe. For fields $\geq$25 Oe flux appears to enter the disk homogenously. The screening strength peaks at $\sim$20 to 25 Oe and gradually falls with increasing field, as illustrated by the respective grayscale values (G): 2.97, 3.6, 4.08, 3.7, 3.48, 2.33.

$$J(r) = -\left(2\frac{J_c}{\pi}\right) \cdot \arctan\left[\left(\frac{r}{R}\right) \cdot \frac{\sqrt{R^2 - a^2}}{\sqrt{a^2 - r^2}}\right] \tag{4.7}$$

J(r) is the supercurrent density profile of a disk of radius R, J_c is the bulk critical current density, a parameter of the model, and a describes an annulus of inner radius a and outer radius R where J_c flows and penetrated flux resides.

$$a = \frac{R}{\cosh\left(2 \cdot \frac{H_a}{\mu_0 J_c d}\right)} \tag{4.8}$$

For the applied fields and disk geometry concerned here, a$\approx$0 and the disk is saturated with supercurrent density J_c. Continuing with the method of Clem and Sanchez, the resulting field profile is evaluated from the supercurrent density profile via a Biot-Savart approach (equation 4.9).

$$B_z(x,y,z) = \frac{\mu_0 d}{4\pi} \int_0^{2\pi} \int_0^r J(r) \left[\frac{-r\sin\theta \cdot (y - r\sin\theta) - r\cos\theta \cdot (x - r\cos\theta)}{[(x - r\cos\theta)^2 + (y - r\sin\theta)^2 + z^2]^{3/2}}\right] \mathrm{d}\theta\, \mathrm{d}r \tag{4.9}$$

$$B_z^{exp} = \frac{1}{w^2} \int_{-\frac{w}{2}}^{\frac{w}{2}} \int_{x-\frac{w}{2}}^{x+\frac{w}{2}} B_z(x,y,z)\, \mathrm{d}x\, \mathrm{d}y \tag{4.10}$$

Furthermore, the sample/sensor separation and Hall probe active width (w = 0.8 μm) are taken into account when simulating the experimental signal (B_z^{exp})

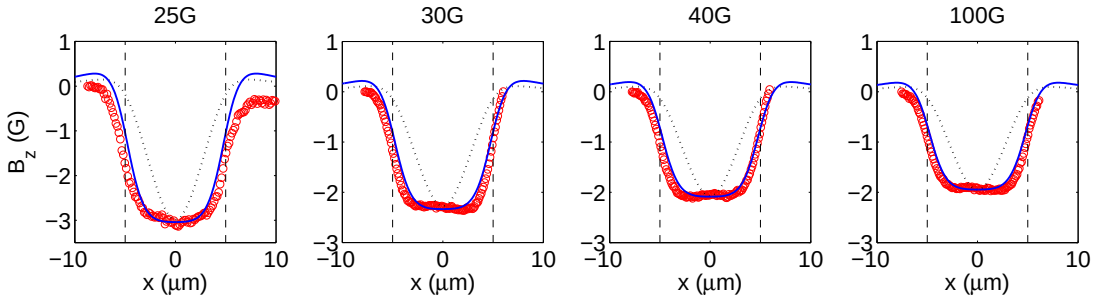

Figure 4-24: Experimental magnetic field profiles (circles) of mesoscopic Sr_2RuO_4 disks (D=10μm) captured in applied fields from 25 Oe to 100 Oe at T=260mK. Two theoretical fits have been attempted. A first, using a constant bulk critical current J_c from a standard model of the critical state in a thin disk (dotted lines), and a second calculated using only edge currents (solid lines) flowing within distance d/2 of the disk edge.

in equation 4.10. Figure 4-24 illustrates that the theoretical calculations of the disk field profile based solely on the presence of bulk currents provide a rather poor fit to the observed field profiles. Instead, good agreement with experiment is only achieved by considering supercurrent profiles based only on edge currents. The motivation for this form of current density profile comes from the description of the Geometrical Barrier where edge currents, potentially in excess of J_c, are described to flow within a region d/2 of the sample edge, where d is the sample thickness which in this instance we take to be 400nm. Field profiles generated from such supercurrent density profiles are seen to give much better agreement with the experimentally derived field profiles. However, the sample/sensor spacing required to give the best agreement ($z = 2.6\mu$m) is far larger than expected for our system, and unreasonable given the spatial resolution observed in previous images from the same sequence.

The theoretical fits based on edge and bulk currents are made with constant sample/sensor separation and so are solely parameterised by J_E and J_c. The strength of the screening of flux from the disk decreases with increasing field as demonstrated by the decreasing magnitudes of the profiles in figure 4-24. This trend is also captured by the greyscale values displayed in the caption of figure 4-23. Fits to disk profiles captured at different H_{eff} (where H_{eff} accounts for the Earth's and cryostat remnant fields) therefore require a variable $J_E(H_{eff})$. The total edge currents $I_E(H_{eff})$ for D=5 and 10μm disks are displayed below in

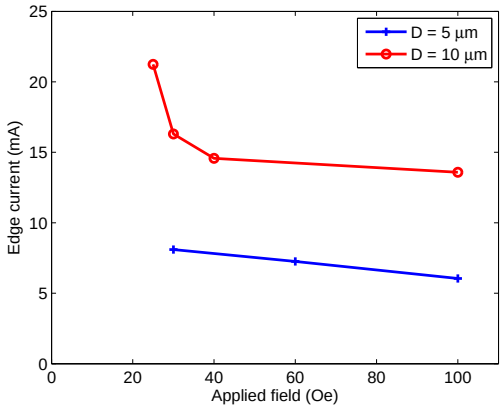

Figure 4-25: The edge currents predicted to be flowing in D= 5 and 10 μm disks at various applied fields. The corresponding critical current densities J_E are: In 5μm disks at fields 30, 60 and 100 Oe, J_E =33.5, 30 and 25 GAm^{-2} respectively. In 10μm disks at fields 25, 30, 40, and 100 Oe, J_E =43, 33, 29.5 and 27.5 GAm^{-2} respectively.

figure 4-25. The corresponding $J_E(H_{eff})$ are included in the caption.

4.5.2 Discussion

A previous attempt to pin chiral domain walls in Sr_2RuO_4 using micro-fabrication techniques reported a null result.[50] However, in this instance the 1μm wide, 1μm deep holes created with focussed ion-beam milling proved to be insufficient pinning centres for vortices, and so their effectiveness as sites of broken translational symmetry for pinning spontaneous chiral edge domain walls was questioned by the authors. In contrast the mesoscopic disks discussed here have been observed to have a definite impact on the vortex physics of the system. At low fields (fig. 4-18), vortices are screened from the disks by Meissner currents and take up locations at pinning sites on or near the disk edge. We see no evidence for spontaneous currents at the edge of the disks that could be attributed to a chiral order parameter. Furthermore, attempts to zero the magnetic field and provide optimum conditions for the formation of degenerate chiral domains failed to realise any domain wall-like magnetic structures in the sample. We conclude that if present, magnetic signatures from chiral edge currents, and chiral domain walls are below the RMS background noise threshold (0.014G is the RMS of the background noise in figure 4-19(c)) of this experiment, which corresponds to $\sim$50 and $\sim$170 times

smaller than the current theoretical predictions of the peak magnitude of CDWs and CEFs respectively, c.f., section 4.2.1.

It is well known that several energy barriers exist which can prevent the penetration of vortices until a penetration field H_P, where $H_P > H_{c1}$. The Geometrical Barrier (GB)[87, 88, 85] shows a $H_P \propto \sqrt{d/R}$ dependence on sample thickness to width ratio whereas the Bean bulk-pinning barrier has a linear relationship with sample size R.[89, 90] Each barrier becomes dominant in different temperature ranges allowing one to discriminate between the active barrier, as demonstrated in previous studies of similar mesoscopic structures in BSSCO-2212.[84, 91, 83] The data displayed in figure 4-21 for H_P in D=5, 10, 15 and 20 μm disks at 300mK, although limited, is in clear disagreement with the relationship of any known surface or geometrical barrier. However, caution must be exercised in interpreting this as unconventional behaviour as the theory of vortex entry energy barriers, and the previously mentioned experimental studies all involve a zero-field-cooled (ZFC) state, when the field is increased after cooling through T_c at H=0 when the sample enters a strongly metastable state. The FC protocol of this experiment produces vortex states close to equilibrium and so the validity of direct comparisons between the two are uncertain.

Also of interest is the surprisingly large increase in applied field required to nucleate a second vortex in the 10μm disk c.f. Fig. 4-20. For a diameter of 10μm, a field increase of $\sim$0.25 Oe is sufficient to nucleate an extra vortex within the disk ($\Delta B_{vtx} = \Phi_0/\pi R^2$). It is impossible to tell at *exactly* which field the second vortex penetrates, but consideration of the images in figure 4-20 suggests that once H_P has been reached, the observed field interval for the entry of a second vortex is somewhere in the range $0.25 < \Delta B < 0.8125$ Oe. At first sight the lower limit of this range appears consistent with expectations but this situation is only possible if we assume that the 1stvortex penetrates precisely at 1.25 Oe (d), and the second vortex penetrates immediately after (e), at just over 1.5 Oe. Although perfectly possible, that scenario would then leave a field increase of 0.375 Oe (e)$\rightarrow$(f) with no sign of a third vortex. One possible explanation for the irregular penetration of vortices into the disk could be the presence of a low density of strong pinning sites in the sample. If the pinning potential of these sites were roughly comparable, thermal fluctuations may result in a variation of the number of occupied pinning sites on each cool-down cycle. It certainly seems

that for H_{eff} >1.25 Oe several vortices are being trapped in the interstitial region rather than continuing to penetrate the disk as expected.

The formation of a vortex ring that clearly reflects the disk symmetry, at the centre of the D=20μm disk, provides direct evidence of the influence of the sample boundaries on the vortex configuration. Previous images have provided evidence of a low density of strong pinning sites in this sample. c.f., the previous paragraph and section 4.4.2. In this instance the formation of the vortex ring is probably facilitated by the increased measurement temperature (1K) which reduces the pinning potential for two reasons. Firstly, the associated increase in vortex size ($\lambda(T)$) means that small crystal defects become "invisible" to vortices, and secondly vortices are more likely to be excited off pinning sites by their increased thermal energy. This increased freedom allows the intrinsic vortex interactions with Meissner screening currents flowing at the disk edge, and each other, to define the vortex configuration. The formation of such a vortex ring is consistent with the theory of "large" mesoscopic disks,[92] which established a *maximum of five* rule for inner rings of "particles" in mesoscopic systems.[93, 94]

Figure 4-23 contains a sequence of images that capture the field distribution in a 10μm disk up to 100 Oe. As the field is increased more and more vortices penetrate the disk and single vortex resolution is lost. Previous studies of similar disks in BSCCO-2212 have captured evidence of a vortex 'dome' forming at the centre of the disk, consistent with the theory of the Geometrical Barrier.[93] In Sr_2RuO_4 at 300mK, in applied fields up to 20 Oe we do not observe a smooth dome but instead a rather inhomogeneous vortex distribution is captured, which is again perhaps indicative of a rather low density of pinning sites with a quite deep pinning potential. Indeed considering that a field increase of ∼0.25 Oe is sufficient to introduce a single vortex into the disk area, one would expect the image to be full of vortices and showing a homogeneous signal at 20 Oe. Tellingly, the grayscale at 20 Oe of 4.08 G is 6 times greater than that for a single isolated vortex (∼0.65 G c.f. fig. 4-18). Such a signal suggests that the dark regions correspond to a flux of 20-4.08≈16 G which has an associated square lattice spacing of ≈1μm. The white regions must therefore contain vortices very much closer together than this confirming that the vortex distribution is strongly influenced by underlying forces, presumably related to crystallographic defects.

It is therefore surprising that the vortex distribution becomes abruptly and

emphatically homogeneous at H_{eff} $\geq$25 Oe. It is as if the pinning forces are suddenly "turned off" at this field strength. Up to the maximum applied field of this experiment, 100 Oe, flux is presumably entering the whole sample but the majority of vortices preferentially penetrate the disk rather than the interstitial area, a process captured by the steadily decreasing gray scale (caption 4-23) of the screened disk signal. If flux was penetrating solely into the disk we would surely expect the screening signal to diminish far more rapidly and disappear at far lower fields. Line scans of the disks at H_{eff} $\geq$25 Oe display a steep-sided and flat-bottomed magnetic profile of the disks (figure 4-24). Critical state theory of thin disks[86] predicts that at these applied fields the disks are saturated with the critical current density J_c but an evaluation of the resultant field using a Biot-Savart (c.f. section 4.5.1) approach yields a v-shaped profile that correlates poorly with experiment, c.f., dotted lines in figure 4-24. In fact good agreement is reached when only edge currents (J_E) are considered in the supercurrent profile. The motivation for such edge currents, set to flow within a distance d/2 of the sample edge in this instance, was provided by the theory of the geometrical barrier developed by Zeldov,[85] and was found to provide good agreement with experiment, c.f., solid lines in figure 4-24, albeit with an unreasonably large scan height ($z = 2.6\mu$m). It should be noted that presently the edge currents are added in a rather ad-hoc way, and strictly speaking a self-consistent solution is appropriate. It is expected that this approach can still be informative of the underlying physics. Earlier in this discussion, it was suggested that the lack of agreement found between H_P(R) and theories of energy barriers was because the theory involved ZFC and metastable states, whereas the experiment involved FC states close to equilibrium. However, the high fields presently discussed here represent saturated critical states, when J_c is flowing everywhere throughout the disk, and as such are at (or very close to) equilibrium and we therefore expect much better agreement with our FC mesurements.

The edge currents used in the disk profile fitting shown in figure 4-24 are J_E $\sim 10^{10}$ Am^{-2} which compares favourably with theoretical predictions of the GB: $J_E^{GB} = 2H_{c1}/d \sim 10^{10} Am^{-2}$[85] ($H_{c1}\approx$70 Oe.[95]) suggesting that the attempted comparisons with the GB made here are perhaps reasonable. As discussed previously, the screening signature of the disk weakens with increasing field. This is captured by the gray-scale of the SHPM images and also by the fit-

ting parameter J_E used in the simulation. Figure 4-25 displays the *total* current flowing at the edge of the D=5 and 10 μm disks at various applied fields. The edge current flowing in the 5μm disk is $\sim$1/2 that in the 10 μm disk suggesting that field-from-a-loop approximations of the screening field $B_E = \mu_0 I/2R$ are equivalent. Between the applied fields of 30$\rightarrow$100 Oe the disks have B_E in the range of 101$\rightarrow$85G (D=10μm) and 101$\rightarrow$75 G (D=5μm). Surprisingly, the theory of the GB does not include a sample size dependent critical current and so it seems the system is governed by something more complex than a conventional GB.

A surprising consequence of the theoretical fitting is that they suggest we are in the limit $J_E \gg J_c = 0$, corresponding to the *weak pinning* regime. This is seemingly in direct contradiction with the indications of strong pinning observed below 25 Oe in this experiment, and in previous measurements of Sr_2RuO_4 discussed earlier. c.f. Section 4.4.2. However, we again reiterate that we are comparing field-cooled experiment with zero-field-cooled theory, the repercussions of which are currently unclear.

4.5.3 Conclusion

Large mesoscopic disks have been fabricated on the a-b surface of a high quality Sr_2RuO_4 single crystal in order to act as locations where translational symmetry is broken, and hence providing ideal sources for spontaneous chiral edge currents/fields predicted to arise as a consequence of chiral spin-triplet superconductivity. Scanning Hall probe images reveal that we see no spontaneous magnetic signal at the disk edges and conclude that either they do not exist, or if the signal is present but below our measurement threshold, the peak magnitude is $\sim$170 times smaller than predicted by current theory for the $d = \Delta_0(k_x \pm ik_y)\hat{z}$ chiral order parameter. Neither do we observe any magnetic signal anywhere else in the sample that could be attributed to the signature of a chiral domain wall suggesting that if present, the peak signal from such a feature is $\sim$50 times smaller than predicted by current theories.

The disks display strong partial screening of magnetic flux, and theoretical fits to magnetic field profiles of the disks suggest a Geometrical Barrier-like energy barrier is governing flux penetration into the disks. However several contradic-

tions to this hypotheses emerge: Firstly, the edge currents are a strong function of disk size, something which isn't captured by the GB; Secondly, simulations suggest that the system is in the *weak pinning* limit in direct contradiction with several pieces of evidence that suggest the presence of a low density of rather *strong pinning* sites in the sample; Thirdly, the penetration field (H_p), as defined by the lowest field when we observe the first vortex in the disk, is not proportional to $(d/R)^{1/2}$ as predicted for the GB.

The source of these apparent contradictions may lie in the fact that GB is evaluated within a ZFC theory and so comparisons with the FC measurements of this experiment are difficult, and reservations about their validity must be made. Indeed, theoretical treatments of FC flux distributions are somewhat qualitative and to the best of the authors knowledge there is no discussion of how edge currents might be effected by this in the literature. It is hoped that the work undertaken here may stimulate new theoretical work leading to increased understanding of flux penetration in mesoscopic samples.

Chapter 5

Broken symmetry vortex structures in a superconducting MgB_2 thin film

5.1 Introduction

The existence of two-band superconductivity was proposed soon after the BCS theory was published,[96] but remained of purely theoretical interest until the discovery of MgB_2 in 2001.[97] Initial excitement centred on the fact that it is a simple inter-metallic compound which consists of relatively cheap and readily available elements. Additionally, the 'high' (non-cuprate) T_c ($\approx 38K$) flew in the face of conventional wisdom; that a high BCS T_c required a high charge carrier density and electrons that reside in open d-shell orbitals.[98] Important issues of the BCS pairing symmetry and the existence and nature of the two energy gaps were resolved relatively quickly, but several significant questions remain.[99]

One subject of interest is the behaviour of superconducting vortices. Much of the recent focus on vortex matter in MgB_2 has been on the apparent presence of an attractive component to the vortex-vortex interaction at long range that gives rise to the "clustering", "chaining", "striping" and "gossamer-like" patterns seen in Bitter decoration,[100], scanning SQUID,[101, 102] and scanning Hall probe experiments.[103] Such patterns are well known to be possible in systems with competing repulsive and attractive interactions.[104]

A non-monotonic vortex interaction was predicted theoretically in MgB_2,[105] before the first experimental observation,[100] as a consequence of disparate "coherence lengths", μ_1^{-1}, μ_2^{-1}, (sometimes termed "inverse field masses" to avoid ambiguity) emerging from, but not directly attributable to, the distinct superconducting gaps Δ_π and Δ_σ in different bands. The view that this represented a new state, termed Type 1.5,[100] was immediately challenged as unphysical in a system with a single critical temperature T_c, and two distinct length scales were deemed unsupportable within Ginzburg-Landau (GL) formulism.[106] Experimental data however, support the existence of two distinct coherence lengths,[107, 108, 109] and so the apparent discrepancy provoked rapid theoretical development in the field. This included further investigation of Type 1.5 theory,[110] and the development of an *extended* GL formulism that justified the use of the disparate length scales known as *healing lengths* in the analysis of two band superconductivity.[111, 112] While it is stressed that the healing lengths are distinct from formally defined coherence lengths, it was subsequently shown that the regime of large disparity between them corresponds to the region of non-monotonic vortex interaction in the standard GL formulism.[113]

Additionally, it has been pointed out that numerous other mechanisms of vortex attraction exist, with a diverse range of origins including: BCS corrections to GL theory for $0.71 \leq \kappa \leq 1.5$; tilted applied fields; a type of "Casimir" force in layered materials; a closely related thermally activated van der Waals (vdW) type interaction and an impurity activated vdW-type interaction.[114] Finally it has also been noted that it is possible to get stripe-like phases solely from two *repulsive* interactions, provided there are at least two lengthscales present in the system.[115, 116, 117]

Stable vortex configurations resulting from a short-range repulsive and long-range attractive vortex interaction have been studied recently using molecular dynamics and shown to produce vortex "islands" and "labyrinths",[118] whose nearest neighbour distributions bear similarities to those seen experimentally.[100] This work was extended to include an analysis of short-range repulsive, *intermediate-range* attractive and long-range repulsive interactions that produced a field-driven evolution of the vortex pattern from clusters→ stripes→ labyrinths→ triangular ordering.[119, 120] It is suggested in Ref. 11 that the addition of a long-range repulsion is crucial in order to stabilise the striping patterns observed exper-

imentally, both in MgB_2 and previously in low-κ Type II superconductors.[114]

To date, vortex imaging in MgB_2 has been limited to single crystals. The thin film measured here has a much shorter electronic mean free path ($\ell \approx 11nm$) than the single crystals measured previously, and as such must exhibit much higher rates of inter- and intra-band scattering. This has repercussions for all of the candidate "attraction" mechanisms. It is against this background of interesting vortex patterns in MgB_2, uncertainty in the origins of the inter-vortex interaction, and the opportunity to probe a unique sample (different dimensions, different growth technique, contrasting low ℓ), that the series of measurements presented here were undertaken.

5.2 Experimental method

High resolution scanning Hall probe microscopy (SHPM) has been used to perform local magnetic imaging of an epitaxial 160nm thick MgB_2 thin film. The film was grown by molecular-beam epitaxy on a Silicon (111) substrate held at $\approx 300^oC$ at a growth rate of $2.3\dot{A}/s$ and a typical flux ratio (Mg:B) of 1.8.[121] A $50\dot{A}$ MgO seed layer was evaporated onto clean Si(111) to promote lattice matching. A lattice strain as low as 3% is achievable through careful consideration of substrate orientation[121], and any strain associated with a lattice mismatch resides in the immediate vicinity of the seed layer and is expected to have a proportionally negligble effect in a thin-film of this thickness.[122] Figure 5-1 displays x-ray diffraction (XRD) data for our sample which establishes that the thin film is highly textured. The diffraction peak markers (vertical lines) represent powder diffraction patterns of polycrystalline MgB_2 samples, with the line height representing the relative diffraction intensity, from standard XRD reference tables. The large height of the peaks for the (002) and (001) planes, despite these having a relative powder pattern intensity of <10%, indicates a strong texture in the expected growth orientation on Si(111). This conclusion is further supported by the absence of the MgB_2 (101) peak which has the maximum powder weighting. Finally, the small signal recorded at $\approx 58.5^o$ is a forbidden reflection from the Si(222) planes, picked up because of the type of 2D detector used.

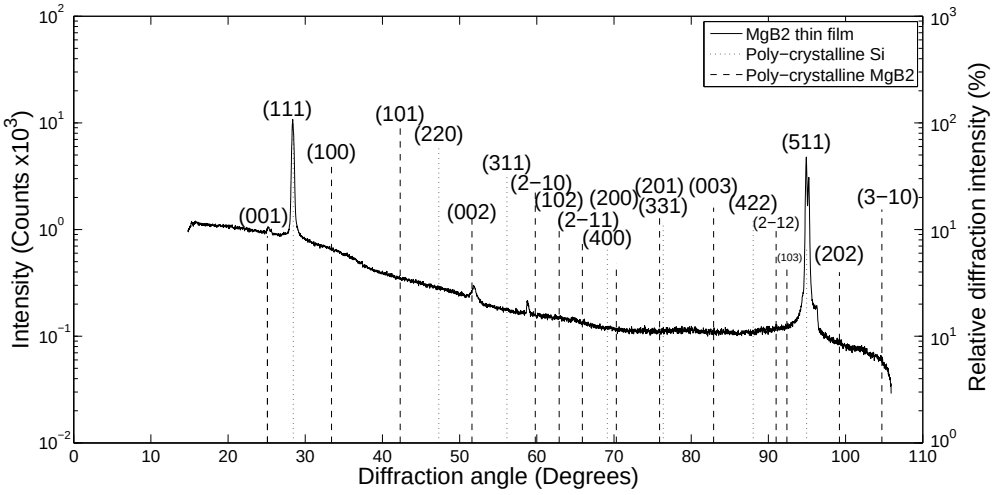

Figure 5-1: X-ray diffraction data of a 160nm MgB_2 thin film, grown by molecular-beam epitaxy and investigated in this series of scanning Hall probe measurements. Vertical lines represent powder diffraction lines of polycrystalline samples, with line heights representing relative diffraction intensity (%) from standard XRD tables.

The resistance versus temperature data displayed in figure 5-2 show an extremely sharp superconducting transition ($\Delta T \cong 0.1K$) at $T_c \cong 35.85K$. The residual resistance ratio, $RRR = R(300K)/R(40K)$, provides a rough indication of the electronic mean free path ℓ (larger RRR = longer ℓ) and can give a useful insight into the crystallinity of the sample. The RRR for our thin film is 1.25, which is considerably smaller than estimates for single crystals which vary between 3.5 and 25.[123, 124, 125, 126, 127] It is also below various other thin film estimates of 2.5,[128] and 4.0-33.3.[129] We therefore expect that the thin film investigated here has a higher level of disorder than comparable samples in the literature. Estimation of the electronic mean free path (ℓ) is possible from the Drude relation $\ell = 3/\rho_0 N(0)\nu_F e^2$. Using an average Fermi velocity of $\nu_F = 4.8 \times 10^5 ms^{-1}$,[130, 131] and a density of states $N(0) = 0.7$ eV^{-1} unit cell^{-1}[132, 133] with a residual resisitvity $\rho_0 = \rho(36K) = 15\mu\Omega cm$ (c.f. Fig. 5-2) we estimate $\ell \approx 11nm$ in our sample. This is far shorter than estimates from other samples which lie in the range $38 \leq \ell \leq 100nm$.[134, 123, 135, 136, 137, 138]

Identification of vortex locations in SHPM images was straight forward at the three lowest fields when vortices are well separated, but reasonably difficult in

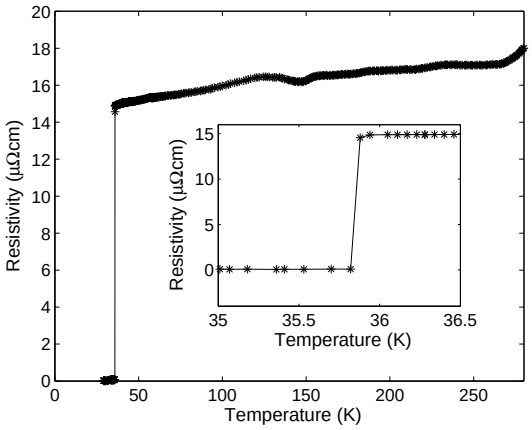

Figure 5-2: Resistivity versus temperature curve for the 160nm MgB_2 thin film, grown by molecular-beam epitaxy, and investigated in this series of scanning Hall probe measurements. The superconducting transition occurs at $T_c \cong 35.85K$ with $\Delta T \cong 0.1K$

some regions of the 5G image. To confirm that the correct number of vortices had been identified at 5G, a self-consistency check was made based on the known value of applied field and scanned sample area.

5.3 Results

Figure 5-3 displays the vortex distributions captured after field cooling from $T > T_c$ to $T \approx 1.7K$, at four different magnetic inductions (1.25, 1.7, 2.8 and 5G), after applying a field perpendicular to the thin film (// c-axis). Each image is a compilation of between 16 and 25 individual scans, aligned and superposed, allowing assessment of the degree of structural disorder in the vortex lattice over an area of $\approx 50 \times 50 \mu m^2$. An initial visual inspection reveals possible weak ordering of vortices into chains at the three lowest fields with a predominant "stripe" direction, and a labyrinth-like structure at the highest field. The type of order at lower fields could be described as "chaining", which can be misleading, given that the Abrikosov lattice also contains "chains" of vortices. For clarity, when we refer to chains what we really mean is 'a chain formation with lower symmetry than the Abrikosov lattice'. The degree of chaining and the predominant direction are discussed later in connection with figure 5-5, but first we analyse the

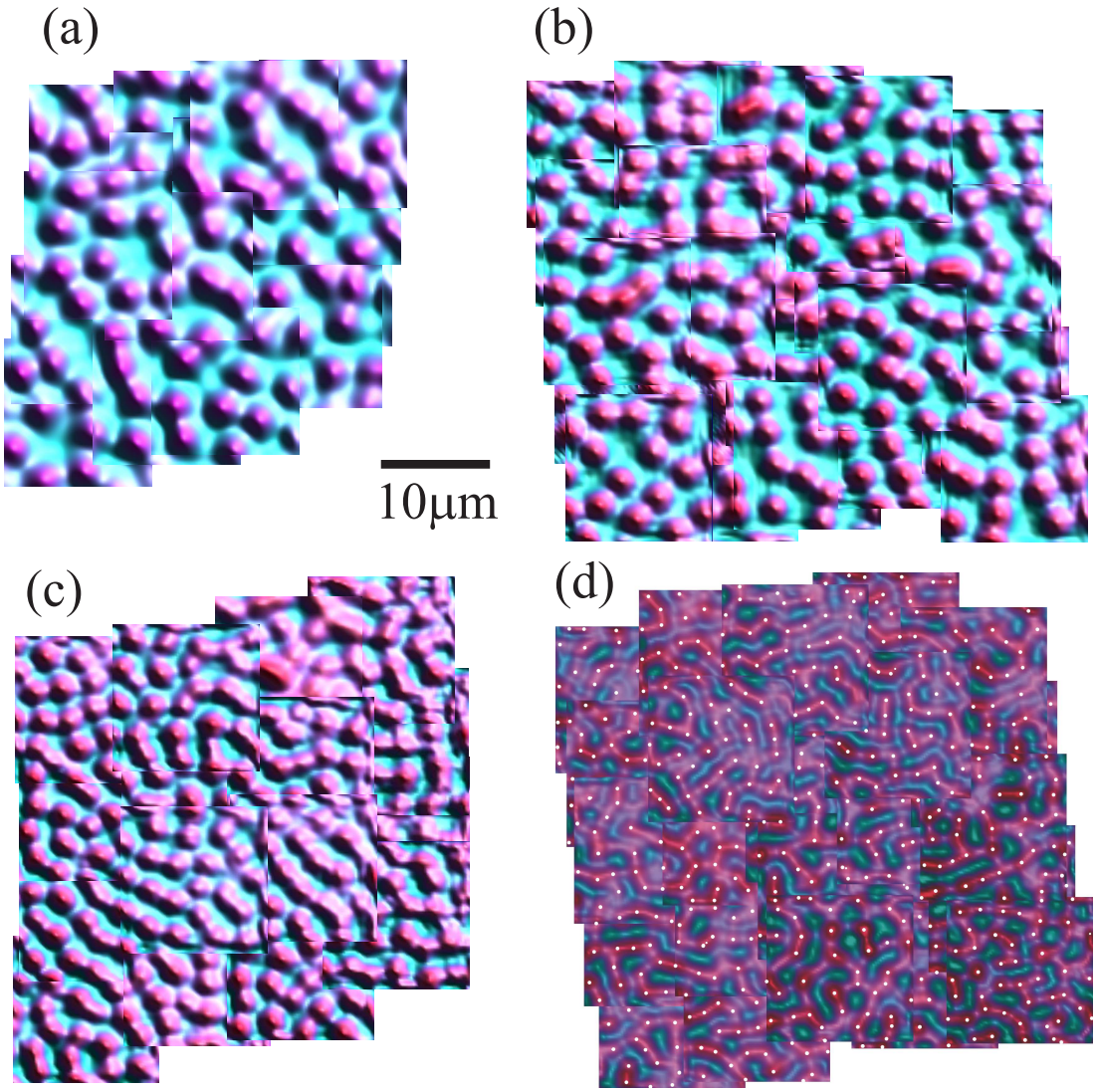

Figure 5-3: Composites of multiple overlapping scanning Hall probe images ($\approx 50 \times 50 \mu m^2$) of a superconducting MgB_2 thin film (thickness 160nm) captured at T≈1.6K after field cooling in perpendicular fields $H_\perp$ (a) 1.25G, (b) 1.7 G, (c) 2.8 G and (d) 5G. Vortex locations in (d) are highlighted with white dots.

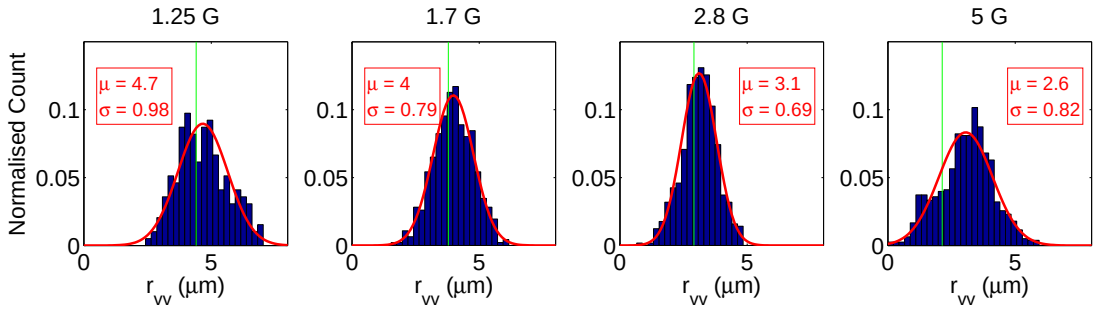

Figure 5-4: Normalised histograms of the vortex nearest neighbour distributions (based on a Delaunay triangulation) of the four images shown in figure 5-3. Gaussian fits (red line) based on the distribution parameters $[\mu, \sigma](\mu m) = [(4.7, 0.98)_{1.25G}, (4, 0.79)_{1.7G}, (3.1, 0.69)_{2.8G}, (2.6, 0.82)_{5G}]$ and scaled by the bin width $(0.22\mu m)$ are superimposed, as is the equivalent spacing of ideal triangular ordering (green line). The distribution evolves from weakly spilt bi-modal at 1.25G to more or less gaussian at 1.7G. A slight imbalance of statistical weighting towards short-bonds at 2.8G evolves into a pronounced shoulder at 5G.

nearest neighbour distribution, which is a useful statistical technique for detecting vortex clustering and characterising the inter-vortex interaction. Figure 5-4 presents normalised histograms of the vortex-vortex separation based on a Delaunay triangulation. According to the Ginzburg-Landau theory for an ideal Type II superconductor, we would expect the vortices to form a triangular Abrikosov lattice. With this in mind the lattice constant of an ideal triangular arrangement, $a_{tri} = \left(\sqrt{3}\Phi_0/2B\right)^{\frac{1}{2}}$, at each respective field (B) is also plotted for comparison.

At the lowest field (1.25G) we see a weakly split bi-modal distribution, spread around $a_{tri}^{1.25G}$. The two peaks reflect the average intra- and inter-chain bond lengths. With increasing field the distribution becomes more gaussian but retains a pronounced asymmetry, with a slightly heavier short-bond statistical weighting at 2.8 G that evolves into a more distinct shoulder at the highest field strength.

Self-correlation images (SCs) and fast Fourier transforms (FFTs) are excellent ways of extracting weak underlying ordering from images. SC images (G) are generated according to the function $G(x', y') = \sum_{x',y'} f(x, y) f(x + x', y + y')$ where $f(x, y)$ is the original 2D image and x' and y' are shifts in x and y. The resulting image peaks at the centre (where $x' = y' = 0$) and at any underlying periodicity in the original image. In the ideal Type II case, vortices form a triangular lattice and a subsequent SC plot will replicate this perfectly. However in the case of a

disordered triangular lattice, as the correlations over the whole image will not be so strong, we expect the SC to be dominated by 6 bright spots that trace a hexagon around the central peak. In addition to this, FFTs provide a second independent ordering analysis by picking out any dominant periodicities in the frequency spectrum.

Self-correlation images (a) and FFTs (b) are shown for the four magnetic fields (i-iv) of figure 5-5. First we consider the SC images (a). At the lowest field (a-i), four of the expected six central bright spots are missing, signifying a strong breaking of symmetry in the vortex lattice. In (a-ii) we now have a heavily distorted arrangement of six spots, causing a slight weakness of the signal on the top-left to bottom-right diagonal, as highlighted by the arrows. These locations are where we would normally expect to see two bright spots in the case of ideal triangular ordering. This weakening on or near the diagonal is again present and more pronounced at 2.8 G (a-iii) where only 4 of the expected 6 spots are present. These images (a-ii and a-iii) signify weak chaining in this direction. The drop in signal in the chaining direction (weak spots) arises because there is very weak correlation of vortex positions along the chains, but as the SC shifts perpendicularly to the chaining direction it picks out the inter-chain periodicity, illustrated by the two solid bright spots either side of the central spot in (a-iii). Finally at the highest field (a-iv), we can still make out four diffuse spots with two missing, but now the contrast is much weaker, signifying that the strength of the preferential ordering direction is also weaker at this field.

Now we address the FFTs in figure 5-5 (b). (b-i) shows two clear bright spots reflecting the strongly broken symmetry reported by the SC image (a-i). At intermediate fields we do not see strong bright spots but we do see a weakly broken symmetry, with a weakening of the signal on the top-left to bottom-right diagonal. This weakening again lies on the presumed chaining direction and is present due to a lack of correlation along the vortex stripes. Interestingly, the predominant direction of this chaining direction varies by $\approx 45^o$ between fields, seemingly ruling out obvious material-based origins of the broken symmetry such as planar defects in the crystal structure. Lastly we examine the 5G data 5-5(iv) and note that while still present, the symmetry breaking of the vortex lattice at this field is by far the weakest of the four inductions investigated. We still only see 4 out of 6 spots in the SC image but the weakness of the signal on the off

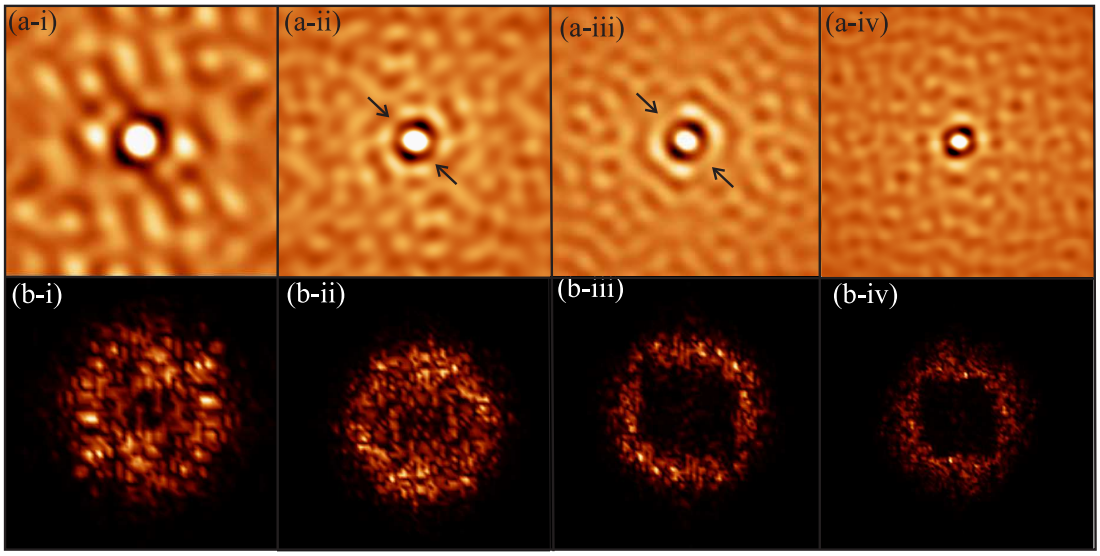

Figure 5-5: Self-correlation (SC) plots (a(i)-a(iv)) and Fast Fourier Transforms (FFT's) (b(i)-b(iv)) of the four vortex distributions shown in figure 5-3 at local magnetic inductions of (i-iv): 1.25, 1.7, 2.8 and 5G. Both analyses provide separate confirmation of a general predominant chaining direction at the 3 lowest fields (i-iii) from roughly top-left to bottom-right (see text).

diagonal is less pronounced, and the FFT barely picks out any broken symmetry at all. All of the data analysis presented here has been performed with WsXM freeware produced by Nanotec Electronica.[139]

5.4 Discussion

Material defects are well established as possible origins of broken symmetry of the vortex lattice in superconductors.[140] It is therefore prudent to confirm that they are not likely the cause of the vortex structures observed here, and fortunately this arrives in several pieces of evidence. Firstly, it is reassuring that the predominant direction of vortex chaining is seen to vary by $\approx 45^o$ between cooling cycles at different fields, and disappears entirely at the highest applied field. If the structures reflected the underlying pinning potential, one might expect to observe the same chaining direction at all fields. Secondly, it should be stressed that the predominant directions that emerge from the symmetry analysis (Fig. 5-5) are an average over the whole image, and that visual inspection of the vortex patterns reveals variation of chain direction within the image, including several

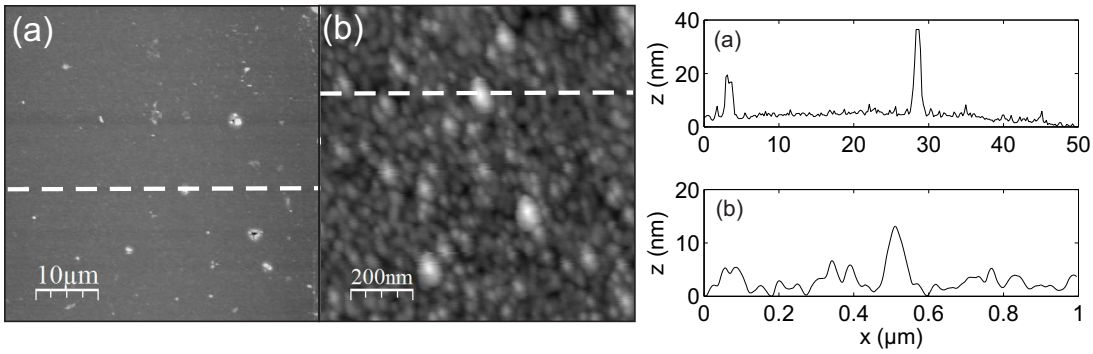

Figure 5-6: AFM images of the 160nm MgB_2 thin film. There is no detectable topographic structure in the thin film over a region comparable in size to the vortex images shown earlier (a). The grain size is of the order of ∼10-75nm (b).

instances of curved chains. Such phenomena seem unlikely to arise from crystallographic defects which presumably would have a linear appearance. Thirdly, studies of critical currents in MgB_2 thin films suggests that grain boundaries are the dominant pinning sites in this system.[141] Atomic force microscope studies of these epitaxially grown films show a grain size of the order of ≈10-75nm (c.f., figure 5-6 (b)), which is much too fine to link to the vortex patterns observed here. Apart from several small pieces of dirt (∼40nm tall), there is no detectable topographic structure to the film over $50\times50\mu m^2$, an area comparable to the composite scan images of vortex configurations shown earlier.

Finally, perhaps the most compelling evidence comes in the form of the images of repeated FC cycles presented in figure 5-7. If pinning centres dominated the observed vortex configurations, one would expect repeated FC measurements to reveal identical images. At 2.5G, figures 5-7(a) and (b), the majority of vortex locations, although generally within about a vortex diameter of each other, are slightly different, as best evidenced by the difference image (c). Here, the four or five vortex size regions of strong contrast correspond to entirely new vortex locations, the weaker signals represent areas where vortices are close to previous positions but slightly misaligned, and the blank regions are where vortices were found in identical locations. Interestingly, even with so many differences, the patterns are qualitatively similar, which suggests that the three or four pinning sites present in the imaged region are enough to pin chains, but once in chains, vortices are clearly free to take up any position they like. At 5G the dense

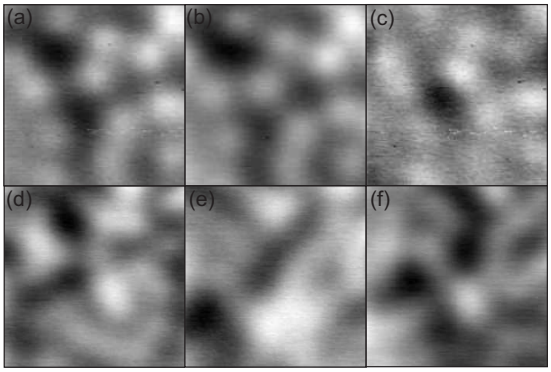

Figure 5-7: A sequence of repeated field-cooled cycles in applied fields of 2.5G, (a) and (b), [(c) is a subtraction of (a)-(b)] and 5G, (d), (e) and (f). The images were acquired after cooling to 20K. The greyscales of (a), (b) and (c) are 0.35, 0.29 and 0.21G. Images are $\approx 8 \times 8 \mu m^2$.

labyrinth structure is completely different after each FC cycle. Clearly the pinning centre density is too low to influence the vortex configuration at such high fields.

Many experiments have observed low-field vortex patterns that indicate the presence of an attractive component to the vortex interaction in MgB_2.[100, 101, 102, 103] We too observe such patterns, as evidenced by the weak peak-splitting of the vortex nearest neighbour distribution at 1.25G and 5G (Fig. 5-4) and broken six-fold symmetry at all fields (Fig. 5-5). The immediate presumption is that the split peaks represent intra-chain and inter-chain bond lengths, and this is confirmed by the analysis presented in figure 5-8 (a) and (b). Here the Delaunay triangulation mesh used to generate the statistics is partially reconstructed in typical individual scan images at two different fields. In figure 5-8 (a) the available bond lengths are fixed at $4\mu m$ (yellow) and $5\mu m$ (black) representing the two peaks in the 1.25G distribution, and attempts were made to fit a nominal number of bonds to the vortex pattern by eye. An excellent fit is achievable and the origin of the short bond length (intra-chain) and long bond length (inter-chain) is clearly visible with a definite predominant chaining (short bond) direction.

The vortex separation becomes roughly gaussian at intermediate fields, with recorded mean spacings of $4\mu m$ at 1.7 G and $3.1\mu m$ at 2.8 G that are very close to what we would expect for ideal triangular ordering at these fields: $a_{tri}(1.7G) = 3.8\mu m$ and $a_{tri}(2.8G) = 2.9\mu m$. A shoulder at short bond lengths emerges at 2.8 G and grows to a pronounced bi-modal distribution at 5G. Again the origin of

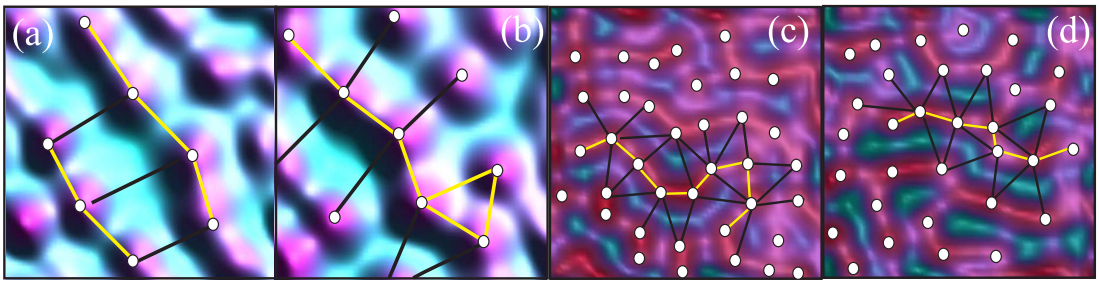

Figure 5-8: Partial reconstructions of the Delaunay triangulation of vortex positions with a nominal number of bonds for typical individual scan images at: 1.25G [(a),(b)] and 5G [(c),(d)]. The bond lengths have been fixed to take one of two possible values, taken from the bi-modal peaks seen in figure 5-4 (1.25G and 5G). At 1.25G these peaks correspond to $4\mu m$ and $5\mu m$ (yellow and black bonds respectively). At 5G the short bond (yellow) is $1.6\mu m$ and the long bond is $2.75\mu m$. This visualisation confirms that the peak-splitting observed in the bond length distributions (Fig. 5-4) originates from the ordering of vortices into chains, and that the short and long bonds correspond to intra- and inter-chain bond lengths.

the two spacings at 5G is visualised in figure 5-8 [(c) and (d)] where the short and long bond lengths have been fitted (by eye) to single images of vortices, confirming their identity as short- and long-bond spacings that characterise the labyrinth structure. The 5G bi-modal distribution is heavily skewed, with significantly heavier statistical weighting at the longer, inter-chain bond length. The explanation for this is evident from further consideration of the reconstructions in figure 5-8. Every vortex in a chain will only have 2 short bond neighbours, one 'up' chain and one 'down' chain. However, the Delaunay triangulation picks an average of 6 or 7 nearest neighbours which leaves 4 or 5 longer bonds drawn out to neighbouring chains.

The statistical imbalance between the inter- and intra-chain bonds is also marked at 2.8 G. Here the vortex density is too low to populate fully formed chains resulting in numerous instances of pairing into vortex "molecules". Each molecule contributes a single short bond but several (>10) long bonds to neighbouring molecules, resulting in the marked statistical imbalance seen in figure 5-4 (2.8 G).

Having discussed the vortex distribution of each image individually, we now address the change of the vortex structure from chaining with a preferential di-

rection ("stripes"), to a labyrinth.

A rich variety of patterns exist in systems with competing attractive and repulsive interactions.[104] A short-range vortex repulsion and long-range attraction leads to a natural vortex spacing d_{min} where the potential is a minimum and this phenomenon has been used to explain unusual vortex patterns (Type II clusters surrounded by Type I voids) in low-κ Type II materials in the Type-II\1 regime.[142, 114]

Recent studies of vortex configurations in the presence of non-monotonic interactions predict interesting patterns that bear a qualitative resemblance to those observed in our experiment. Molecular dynamics simulations predict a vortex-density-driven evolution from "clumps" to "labyrinths" before entering a final increasingly dense triangular phase.[118] Interestingly, the above molecular dynamics simulations unanimously predict vortex clumps are the ground state of systems with short-range repulsive (SRR) and long-range attractive (LRA) interactions. Clumps, labyrinths and voids are all shown to be possible in such systems but striping patterns, such as those seen in the low-κ Type-II\1 materials,[114] recently in single crystal MgB_2,[103] and now here, are found to be stabilised *only* when a long-range repulsion is considered in tandem with a short-range repulsion and *intermediate-range* attraction (IRA).[119, 120, 143, 144] Here, interestingly, vortices are seen to form labyrinthine-like domain structures which bear a strong resemblance to the features of figure 5-3(d). The authors also suggest that a longer range repulsion needs to be considered when understanding the patterns in Type-II\1 superconductors.[142, 114] Finally, for completeness, it should also be noted that stripe formation is possible in systems with strictly repulsive interactions, provided that more than one length scale is present in the interaction.[115, 116, 117]

Analysis of such patterns in Type-II\1 superconductors,[142] and MgB_2,[103] yields an approximately field-independent intra-chain or intra-cluster spacing, r_0, which is postulated to correspond to the minimum in the vortex-vortex interaction potential, d_{min}. The data shown for our MgB_2 film in Fig. 5-4 appear to show a field-dependent average intra-chain vortex spacing ranging from $4\mu m$ at B =1.25G in the 'stripe' regime to $1.6\mu m$ at B=5G in the 'labyrinth' regime. We speculate that the vortex-vortex interaction potential in our samples has a very broad and shallow minimum, which might well give rise to the

field-dependent intra-chain spacing that we observe. This behaviour is in qualitative agreement with molecular dynamics simulations for a SRR/IRA/LRR inter-vortex potential.[119] Moreover, in these simulations the number of chains contained within a stripe is shown to be dependent on the screening length of the inter-vortex potential. Stripes of vortices consisting of between 2 and 5 chains wide could be realised this way placing this work close to the regime of one-chain stripes observed here.

Now we return to considerations of the vortex configuration at the intermediate field 1.7 G. Here we have a seemingly inconsistent picture of a gaussian distribution to the vortex bond lengths (Fig. 5-4, 1.7G) which contains a very weak broken symmetry (Fig. 5-5(ii)). This is inconsistent because at the low and high fields we argue that the broken symmetry and bi-modal distributions are inextricably linked. If we increase the applied field from zero there must exist a value at which r_0 matches the equilibrium Abrikosov lattice spacing, even if r_0 is field-dependent as discussed above. We tentatively suggest that in our system, this point lies very close to 1.7 G as evidenced by the gaussian distribution of nearest neighbour bond lengths at this field strength. However, there remains enough disparity to result in weak chain formation. Certainly it is noteworthy that at this vortex density the broken symmetry of the vortex lattice is much weaker than at the neighbouring field strengths (Fig. 5-5).

Current focus of the scientific debate on MgB_2 is centred on the origin of the attractive component of the vortex interaction. A recent review of the field points out that vortex patterns similar to those observed in MgB_2 were first imaged in Type II superconductors with $\kappa \approx 1/\sqrt{2}$ many years ago.[145] Termed the *Intermediate-mixed state*, it was deemed to arise due to the appearance of a vortex attraction predicted by the S-shape in the theoretical magnetization curve and formally resulting from BCS corrections to the GL theory. This and five other conceivable origins of vortex attraction in MgB_2 are put forward in a recent review by Brandt and Das.[114]

Elsewhere, recent phenomenological studies of two-band superconductivity in MgB_2, using two-component GL theory with distinct GL parameters κ_π and κ_σ for the respective bands, suggest that a SRR and LRA interaction arise due to the fact that the π and σ components of the order parameter lie in different regimes: $\kappa_\pi < 1/\sqrt{2}$ (Type I) and $\kappa_\sigma > 1/\sqrt{2}$ (Type II).[100] The view that this

represented a new state was immediately challenged as unphysical in a system with a single critical temperature T_c, and two distinct length scales were deemed unsupportable by Ginzburg-Landau (GL) formulism.[106] The apparent discrepancy with experimental data in support of the existence of two distinct coherence lengths provoked rapid theoretical development in the field.[107, 108, 109] This included the further development of Type 1.5 theory which introduces the length scales, μ_1^{-1}, μ_2^{-1}, and investigations of the closely related *extended* GL formulism (EGL) that justified the use of the disparate length scales ξ_1 and ξ_2, known as *healing lengths*, in the analysis of two band superconductivity.[111, 112] While it is stressed that the healing lengths are distinct from formally defined coherence lengths, it was subsequently shown that the regime of large disparity between ξ_1 and ξ_2 corresponds to the region of non-monotonic vortex interaction in the standard GL formulism.[113] Furthermore, recent simulations of multi-component time-dependent *standard* GL equations also demonstrate an attractive vortex interaction. Similar to Type 1.5 theory, this attraction is predicted to arise when the London penetration depth falls between two distinct "coherence lengths" (again associated with the distinct π and σ bands), but here the divergence of the coherence lengths requires the use of special forms of the GL functional.[146]

The residual resistance ratio (RRR≈1.25) and electronic mean free path ($\ell \approx$ 11nm) of our thin film are very much lower than for the single crystals investigated elsewhere in the literature. The consequences of the short ℓ for all of the above mentioned candidate mechanisms of vortex attraction are now briefly discussed.

In addition to the 6 theories offered by Brandt and Das, Type 1.5 theory gives us 7 possible origins of the vortex-vortex attraction.[114] Now listed and labelled here as: (1)-BCS corrections to the GL theory;[147] (2)- Corrections to simple GL or London theories;[148] (3)- Tilted fields;[149] (4)- A type of "Casimir" force in layered materials;[150] (5)- A closely related thermally activated van der Waals (vdW) type interaction;[151]; (6)- An impurity activated vdW-like interaction;[152] and (7)- Type 1.5 theory.[100]

Mechanism (1) originates from BCS corrections to the GL theory. It is responsible for the vortex patterns seen in the low-κ Type-II\1 superconductors and was predicted to occur theoretically for $0.71 \leq \kappa \leq 1.5$. Experimental investigation of the Type-II\1 / Type-II\2 phase boundary found good agreement with this and defined limits of $0.45 \lessapprox \kappa \lessapprox 1.1$ for this mechanism of vortex attraction.[153]

Calculations of MgB_2 in the clean limit certainly put κ_π in this regime,[100] but our consideration of ℓ predicts κ_π =2.2, κ_σ =3.6 for our sample and pushes us far outside these limits (see treatment of $\kappa_\pi, \kappa_\sigma$, ℓ in discussion of mechanism (7)). Therefore it seems unlikely that this is an appropriate mechanism for describing the vortex attraction in our thin films.

Mechanism (2) originates from a non-local extension of the London model with Pippard theory. This gives rise to an oscillating vortex potential that can realise an attractive tail to inter-vortex interactions. This attraction is predicted to exist when the relation $\Re[\Lambda^{-1}] > \xi_o^{-1}$ is satisfied. Λ and ξ_o are the magnetic and order parameter "decay lengths" respectively,[148] but are related non-trivially to the standard penetration depth and coherence length of superconductors, c.f. equations 2.17 and 2.18 in reference.[154] As such it is unclear from the theory, as it stands now, in which regime MgB_2 lies. However, as both of these variables are strongly dependent on the electronic mean free path,[155] quantification of this relation for the spread of ℓ over the MgB_2 systems studied so far could shed further light on the applicability of this mechanism to MgB_2.

Mechanism (3) involves applied fields tilted at $\approx 70^o$ to the c-axis of layered materials. Such chains have been observed in the highly anisotropic BSCCO,[156] and moderately anisotropic YBCO ($\Gamma \approx 5$),[157] at field tilts of 70^o and 75^o respectively. Conservative estimates of the field misalignment in our system put it at $<2^o$ and so this mechanism seems unlikely. A review of vortex chaining due to tilted fields in highly anisotropic systems is contained elsewhere.[158]

The Casimir-like force (4) and the vdW-like (vdW) interaction (5) involve thermal activation of vortices and so are unlikely to operate at the temperatures of this experiment ($T \approx 1.6K$) which were far below the critical temperature (T_c = 35.85K). Additionally (4) is active only at sample edges (the images published here were taken $\approx$1mm from sample edge) and (5) is dominant only in highly anisotropic materials. The anisotropy parameter of the previously studied system (BSCCO-2212) is $\Gamma = \lambda_c/\lambda_{ab} > 150$,[142] whereas in comparison MgB_2 is only moderately anisotropic with $\Gamma \approx 5$.[159]

Mechanism (6) is developed for layered or highly anisotropic systems. Interestingly for our sample, this mechanism requires small levels of impurity but is destroyed by increasing levels of disorder. The optimum vortex spacing predicted by this model is $\approx 1.5\mu m$, of the order of that seen in MgB_2 here and

elsewhere.[103] However, this model is again developed for highly anisotropic BSCCO-2212, which lies somewhat outside of the regime of MgB_2, and therefore seems unlikely. Unfortunately, within the theory in its current state, the coefficients of this disorder induced attraction are not precisely determined preventing further quantifiaction of this mechanism for MgB_2.[152]

A key premise of mechanism (7), Type-1.5 theory, is that the two component GL model of a two-band superconductor has *three fundamental length scales*, not the two of standard one-component treatments of superconductivity. Here the system can no longer be paramaterized by a single dimensionless quantity κ and a long range vortex attraction and short range repulsion, among other properties, appears in the regime $\xi_1 < \sqrt{2}\lambda < \xi_2$, where λ is the magnetic penetration depth and strictly speaking, ξ_1, ξ_2 are characteristic variations of the density fields known as "inverse field masses", not coherence lengths attributable to π and σ band condensates. Unfortunately, analytical solutions of ξ_1 and ξ_2 are not available except in special cases,[160] and so evaluation of this inequality for our present case is not currently possible. However, in the limit of negligble interband Josephson coupling, these lengthscales do become equivalent to two independent coherence lengths of the condensates ξ_π, ξ_σ, and so the remainder of this analysis will proceed having followed this assumption.

In the dirty limit, $\ell \ll \xi$ the characteristic lengthscales of superconductivity are dependent on ℓ in the following way.[161]

$$\lambda_{eff}(T) = \frac{\lambda_L}{(2(1-t))^{\frac{1}{2}}} \cdot \left(\frac{\xi_0}{1.33\ell}\right)^{\frac{1}{2}} \tag{5.1}$$

$$\xi(T) = \frac{0.855\,(\xi_0 \ell)^{\frac{1}{2}}}{(1-t)^{\frac{1}{2}}} \tag{5.2}$$

Where λ_L is the London penetration depth, ($\xi_0 = \hbar\nu_F/\pi\Delta_0$) is the BCS coherence length and $t = T/T_c$, where T_c is the superconducting critical temperature. $\lambda_L^\pi = 33.6$nm and $\lambda_L^\sigma = 47.8nm$ are defined to parameterize the ground state superfluid densities of the condensates from the respective plasma frequencies $\omega_{p\pi}$ and $\omega_{p\sigma}$,[162] and the equation $\lambda_L = c/\omega_p$.[141] The BCS coherence lengths $\xi_0^\pi = 51nm$ and $\xi_0^\sigma = 13nm$ are calculated from the Fermi velocities ($\nu_F^\pi = 5.35 \times 10^5 ms^{-1}$, $\nu_F^\sigma = 4.4 \times 10^5 ms^{-1}$),[163] and the band gaps $\Delta_\pi(0) = 2.2$

meV,[164, 165] $\Delta_\sigma(0) = 7.1$ meV.[166, 167]

Combining all of the above values with $\ell = 11$nm, and a measurement temperature T =1.6K, into equations 5.1 and 5.2 returns the following: $\lambda^\pi_{eff} = 45.4nm$, $\xi^\pi = 20.7nm$, $\lambda^\sigma_{eff} = 47.8nm$, $\xi^\sigma = 13.3nm$, where the σ-band is presumed to be in the "clean" limit. In a two-band superconductor, the superfluid densities of both bands contribute to the screening of external magnetic fields. Therefore the magnetic penetration depth λ is defined as $\lambda = [1/\lambda_\pi^2 + 1/\lambda_\sigma^2]^{-\frac{1}{2}}$, which in this case yields $\lambda = 33$nm. $\sqrt{2}\lambda = 47$nm and so this analysis puts us far outside the Type 1.5 regime defined as $\xi_1 < \sqrt{2}\lambda < \xi_2$, although we stress that the use of BCS coherence lengths in the evaluation of this equality is only valid when the interband Josephson coupling is negligible.

Alternatively, with some extremely careful reservations, one can introduce two κ's where $\kappa_i = \lambda_i/\xi_i$ $(i = \pi, \sigma)$.[100] The predictable consequence of a short ℓ is to push this system further into the Type II regime where the Ginzburg-Landau parameter $\kappa > 1/\sqrt{2}$. κ_π =2.2, κ_σ =3.6 are now strongly Type II and are also in reasonable agreement with experimentally defined values used in a two-band GL model elsewhere.[141]

Again we stress that both the preceding analyses concerning Type 1.5 superconductivity are weakened by the use of standard BCS coherence lengths for evaluation of the critical inequality. This approach is only valid in the regime of negligible interband Josephson coupling and conclusions drawn from them need to be treated with care.[105] A proper analysis most likely requires the analytic definition of ξ_1 and ξ_2, the characteristic variations of the density fields often defined as "inverse field masses", μ_1^{-1}, μ_2^{-1} in recent literature, and this is the current focus of ongoing theoretical work.[168, 169] The recent theoretical development of Type 1.5 superconductivity is summarised in a forthcoming review.[110] Finally, it should also be noted that the Type 1.5 regime is only predicted to exist when $\xi_1 < \sqrt{2}\lambda < \xi_2$ *and* when vortices are shown to be thermodynamically stable. A condition which is described to have been met in high quality single crystal MgB_2.[105, 170, 160]

Closely related to, but subtly different from the Type 1.5 theory has been the development of *extended* GL theory.[111, 112] This work expands the GL treatment to 4^{th} order derivatives and introduces *healing lengths* that are similar to μ_1^{-1}, μ_2^{-1} of Type 1.5 Theory. As with Type 1.5 theory analytical calculation

of these quantities is difficult but qualitatively at least, in the context of these measurements, one might expect that the disparity of the healing lengths in the EGL is reduced as the high inter-band scattering rate causes them to converge on a single value, rendering the vortex interaction monotonic.[113]

5.5 Conclusion

We have directly imaged the local stray magnetic fields at the surface of a 160nm thick MgB_2 thin film with relatively high levels of disorder as a function of applied field. We observe the spontaneous ordering of vortices into stripes with a predominant chaining direction at the three lowest fields, and a labyrinth at the highest field. We note that while these patterns are similar to those formed in systems with a competing short-range repulsion and long-range attraction, they are perhaps more characteristic of a vortex-vortex interaction that has short-range repulsive, intermediate range attractive and long-range repulsive components. At the lowest and highest fields the vortex configurations are characterised by a bi-modal distribution to the nearest neighbour bond lengths which we attribute to the intra- and inter-chain bond lengths. Images at intermediate fields also show chaining of vortices while, at the second lowest field, this coincides with an approximately Gaussian distribution of vortex separations. We tentatively postulate that at this vortex density, the equilibrium spacing and Abrikosov lattice parameter are roughly equivalent. A detailed ordering analysis of the vortex structures at the 3 lowest fields reveals that the preferential direction of the chaining varies by approximately 45^o, and at the highest field shows no predominant direction, apparently discounting the role of materials based effects on the symmetry breaking of the vortex lattice.

The suitability of seven candidate mechanisms for the intermediate-range vortex attraction in MgB_2 have been reviewed in light of the extremely short electronic mean free path of our sample. Five of the seven mechanisms seem unlikely. Of the remaining two, serious reservations regarding the analysis of Type 1.5 theory are made, and quantification of the suitability of this theory is hindered by a lack of analytical solutions to the fundamental length scales, μ_1^{-1}, μ_2^{-1}. The remaining suitable candidate involves oscillatory behavior of magnetic fields (labelled as mechanism (2)) of this paper) and further theoretical work is also needed

to ascertain if this is likely to be active in MgB_2.

Chapter 6

Geometry-dependent penetration fields of superconducting $Bi_2Sr_2CaCu_2O_{8+\delta}$ platelets

6.1 Motivation

In Type-II superconductors the Meissner phase is separated from the mixed phase by the lower critical field H_{c1}. As the applied field is increased above H_{c1} superconductivity is gradually surpressed and flux steadily enters the sample in the form of quantised tubes known as *superconducting vortices*. c.f. Section 2.5. Any conceivable applications of Type-II superconductors will invariably exploit the benefits of a dissipationless persistent current. Unfortunately, the presence of a transport current subjects vortices to a Lorentz force, under which they move and dissipate energy, and thus the material will experience resistive effects with obvious disastrous consequences for superconductivity.

Vortices are often trapped by regions of suppressed order parameter known as pinning sites which opposes this motion. Such sites are often a result of sample impurities or crystalline imperfections and as such a material's critical current (J_c) is a direct measure of its pinning strength and purity. Indeed, the behaviour and control of vortices on pinning landscapes, both natural and artificial, has been the subject of intensive research in recent decades.

In parallel with attempts to study the behaviour of vortices once inside a su-

perconducting system, progress has been made in understanding the mechanisms of flux penetration. For instance it is now known that several energy and surface barriers exist that prevent the penetration of flux into a sample until an applied field of H_p, known as the *penetration field* where $H_p > H_{c1}$.[87, 88, 85, 171, 172, 173, 89, 89]

Perhaps of greater significance are *demagnetisation effects*, whereby Meissner shielding diverts, distorts and enhances the applied field around a sample making the local effective field a strong function of position in an arbitrarily shaped sample. A greater understanding of this enhancement leading to more accurate modelling is crucial to our ability to predict vortex penetration and extend the flux-free state.

6.2 Theory of demagnetising fields

A well known problem of magnetostatics is the calculation of the internal magnetic field (H_i) of an arbitrarily shaped sample in the presence of a uniform external applied field (H_a). Consideration of the magnetic induction $B = \mu_0(H + M)$ and Maxwell's 1st equation $\nabla \cdot B = 0$ leads to:

$$\nabla \cdot \mathbf{H} = -\nabla \cdot \mathbf{M} \tag{6.1}$$

The internal magnetisation of a magnetised body faces a discontinuity, and hence a divergence, at the sample surface. Equation 6.1 tells us that this generates a divergence in magnetic field of equivalent magnitude that opposes **M**. Historically this problem was first considered in relation to ferromagnetic materials where the spontaneous internal field *opposes* the applied field, and is hence termed the *demagnetising field*, H_D. In the special case of a superconductor in the Meissner phase (perfectly diamagnetic) it is clear that H_D lies in the same direction as H_A and therefore *enhances* the applied field, as illustrated schematically in figure 6-1. Herein lies the origin of demagnetisation effects and the geometrical dependence of penetration fields in superconducting materials.

The internal field (H_i) of a superconductor in the Meisnner phase therefore has an additional component H_D,

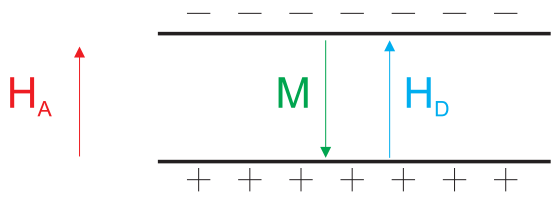

Figure 6-1: The demagnetising field in an infinite plane superconductor in the Meissner phase. An internal magnetisation (**M**) equal and opposite to the applied field ($\mathbf{H_A}$) is spontaneously generated. A positive (negative) divergence of (**M**) at the sample top (bottom) requires a negative (positive) divergence of **H** (c.f. Equation 6.1) and the creation of negative (positive) magnetic poles. The resultant field flows from positive to negative poles and is termed the *demagnetising field* ($\mathbf{H_D}$).

$$\mathbf{H_i} = \mathbf{H_A} + \mathbf{H_D} \tag{6.2}$$

For the infinite plane superconductor considered in figure 6-1 the demagnetising field and magnetisation are simply related by H_D =-M. In arbitrarily shaped samples however H_D is not so clearly defined and becomes $\mathbf{H_D}$ =-D**M** where $0 \leq D \leq 1$ is a scalar unique to a specific sample geometry termed the *demagnetisation factor*.

$$\mathbf{H_i} = \mathbf{H_A} - D\mathbf{M} \tag{6.3}$$

Considering the special case where $\mathbf{M} \propto \mathbf{H}$ the simple relationship $\mathbf{M} = \chi\mathbf{H_i}$ holds. Then for a superconductor in the Meissner phase ($\chi = -1$) it follows that,

$$\mathbf{H_i} = \mathbf{H_A} - D\chi\mathbf{H_i} \tag{6.4}$$

and,

$$\mathbf{H_i} = \frac{\mathbf{H_A}}{(1-D)}, \tag{6.5}$$

where we find that $\mathbf{H_A}$ is scaled by a factor of (1-D). The demagnetisation factor D is notoriously difficult to define for arbitrarily shaped bodies and in fact analytical solutions only exist for ellipsoids where the special cases of infinite cylinder, sphere and infinite disk are described by D=0, 1/3 and 1 respectively. Any departure from this situation dramatically increases the complexity of the

problem. Nevertheless, full solutions for e.g. orthorhombic geometries, do exist but require lengthy and time consuming calculations by numerical methods such as those described in [174]. As such, D is often estimated using equivalent ellipsoids as described in more detail later in this chapter.

So far this analysis has only involved the field inside the superconductor H_i. We develop the theory further to describe the local field at the surface H_L with consideration of the rule of conservation of H at a sample boundary i.e. the tangential component of H is conserved. By taking into account the fact that H_i, is parallel to H_A, the tangential component of H_i at the surface of an ellipse will be greatest at the equatorial line perpendicular to H_A, as illustrated in figure 6-2. H_L therefore varies continuously from a maximum at the equator, where penetration occurs first, to a minimum at the poles. Taking the special case of a sphere (D=1/3) we see that the actual penetration field is related to the lower critical field via equation 6.5 and is defined as $H_p = 2/3 * H_{c1}$.

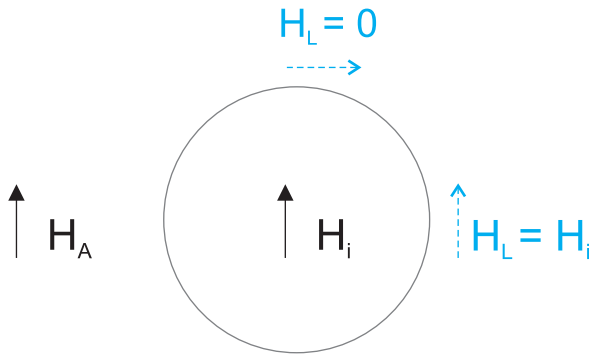

Figure 6-2: The *local* field $\mathbf{H_L}$ at the surface of a magnetised ellipsoid is given by the tangential component of the *internal* field $\mathbf{H_i}$ which varies continously from H_i at the equator to 0 at the poles.

6.3 Experimental method

Microfabricated structures on the surface of $Bi_2Sr_2CaCu_2O_{8+\delta}$ (BSCCO) single crystals have been shown to be model systems for investigating surface barriers (Bean-Livingston and geometrical) to flux penetration.[91, 83] Previous works have focused on investigations of the temperature dependence of penetration into circular disks of various sizes. Here we describe an extension of these studies to

look at the role that the sample geometry plays in the vortex penetration process. We have fabricated arrays of BSCCO disks, pentagons, squares, and triangles of fixed known area and measured their temperature-dependent penetration fields $H_p(T)$ using differential magneto-optic imaging (MOI). In the regime studied $H_p(T)$ was observed to decay exponentially with temperature and, in stark conflict with conventional estimates of the demagnetisation factors, falls with the decreasing degree of symmetry of the sample.

Single crystals of BSCCO ($T_c \sim 92K$) were grown using the floating zone method.[175] Arrays of shallow pillars with the four different symmetries were etched into the surface of freshly cleaved crystals using optical lithography and argon ion-milling techniques. Optical micrographs of typical sample arrays are shown in Fig. 6-3. In each case, structures of different area are patterned at the corners of a repeating 40μm square cell and the pillar height is 300nm. The four sizes of the circular disks (A1-A4) have diameters: 20, 15, 10 and 5 μm and the dimensions of the other regular polygons have been designed to conserve these four areas (table 6.1).

We assume that the influence of the underlying optimally doped BSCCO platelet on $H_p(T)$ is negligible due to the substantial suppression of bulk pinning in our measurement temperature range (45K - 80K).

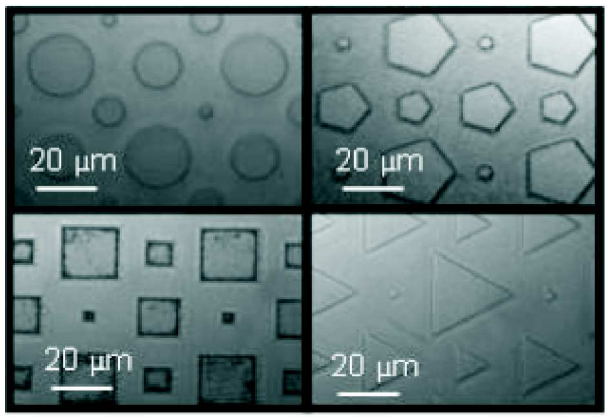

Figure 6-3: Optical micrographs of four typical BSCCO samples.

Magneto-optical imaging (MOI) has previously been shown to be a very useful technique for studying flux penetration into BSCCO mesostructures[91] and the technique is discussed in detail in chapter 3. The numerical difference between

Table 6.1: Areas of the four structure sizes labelled A1-A4, equivalent to disks of diameter 20, 15, 10 and 5 m respectively.

Mesostructure	Area (μm^2)
A1	$\pi \times 10^2$ =314.2
A2	$\pi \times 7.5^2$ =176.7
A3	$\pi \times 5^2$ =78.5
A4	$\pi \times 2.5^2$ =19.6

two images captured at slightly different magnetic fields (henceforth termed a difference image) is used to map flux penetration as the subtraction enhances contrast and removes unwanted artefacts, such as domain walls and scratches in the garnet indicator, from individual images. Figure 6-4 shows some typical difference images used to establish H_p in circular disk-shaped samples at 55K. At low fields flux was found to enter only the interstitial areas of the array as seen in Fig. 6-4(a). At higher fields the most noticeable flux changes are those within the pillars. H_p is identified as the lowest field at which penetration into a structure of given area is observed.

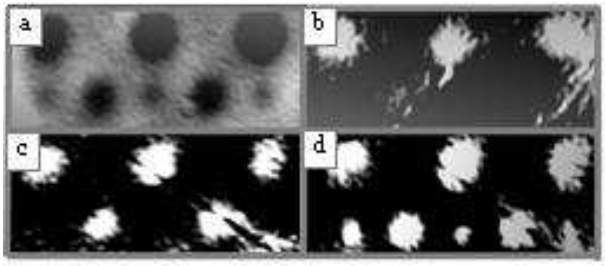

Figure 6-4: Magneto-optical difference images of an array of microscopic BSCCO disks at 55 K. The circles of white contrast correspond to flux penetration into the disks. The fine structure is an imaging artefact most likely due to a combination of scratches in the garnet indicator and cryo-cooler vibrations. (a) [25 Oe - 0 Oe] displays the Meissner screening signature of the pillars as flux enters interstitial areas at low fields. (b) [35 Oe - 30 Oe], (c) [39 Oe - 34 Oe], and (d) [43 Oe -38 Oe] show flux entering the 20, 15 and 10 μm diameter shapes respectively as the field increases. The smallest (A4) structures lay outside the spatial resolution of this experiment.

6.4 Results

When an external field is applied along the c-axis, the highly layered structure of BSCCO means that vortical supercurrents are confined to the CuO_2 layers and so flux tubes are broken up into stacks of weakly interacting *pancake vortices* (PVs).[176] It is now known that a single PV can penetrate a sample independently and drag the rest of a stack with it,[177] and several experimental and theoretical studies have established the Bean-Livingston barrier as the dominant barrier for PVs in BSCCO at T > 15K.[83, 178, 173, 179]. Theory predicts H_p(T) will take the form:[83, 173]

$$H_p = P\frac{\sqrt{2}\kappa}{ln\kappa}H_{c1}(0)\left[1-\left(\frac{T}{T_c}\right)^2\right]e^{-T/T_0}, \tag{6.6}$$

where κ is the Ginzburg-Landau parameter, P is the inverse field enhancement factor, which is related to the demagnetisation factor (P=1-D) and $k_B T_0$ is a characteristic energy for the penetration process. For ease of comparison with Eq. 6.6, Figs. 6-5 and 6-6 display experimental data in the form $\ln[H_p(T)/(1-(T/T_c)^2)]$ versus T. Figure 6-5 displays penetration field data for the largest sized shape (A1) of each geometry in the temperature range 45K - 75K. Linear fits based on Eq. 6.6 have been plotted (choosing T_0 =34K and T_c =92K), and are in excellent agreement with our data, confirming the exponential temperature dependence predicted by Eq. 6.6. The prefactors $[(P\sqrt{2}\kappa/\ln\kappa)H_{c1}(0)]$ extracted from these fits are discussed later, as they contain information regarding the surface field enhancement and quantify the trend that is clearly observed in Fig. 6-5: H_p falls systematically with decreasing sample symmetry for a given sample area.

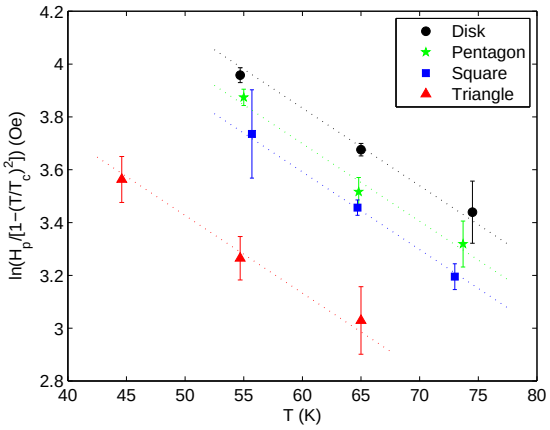

Figure 6-5: $\ln[H_p(T)/(1-(T/T_c)^2)]$ versus T for the largest BSCCO mesostructures (A1). Data points are experimental data; dashed lines are fits to Eq. 6.6 with T_0 =34K and T_c =92K.

MOI spatial resolution is limited by the finite sample/garnet spacing, and accurate sample preparation was paramount in achieving high resolution. This, combined with cryocooler vibrations of the order of $\sim 1\mu$m made it impossible to resolve penetration of flux into the smallest A4 structures in all cases. A2 and A3 exhibit the same trend as the A1 structures shown in Fig. 6-5, with T_0 =34K again providing an excellent description using fits based on Eq. 6.6. To illustrate this point, Fig. 6-6 plots the temperature dependence of the penetration field for the three largest square structures, each of which is seen to exhibit the same exponential temperature dependence with a different size-dependent prefactor.

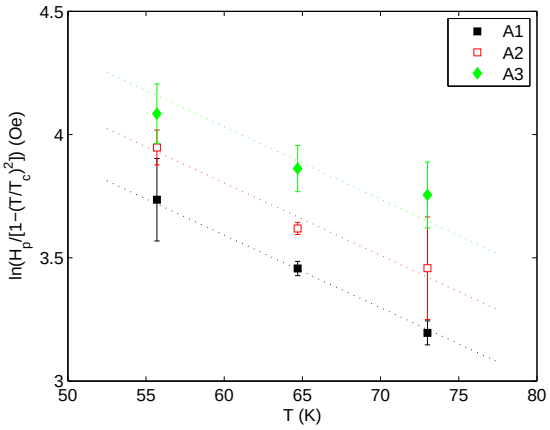

Figure 6-6: $\ln[H_p(T)/(1-(T/T_c)^2)]$ versus T for square BSCCO mesostructures. Data points are experimental data; dashed lines are fits to Eq. 6.6 with T_0 =34K and T_c =92K.

Analytical solutions for demagnetization factors exist only for ellipsoidal-shaped magnetic bodies. As a consequence, demagnetization effects in arbitrarily shaped superconducting bodies are commonly approximated by those for "equivalent" ellipsoids. For an ellipsoid with a magnetic field H_A applied parallel to one of the principal axes, the effective magnetic field (H_{eff}) at the equator is,[180]

$$H_{eff} = \frac{H_A}{1-D}, \tag{6.7}$$

where D is the demagnetisation factor which can take values between 0 and 1, and the inverse enhancement factor in Eq. 6.6 is $P = (1-D)$. For an oblate ellipsoid with principal axes (a, a, c) along (x, y, z) directions and with the field applied along z it can be shown that,[180]

$$D = \frac{1}{e^3}\left(e - \sqrt{1-e^2}\arcsin e\right), \tag{6.8}$$

where $e = (1-c^2/a^2)^{1/2}$. Expanding 6.8 to second order in c/a yields

$$P = (1-D) \cong, \frac{\pi}{2}\frac{c}{a} - 2\frac{c^2}{a^2}. \tag{6.9}$$

One might expect that a good approximation to the field at the edge of a disk of radius R and thickness d$\ll$R in a perpendicular field H_A could be obtained by

replacing the disk by an oblate ellipsoid with major axis b =R and minor axis c =d/2. Combining 6.7 and 6.9 (ignoring the second-order term) would yield the result for the field at the edge $H_{eff} = H_A(2a/\pi c) = H_A(4R/\pi d) \approx H_A(R/d)$. However, Geshkenbein and Larkin[181] suggested that a better approximation corresponds to a different choice of elliptical cross section with a larger semi-minor axis, such that the radius of curvature at the edge is approximately d/2.[181] (The radius of curvature of an oblate ellipsoid at $(x, y, z) = (a, 0, 0)$ is $\rho(a, 0, 0) = c^2/a$.) Zeldov et al.[85] have demonstrated that this leads to a more accurate value of $H_{eff} \cong H_A(R/d)^{1/2}$ in the limit $\lambda < d \ll R$, a result which was confirmed by experiments on mesoscopic BSCCO structures[91, 83] and our own observations here. The same approach has been used to estimate the penetration field in long strips and disks.[88, 86] Figure 6-7 shows the applied field at penetration plotted against the inverse quarter power of the sample area, $A^{-1/4}$. Since the areas (A1-A3) are proportional to the radius of the equivalent disks squared, the good linear fits are consistent with the expected functional relationship of $H_p \propto R^{-1/2}$. A more critical analysis of Fig. 6-7 reveals that, while the data for the triangular samples extrapolates to a point near the origin for $A^{-1/4} = 0$ as expected from Eq. 6.6, the data for squares and disks extrapolate to significant positive intercepts (9 Oe and 17 Oe respectively). Since penetration must surely occur at H$\sim$0 for an infinite platelet this suggests that these data points in Fig. 6-7 would be better described by a sublinear relationship that passes close to the origin. This apparent discrepancy may be due to the fact that we are not strongly in the limit described in reference [85] since d$\sim \lambda$ in our samples. It is interesting to note that plots of similar data for somewhat thicker BSCCO disks and squares actually exhibit negative intercepts at $(d/R)^{1/2}$.[83]

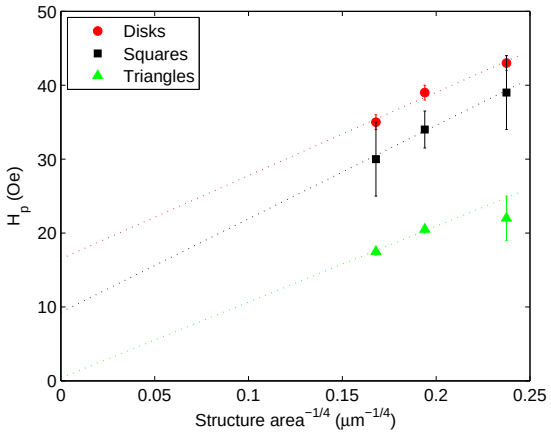

Figure 6-7: H_p versus $A^{-1/4}$ for disk-shaped, square, and triangular BSCCO mesostructures at T=55K. The smallest structures (A4) and the A3 pentagons were beyond the resolution of this experiment.

Theoretical fits to our experimental measurements based on Eq. 6.6 using T_0 =34K yield the values for the prefactor $[(P\sqrt{2}\kappa/\ln\kappa)H_{c1}(0)]$ recorded in Table 6.2. These are in reasonably good agreement with other similar measurements in the literature.[91, 83] Taking $\kappa \approx 100$ and $H_{c1}(0)$≈100 Oe,[91, 172] we can then estimate the values for the inverse enhancement factor P for each geometry and size.

6.5 Discussion

Many theoretical studies have been devoted to the calculation of demagnetisation factors for magnetic bodies with a range of regular shapes. Much of this work has arisen in the context of ferromagnetism where accurate demagnetisation factors are vital for the precise calculation of magnetostatic energies. Since demagnetising fields are not uniform in arbitrarily shaped bodies, such calculations yield effective average values; for example, the magnetometric demagnetizing factor of an arbitrary sample in the z-direction, D_z, can be defined as the factor that makes the magnetostatic self-energy per unit volume equal to $2\pi D_z M_s^2$, where M_s is its saturation magnetisation. A comparison with estimates based on values obtained from equivalent ellipsoids is frequently made. For example, Aharoni presents analytical results for the demagnetisation factors of rectangular ferro-

magnetic prisms and notes very significant discrepancies from values obtained for a prolate spheroid with the same aspect ratio.[182] To address this issue, Beleggia *et al.*[183] have calculated the equivalent ellipsoid for uniformly magnetised disks, cylinders with elliptical cross-section and prisms, by imposing equality between the demagnetisation factors of the two shapes of *equal* volume. Demagnetisation factors have also been calculated for magnetic materials under other assumptions, e.g., for a fixed value of the magnetic susceptibility, χ. Making an explicit connection to the Meissner state in superconductors, Pardo et al.[184] and Chen et al.[185] have numerically calculated the magnetometric demagnetisation factors for perfectly diamagnetic ($\chi = -1$) square prisms and cylinders.

The above methods of estimating demagnetisation factors of polyhedra have commonly been approximated by inscribed ellipsoids of revolution.[186] In our case, and imposing the above condition on the radius of curvature at the edge, $c^2/a = d/2$, this corresponds to a choice of $a = b = r_n$, $c = (r_n d/2)^{1/2}$ and (from Eqn. 6.9) $P_i(n) \cong (\pi^2 d/8r_n)^{1/2}$, where r_n is the inscribed radius of a regular polygon with n-fold rotational symmetry (the subscript i denotes use of an inscribed circle). However, noting that the radii of inscribed circles r_n vary as $r_3(tri) < r_4(squ) < r_5(pent) < r_\infty(disk)$, it is evident that this approach gives $H_p^3 > H_p^4 > H_p^5 > H_p^\infty$. The experimentally measured field enhancement parameters (P_{exp}) are listed alongside these theoretical estimates (P_i) in Table 6.2 and it is clear that the trend of the predictions for inscribed ellipsoids are in direct contradiction with our experimental observations. We note that the penetration fields of similar freestanding BSCCO microstructures (circular disks and squares) were also compared in Ref. [83]. Although the authors did not comment on it in that paper, and data were not presented at directly comparable temperatures for the two shapes, their penetration fields for squares also appear to be significantly lower than circular disks of the same width and thickness for T $\geq$45K.

In practice, however, penetration in our pillars occurs at the point on the surface where the effective field (demagnetising field) is highest, and these average calculations are of little practical use. Moreover, none of these works accounts for the penetration of flux lines in a realistic way; for example, the field lines at the edges do not have the expected curvature as discussed above.[181] Berdiyorov et al.[187] describe a theoretical study that addresses a situation much closer to the one found in our experiments. They have calculated numerical solutions to

the non-linear Ginzburg-Landau equations for vortex penetration into mesoscopic superconducting disks, rings, and squares. They find that the Bean-Livingston energy barrier that has to be overcome for a single vortex to enter a sample is lower at the middle of one edge of a square than on the circumference of a disk of the same width and thickness. Hence first flux penetration occurs at significantly lower fields in the square, in apparent agreement with our experimental observations. We note, however, that these calculations have been made for samples with R= 4ξ, d= 0.1ξ, and $\kappa = 1$ and so are in a very different regime from our samples with R$\gg \xi$, d=$\gg \xi$, and $\kappa \approx 100$.

Finally we make the empirical observation that the qualitative trend exhibited by our experimental data is captured if we base equivalent ellipsoids on the radius of the *circumscribed* circle instead of the *inscribed* circle considered above. The radius, R_n, of a circumscribed circle surrounding an n-sided regular polygon with side of length S_n is

$$R_n = \frac{S_n}{2\sin(\pi/n)}. \tag{6.10}$$

Choosing $a = b =$R$_n$, and $c = (R_n d/2)^{1/2}$, theoretical values of $P_c(n)$ (the subscript c denotes use of a circumscribed circle) for our BSCCO platelets have been generated by combining Eqs. 6.9 and 6.10 and are displayed in Table 6.2. Comparing experimental data with the circumscribed circle model, we note that the trend with decreasing degree of symmetry is now correct. However, a comparison of columns P_{exp}/P_{ref} and $P_c(n)/P_{c,ref}$, where the inverse enhancement factors have been normalized by that of a reference disk of area A1, reveals that the theoretical predictions do consistently overestimate the observed values. Aside from these numerical differences, we believe that this is the first time that it has been pointed out that equivalent ellipsoids based on circumscribed rather than inscribed circles yield a qualitatively better estimate of the trend in demagnetisation factors as a function of degree of symmetry in polygon-shaped superconducting platelets. Our observations have rather important implications for the estimation of appropriate effective demagnetisation factors for flux penetration into arbitrarily shaped superconducting bodies. In particular, it is surprising that the experimental field enhancement factor for the triangular platelets is so much larger than the other structures. Clearly a model based on circumscribed

circles is too simple to capture all the physics of the probelm of flux penetration which must also consider the distribution of supercurrent densities and the role of sharp/rounded corners etc. Hence we hope that this research will stimulate new theoretical work to fully understand this.

Table 6.2: Experimentally and theoretically derived inverse enhancement factors P for various BSCCO mesostructures. The areas of the n-sided regular polyhedra A1-A3 are contained in Table I. P_i(n) and P_c(n) are theoretically derived using the methods of inscribed and circumscribed ellipsoids respectively. P_{ref}, $P_{i,ref}$ and $P_{c,ref}$ are the experimental and theoretical values of P for the A1 disk structure. The height of mesoscopic pillars is 300 nm in all cases.

Mesoscopic structure	P_{exp}	P_{exp}/P_{ref}	$P_i(n)$	$P_i(n)/P_{i,ref}$	P_c(n)	$P_c(n)/P_{c,ref}$
A1 - Disk	0.0893 ± 0.0016	1.000	0.166	1.000	0.166	1.000
Pentagon	0.0787 ± 0.0018	0.882	0.172	1.032	0.157	0.942
Square	0.0699 ± 0.0010	0.783	0.175	1.054	0.151	0.907
Triangle	0.0446 ± 0.0010	0.500	0.185	1.112	0.137	0.823
A2 - Disk	0.1053 ± 0.0053	1.179	0.188	1.131	0.188	1.131
Square	0.0877 ± 0.0022	0.983	0.198	1.189	0.171	1.027
A3 - Square	0.1136 ± 0.0031	1.273	0.233	1.402	0.202	1.217

Chapter 7

Final conclusions and future work

7.1 Chiral supercurrents in Sr_2RuO_4

A search for "smoking gun" magnetic signatures of chiral p-wave superconductivity in Sr_2RuO_4 via scanning Hall probe microscopy has returned a null result. Consequently the case for this exotic ordering remains unresolved and the continued absence of these signals from real-space imaging measurements suggests the need for considerable revision of current p-wave models, or even consideration of alternative pairing symmetries. It is currently unclear how further magnetic imaging experiments of Sr_2RuO_4 could complement this process.

However, several questions remain unresolved regarding the "top hat" magnetic field profiles of Sr_2RuO_4 mesoscopic disks. To a certain extent the current uncertainty around these measurements lies in the fact we are comparing field-cooled (FC) measurements with zero-field-cooled theory. The measurement protocol was restricted to FC to prevent the sample entering the critical state, therefore avoiding irregular avalanches of flux into the bulk. Another way to avoid flux-jumps would be to attempt ZFC while the sample is held at a temperature very close to T_c. The increased thermal energy of vortices then may be sufficient to render pinning sites impotent and allow formation of a true equilibrium flux distribution. Repetition of this experiment while systematically varying the thickness of the underlying platelet would confirm/rule out the influence of the bulk single crystal on the unexplained profiles. A search for such profiles in similar structures fabricated in different materials would also verify whether or not the unexplained profiles in Sr_2RuO_4 disks are a direct consequence of physics

intrinsic to this material.

7.2 The inter-vortex attraction in MgB_2

The scanning Hall probe imaging of a MgB_2 thin-film revealed vortex configurations consistent with the presence of an attractive component in the inter-vortex interaction in our sample. This finding is in agreement with observations in single crystals from the literature, but the origin of the attraction is currently the focus of intense scientific debate.

These results and the accompanying review of candidate mechanisms, conducted in light of the very high disorder expected in our sample, have highlighted several promising areas for further investigation. A current lack of theoretical understanding is frustrating a proper analysis but it is hoped that this work will stimulate further theoretical development in these areas.

In the meantime, several extensions of this experimental work could shed further light on the origins of the active mechanism. Of particular interest is the behaviour of the labyrinth at higher fields. A transition to triangular ordering at very high fields would be consistent with the results of several simulations, and if it exists, the field strength at the transition will yield information about the disparate length-scales of the vortex interaction, knowledge of which will be crucial to developing a theoretical understanding. The increased vortex density would however, probably have put this transition beyond the spatial resolution of this experiment, but further attempts using smaller Hall probes, with greater care to reduce the sample/sensor separation stand a good chance of success.

Additionally, systematic variation of the interband scattering is achievable by varying the film thickness. A repetition of this experiment for several different film thicknesses could prove to be extremely interesting as any alteration in the vortex behaviour with thin-film thickness will again speak for the lengthscales of the inter-vortex interaction.

Finally, the influence of underlying crystalline disorder on vortex patterns always leaves some room for doubt as to the genuine intrinsic nature of the underlying physics responsible for the pattern. The influence of pinning sites on the vortex configurations can be evaluated by making repeated field-cooled cycles in the same location. Such measurements will reveal if the vortex pattern

is indeed dominated by a low density of strong pinning sites.

7.3 Demagetisation factors of superconductors

The magneto-optical imaging of flux penetration into BSCCO microstructures revealed that conventional estimates of inverse field penetration factors ($P = (1 - D)$) were in direct contradiction with experimental observations. Rather than calculating estimates using equivalent ellipsoids based on *inscribed* circles of revolution, it was noticed empirically that the correct qualitative trend is instead given by *circumscribed* circles.

Unfortunately there remains some discrepancy in the quantitative comparison, with theoretical estimates consistently overestimating the experimental values. Normalised to the disk, $P_{exp} = [1.000, 0.882, 0.783, 0.500]$ while $P_{theory} = [1.000, 0.942, 0.907, 0.823]$ for disks, pentagons, squares and triangles respectively. Perhaps the quantitative mismatch is not so surprising considering that these simplified estimates are not expected to capture all of the physics surrounding flux entry into a microscopic sample. Indeed, numerical solutions to the non-linear Ginzburg-Landau equations capture the correct trend, but in addition to being far outside the regime of this experiment, are currently insufficient to offer a quantitative comparison.

It is hoped that an extension of this theoretical work will be stimulated by the results of this thesis. In the meantime, several extensions of the experimental work could also be extremely valuable. It would be interesting to observe whether or not the same ratios of the normalised $P_{exp}s$, from disks to triangles, crop up over a range of aspect ratios (d/R). All of the structures involved in this study were d=300nm and so the most convenient way to systematically alter the aspect ratio is to simply alter d by varying the milling time during fabrication.

Furthermore, it would be interesting to observe P_{exp} in similar structures fabricated in different materials. Flux entry in BSCCO is governed by the penetration of pancake vortices over the Bean-Livingston energy barrier. By choosing different materials (Type I or Type II) it is possible to isolate the sample shape effects from energy and surface barrier physics and confirm the P_{exp} dependence we observe is truly geometric in origin. Finally, the fabrication of truly freestanding structures, either in BSCCO or thin film metal, would allow the role of the

underlying platelet to be probed.

7.4 List of publications

The following is a list of publications related to the experimental work described in this thesis.

P.J. Curran, J.R. Clem, S. J. Bending, Y. Tsuchiya and T. Tamegai, "Geometry-dependent penetration fields of superconducting $Bi_2Sr_2CaCu_2O_{8+\delta}$ platelets", *Physical Review B* **82**, 134501 (2010)

P.J. Curran, V.V Khotkevych, S. J. Bending, A.S. Gibbs, S.L. Lee and A.P. Mackenzie, "Vortex imaging and vortex lattice transitions in Sr_2RuO_4 single crystals ", *Physical Review B* **84**, 104507 (2011)

S.J. Bending, P.J. Curran, W.M.A. Desoky, V.V. Khotkevych, A. Gibbs, A.P. Mackenzie, T. Tamegai and S.E. Sebastian, "Vortex imaging in unconventional superconductors", *Physica C* **479** (2012) 65-68

Bibliography

[1] M. Augustus and B. Moritz von, "On the Influence of Temperature on the Electric Conducting Power of Metals," *Phil. Trans. R. Soc. London*, vol. 152, pp. 1–27, 1862.

[2] H. K. Onnes, "Investigations into the properties of substances at low temperature, which have led, amongst other things, to the preparation of liquid helium," *Nobel Lecture*, 1913.

[3] W. M. and R. Oschenfield., "A new effect concerning the onset of superconductivity," *Die Naturwissenschaften*, vol. 21, p. 787, 1933.

[4] F. London and H. London, "The electrodynamic equations of the supraconductor," *Proc. Roy. Soc. Lond. A*, vol. 149, pp. 71–88, 1935.

[5] A. G. Meshkovsky *Zh. Eksp. Teor. Fiz*, vol. 17, 1947.

[6] V. L. Ginzburg and L. D. Landau, "On the theory of superconductivity," *Zh. Eksp. Teor. Fiz*, vol. 20, p. 1064, 1950.

[7] A. A. Abrikosov, "On the magnetic properties of superconductors of the second group.," *JETP*, vol. 5, no. 6, 1957.

[8] U. Essmann and H. Trauble, "The direct observation of individual flux lines in type ii superconductors," *Phys. Rev. Lett.*, vol. 24A, p. 526, 1967.

[9] F. London, *Superfluids*, vol. 1. Wiley, 1950.

[10] E. Maxwell, "Isotope effect in the superconductivity of mercury," *Phys. Rev.*, vol. 78, p. 477, 1950.

[11] C. A. Reynolds, B. Serin, W. H. Wright, and L. b. Nesbitt, "Superconductivity of isotopes of mercury," *Phys. Rev.*, vol. 78, p. 487, 1950.

[12] H. Fröhlich, "Theory of the superconducting state. i. the ground state at the absolute zero of temperature," *Phys. Rev.*, vol. 79, no. 5, p. 845, 1950.

[13] L. N. Cooper, "Bound electron pairs in a degenerate fermi gas," *Phys. Rev.*, vol. 104, no. 4, p. 1189, 1956.

[14] A. C. Rose-Innes and E. H. Rhoderick, *Introduction of Superconductivity.* No. 6 in International Series in Solid State Physics, Pergamon, 2nd ed., 1978.

[15] J. Bardeen, L. N. Cooper, and J. R. Schrieffer, "Theory of Superconductivity," *Phys. Rev.*, vol. 108, no. 5, p. 1175, 1957.

[16] W. Corak, B. Goodman, C. Satterwaite, and A. Wexler, "Exponential temperature dependence of the electronic specific heat of superconducting Vanadium," *Phys. Rev.*, vol. 96, no. 5, pp. 1442–1444, 1954.

[17] W. Corak, B. Goodman, C. Satterwaite, and A. Wexler, "Atomic heats of normal and superconducting Vanadium," *Phys. Rev.*, vol. 102, no. 3, pp. 656–661, 1956.

[18] R. E. Glover and M. Tinkham, "Transmission of superconducting films at millimeter-microwave and far infrared frequencies," *Phys. Rev.*, vol. 104, p. 844, 1956.

[19] M. A. Biondi, M. P. Garfunkel, and A. O. McCoubrey, "Millimeter wave absorption in superconducting aluminum," *Phys. Rev.*, vol. 1427, p. 102, 1956.

[20] R. E. Glover and M. Tinkham, "Conductivity of Superconducting Films for Photon Energies between 0.3 and 40kT_c," *Phys. Rev.*, vol. 108, p. 243, 1957.

[21] W. Heisenberg *Z. Phys.*, vol. 39, p. 499, 1926.

[22] S. Bending, "Local magnetic probes of superconductors," *Adv. in Phys.*, vol. 48, pp. 449–535, Jul 1999.

[23] R. Broom and E. Rhoderick, "Studies of the intermediate State in Thin Superconducting films," *Proc. Phys. Soc.*, vol. 79, no. 509, pp. 586–&, 1962.

[24] T. Tamegai, L. Krusin-Elbaum, P. Santhanam, M. J. Brady, W. T. Masselink, C. Feild, and F. Holtzberg, "Spatially resolved magnetic hysteresis in a $YBa_2Cu_3O_{7-y}$ crystal measured by a Hall-probe array," *Phys. Rev. B*, vol. 45, no. 5, pp. 2589–2592, 1992. Cited By (since 1996): 18.

[25] R. Dingle, H. L. Strmer, A. C. Gossard, and W. Wiegmann, "Electron mobilities in modulation-doped semiconductor heterojunction superlattices," *App. Phys. Lett.*, vol. 33, no. 7, pp. 665–667, 1978. Cited By (since 1996): 218.

[26] J. S. Neal, *Superconducting and ferromagnetic micro-systems and hybrid structures studied by scanning Hall probe microscopy.* Phd thesis, Dept. of Physics, University of Bath, 2007.

[27] V. V. Khotkevych, M. V. Miloevi, and S. J. Bending, "A scanning hall probe microscope for high resolution magnetic imaging down to 300 mk," *Rev. Sci. Inst.*, vol. 79, no. 12, 2008. Cited By (since 1996): 3.

[28] M. Faraday, "Experimental researches in electricity. nineteenth series," *Phil. Tran. R. Soc. London*, vol. 136, pp. 1–20, 1846.

[29] P. B. Alers, "Structure of the intermediate state in superconducting lead," *Phys. Rev.*, vol. 105, pp. 104–108, Jan 1957.

[30] W. DeSorbo, "Study of the intermediate state in superconductors using cerium phosphate glass," *Phys. Rev. Lett.*, vol. 4, pp. 406–408, Apr 1960.

[31] H. and Kirchner, "Improved faraday technique for observing magnetic structures in superconductors," *Phys. Lett. A*, vol. 30, no. 8, pp. 437 – 438, 1969.

[32] I. M. W. Polyanskii A A, Vlasko-Vlasov V K and N. V. I, "Study of the intermediate state in superconductors using cerium phosphate glass," *Sov. Tech. Phys. Lett.*, vol. 15, p. 872, 1989.

[33] Z. Simsa, H. Le Gall, J. Simsova, J. Kolacek, and A. Le Paillier-Malecot, "Spectral dependences of Faraday rotation in $Y_{3-x}Bi_xFe_5O_{12}LPE$ films," *IEEE. Trans. Magn.*, vol. 20, pp. 1001 – 1003, Sep 1984.

[34] M. Wallenhorst, M. Niemöller, H. Dötsch, P. Hertel, R. Gerhardt, and B. Gather, "Enhancement of the nonreciprocal magneto-optic effect of tm modes using iron garnet double layers with opposite faraday rotation," *J. Appl. Phys.*, vol. 77, no. 7, pp. 2902–2905, 1995.

[35] R. Grechishkin, M. Goosev, S. Ilyashenko, and N. Neustroev, "High-res sensitive magneto-optic ferrite-garnet films with planar anisotropy," *J. Mag. and Mag. Mat.*, vol. 157, no. 0, p. 305, 1996.

[36] P. E. Goa, H. Hauglin, M. Baziljevich, E. Il'yashenko, P. L. Gammel, and T. H. Johansen, "Real-time magneto-optical imaging of vortices in superconducting $NbSe_2$," *Supercond. Sci. Tech.*, vol. 14, no. 9, p. 729, 2001.

[37] B. Kalisky, A. Shaulov, T. Tamegai, and Y. Yeshurun, "Magneto-optical measurements of the lifetime spectrum of transient vortex states in BSCCO," in *Magneto-optical imaging* (Johansen, TH and Shantsev, DV, ed.), vol. 142 of *NATO Science Series II-Mathematics Physics and Chemistry*, pp. 87–94, 2004.

[38] Y. Maeno, H. Hashimoto, K. Yoshida, S. Nishizaki, T. Fujita, J. G. Bednorz, and F. Lichtenberg, "Superconductivity in a layered perovskite without copper," *Nature*, vol. 372, no. 6506, pp. 532–534, 1994.

[39] J. Brison, L. Glemot, H. Suderow, A. Huxley, S. Kambe, and J. Flouquet, "Heavy fermion superconductivity," *Physica B*, vol. 280, pp. 165–171, May 2000.

[40] E. Chashechkina, I. Lee, S. Brown, D. Chow, W. Clark, M. Naughton, and P. Chaikin, "Interlayer decoupling, Lebed magic angle magnetoresistance and triplet superconductivity in (TMTSF)(2)PF6," *Synth. Met.*, vol. 119, pp. 13–18, Mar 2001.

[41] S. Saxena, P. Agarwal, K. Ahilan, F. Grosche, R. Haselwimmer, M. Steiner, E. Pugh, I. Walker, S. Julian, P. Monthoux, G. Lonzarich, A. Huxley,

I. Sheikin, D. Braithwaite, and J. Flouquet, "Superconductivity on the border of itinerant-electron ferromagnetism in UGe2," *Nature*, vol. 406, pp. 587–592, Aug 2000.

[42] S. J. Bending, "Local magnetic probes of superconductors," *Adv. in Phys.*, vol. 48, pp. 449–535, Jul-Aug 1999.

[43] C. Pfleiderer, M. Uhlarz, S. Hayden, R. Vollmer, H. von Lohneysen, N. Bernhoeft, and G. Lonzarich, "Coexistence of superconductivity and ferromagnetism in the d-band metal ZrZn2 (vol 412, pg 58, 2001)," *Nature*, vol. 412, p. 660, Aug 2001.

[44] F. Wilczek, "Majorana returns," *Nature*, vol. 5, pp. 614–618, Sep 2009.

[45] D. A. Ivanov, "Non-abelian statistics of half-quantum vortices in p-wave superconductors," *Phys. Rev. Lett.*, vol. 86, pp. 268–271, Jan 2001.

[46] A. Kitaev, "Fault-tolerant quantum computation by anyons," *Ann. Phys.*, vol. 303, pp. 2–30, Jan 2003.

[47] V. O. Dolocan, C. Veauvy, F. Servant, P. Lejay, K. Hasselbach, Y. Liu, and D. Mailly, "Observation of vortex coalescence in the anisotropic spin-triplet superconductor Sr_2RuO_4," *Phys. Rev. Lett.*, vol. 95, no. 9, p. 097004, 2005.

[48] J. R. Kirtley, C. Kallin, C. W. Hicks, E. A. Kim, Y. Liu, K. A. Moler, Y. Maeno, and K. D. Nelson, "Upper limit on spontaneous supercurrents in Sr_2RuO_4," *Phys. Rev. B.*, vol. 76, no. 1, p. 014526, 2007.

[49] C. W. Hicks, J. R. Kirtley, T. M. Lippman, N. C. Koshnick, M. E. Huber, Y. Maeno, W. M. Yuhasz, M. B. Maple, and K. A. Moler, "Limits on superconductivity-related magnetization in sr2ruo4 and pros4sb12 from scanning squid microscopy," *Phys. Rev. B.*, vol. 81, no. 21, 2010.

[50] P. G. Bjornsson, Y. Maeno, M. E. Huber, and K. A. Moler, "Scanning magnetic imaging of Sr_2RuO_4," *Phys. Rev. B.*, vol. 72, no. 1, p. 012504, 2005.

[51] C. Kallin and A. J. Berlinsky, "Is sr_2ruo_4 a chiral p-wave superconductor?," *J. Phys-Condens. Mat.*, vol. 21, no. 16, 2009.

[52] J. G. Bednorz and K. A. Müller, "Possible high T_c superconductivity in the BaLaCuO system," *Zeitschrift für Physik B Condensed Matter*, vol. 64, no. 2, pp. 189–193, 1986.

[53] T. M. Rice and M. Sigrist, "Sr2ruo4 - an electronic analog of he-3," *J. Phys-Condens. Mat.*, vol. 7, pp. L643–L648, Nov 1995.

[54] A. P. Mackenzie, R. K. W. Haselwimmer, A. W. Tyler, G. G. Lonzarich, Y. Mori, S. Nishizaki, and Y. Maeno, "Extremely strong dependence of superconductivity on disorder in sr_2ruo_4," *Phys. Rev. Lett.*, vol. 80, no. 1, p. 161, 1998.

[55] K. Ishida, H. Mukuda, Y. Kitaoka, K. Asayama, Z. Q. Mao, Y. Mori, and Y. Maeno, "Spin-triplet superconductivity in Sr_2RuO_4 identified by O-17 Knight shift," *Nature*, vol. 396, no. 6712, pp. 658–660, 1998.

[56] J. A. Duffy, S. M. Hayden, Y. Maeno, Z. Mao, J. Kulda, and G. J. McIntyre, "Polarized-Neutron Scattering Study of the Cooper-Pair Moment in Sr_2RuO_4," *Phys. Rev. Lett.*, vol. 85, no. 25, p. 5412, 2000.

[57] A. P. Mackenzie and Y. Maeno, "The superconductivity of Sr_2RuO_4 and the physics of spin-triplet pairing," *Rev. Mod. Phys.*, vol. 75, no. 2, p. 657, 2003.

[58] G. M. Luke, Y. Fudamoto, K. M. Kojima, M. I. Larkin, J. Merrin, B. Nachumi, Y. J. Uemura, Y. Maeno, Z. Q. Mao, Y. Mori, H. Nakamura, and M. Sigrist, "Time-reversal symmetry-breaking superconductivity in sr2ruo4," *Nature*, vol. 394, no. 6693, pp. 558–561, 1998.

[59] J. Xia, Y. Maeno, P. T. Beyersdorf, M. M. Fejer, and A. Kapitulnik, "High resolution polar kerr effect measurements of sr2ruo4: Evidence for broken time-reversal symmetry in the superconducting state," *Phys. Rev. Lett.*, vol. 97, no. 16, 2006.

[60] K. D. Nelson, Z. Q. Mao, Y. Maeno, and Y. Liu, "Odd-Parity Superconductivity in Sr_2RuO_4," *Science*, vol. 306, pp. 1151–1154, November 12, 2004.

[61] F. Kidwingira, J. D. Strand, D. J. Van Harlingen, and Y. Maeno, "Dynamical superconducting order parameter domains in sr_2ruo_4," *Science*, vol. 314, no. 5803, pp. 1267–1271, 2006.

[62] M. Matsumoto, "Quasiparticle states near the surface and the domain wall," *J. Phys. Soc. Jpn.*, vol. 68, no. 3, pp. 994–1007, 1999.

[63] H. Bluhm, "Magnetic fields above the surface of a superconductor with internal magnetism," *Phys. Rev. B.*, vol. 76, no. 14, p. 144507, 2007.

[64] B. J. Roth, N. G. Sepulveda, and J. John P. Wikswo, "Using a magnetometer to image a two-dimensional current distribution," *J. Appl. Phys.*, vol. 65, no. 1, pp. 361–372, 1989.

[65] M. Ichioka, Y. Matsunaga, and K. Machida, "Magnetization process in a chiral p -wave superconductor with multidomains," *Phys. Rev. B.*, vol. 71, no. 17, p. 172510, 2005.

[66] T. M. Riseman, P. G. Kealey, E. M. Forgan, A. P. Mackenzie, L. M. Galvin, A. W. Tyler, S. L. Lee, C. Ager, D. M. Paul, C. M. Aegerter, R. Cubitt, Z. Q. Mao, T. Akima, and Y. Maeno, "Observation of a square flux-line lattice in the unconventional superconductor sr2ruo4," *Nature*, vol. 396, no. 6708, pp. 242–245, 1998.

[67] C. M. Aegerter, S. H. Lloyd, C. Ager, S. L. Lee, S. Romer, H. Keller, and E. M. Forgan, "Evidence for a square vortex lattice in Sr_2RuO_4 from muon-spin-rotation measurements," *J. Phys-Condens. Mat.*, vol. 10, no. 33, pp. 7445–7451, 1998.

[68] R. Heeb and D. F. Agterberg, "Ginzburg-landau theory for a p-wave sr_2ruo_4 superconductor: Vortex core structure and extended london theory," *Phys. Rev. B.*, vol. 59, no. 10, p. 7076, 1999.

[69] Y. Maeno, S. Nishizaki, K. Yoshida, S. Ikeda, and T. Fujita, "Normal-state and superconducting properties of sr_2ruo_4," *J. Low Temp. Phys.*, vol. 105, no. 5-6, pp. 1577–1586, 1996.

[70] Z. Q. Mao, Y. Maeno, and H. Fukazawa, "Crystal growth of sr_2ruo_4," *Mater. Res. Bull.*, vol. 35, no. 11, pp. 1813–1824, 2000.

[71] K. Hasselbach, V. O. Dolocan, P. Lejay, and D. Mailly, "Observation of vortex coalescence, vortex chains and crossing vortices in the anisotropic spin-triplet superconductor Sr_2RuO_4," *Physica C*, vol. 460, pp. 277–280, 2007.

[72] J. Clem, "Simple model for vortex core in a type-ii superconductor," *J. Low Temp. Phys.*, vol. 18, no. 5-6, pp. 427–435, 1975.

[73] A. Gibbs, "Private communication," 2010.

[74] S. Raghu, A. Kapitulnik, and S. A. Kivelson, "Hidden Quasi-One-Dimensional Superconductivity in Sr_2RuO_4," *Phys. Rev. Lett.*, vol. 105, no. 13, p. 136401, 2010.

[75] R. P. Huebener, *Magnetic flux structures in superconductors : extended reprint of a classic text*. London: Springer, 2nd ed., 2001.

[76] V. Moshchalkov, M. Menghini, T. Nishio, Q. H. Chen, A. V. Silhanek, V. H. Dao, L. F. Chibotaru, N. D. Zhigadlo, and J. Karpinski, "Type-1.5 superconductivity," *Phys. Rev. Lett.*, vol. 102, no. 11, p. 117001, 2009.

[77] R. Gilardi, J. Mesot, A. J. Drew, U. Divakar, S. L. Lee, N. H. Andersen, J. Kohlbrecher, N. Momono, and M. Oda, "Field-induced hexagonal to square transition of the vortex lattice in overdoped $La_{1.8}Sr_{0.2}CuO_4$," *Physica C*, vol. 408, pp. 491–492, 2004.

[78] G. M. Luke, Y. Fudamoto, K. M. Kojima, M. I. Larkin, B. Nachumi, Y. J. Uemura, J. E. Sonier, Y. Maeno, Z. Q. Mao, Y. Mori, and D. F. Agterberg, "Unconventional superconductivity in sr2ruo4," *Physica B*, vol. 289-290, pp. 373–376, 2000.

[79] Y. Maeno, T. Ando, Y. Mori, E. Ohmichi, S. Ikeda, S. NishiZaki, and S. Nakatsuji, "Enhancement of Superconductivity of Sr_2RuO_4 to 3 K by Embedded Metallic Microdomains," *Phys. Rev. Lett.*, vol. 81, no. 17, p. 3765, 1998.

[80] K. Ishida, H. Mukuda, Y. Kitaoka, K. Asayama, Z. Q. Mao, Y. Mori, and Y. Maeno, "Spin-triplet superconductivity in Sr_2RuO_4 identified by O-17 Knight shift," *Nature*, vol. 396, no. 6712, pp. 658–660, 1998.

[81] H. Murakawa, K. Ishida, K. Kitagawa, Z. Mao, and Y. Maeno, "Measurement of the Ru-101-Knight shift of superconducting Sr_2RuO_4 in a parallel magnetic field," *Phys. Rev. Lett.*, vol. 93, Oct 2004.

[82] K. Ishida, H. Murakawa, H. Mukuda, Y. Kitaoka, Z. Q. Mao, and Y. Maeno, "NMR and NQR studies on superconducting Sr_2RuO_4," *J. Phys. Chem. Solids*, vol. 69, pp. 3108–3114, Dec 2008.

[83] Y. M. Wang, A. Zettl, S. Ooi, and T. Tamegai, "Vortex penetration into micron-sized $Bi_2Sr_2CaCu_2O_{8+\delta}$," *Phys. Rev. B*, vol. 65, no. 18, p. 184506, 2002.

[84] P. Curran, J. R. Clem, S. Bending, Y. Tsuchiya, and T. Tamegai, "Geometry-dependent penetration fields in superconducting $Bi_2Sr_2CaCu_2O_{8+\delta}$ platelets," *Phys. Rev. B.*, vol. 82, Oct 2010.

[85] E. Zeldov, A. Larkin, V. Geshkenbein, M. Konczykowski, D. Majer, B. Khaykovich, V. Vinokur, and H. Shtrikman, "Geometrical Barriers in High-Temperature Superconductors," *Phys. Rev. Lett.*, vol. 73, pp. 1428–1431, Sep 1994.

[86] J. Clem and A. Sanchez, "Hysteretic AC losses and susceptibility of thin superconducting disks," *Phys. Rev. B*, vol. 50, pp. 9355–9362, Oct 1 1994.

[87] M. Indenbom, G. Danna, M. Andre, V. Kabanov, and W. Benoit, "Edge-shape barrier irreversibility and decomposition of vortices in $Bi_2Sr_2CaCu_2O_8$," *Physica C*, vol. 235, pp. 201–204, Dec 1994.

[88] M. Benkraouda and J. Clem, "Magnetic hysteresis from the geometrical barrier in type-II superconducting strips," *Phys. Rev. B.*, vol. 53, pp. 5716–5726, Mar 1996.

[89] C. Bean, "Magnetization of hard superconductors," *Phys. Rev. Lett.*, vol. 8, no. 6, pp. 250–&, 1962.

[90] G. Blatter, M. Feigelman, V. Geshkenbein, A. Larkin, and V. Vinokur, "Vortices in high-temperature superconductors," *Rev. Mod. Phys.*, vol. 66, pp. 1125–1388, Oct 1994.

[91] M. R. Connolly, M. V. Milosevic, S. J. Bending, and T. Tamegai, "Magneto-optical imaging of flux penetration into arrays of $Bi_2Sr_2CaCu_2O_8$ microdisks," *Phys. Rev. B*, vol. 78, p. 132501, Oct 2008.

[92] V. R. Misko, B. Xu, and F. M. Peeters, "Formation and size dependence of vortex shells in mesoscopic superconducting niobium disks," *Phys. Rev. B.*, vol. 76, Jul 2007.

[93] M. R. Connolly, M. V. Milosevic, S. J. Bending, J. R. Clem, and T. Tamegai, "Continuum vs. discrete flux behaviour in large mesoscopic $Bi_2Sr_2CaCu_2O_{8+\delta}$ disks," *Euro. Phys. Lett.*, vol. 85, Jan 2009.

[94] V. Bedanov and F. Peeters, "Ordering and phase-transitions of charged particles in a classical finite 2-dimensional system," *Phys. Rev. B.*, vol. 49, pp. 2667–2676, Jan 1994.

[95] K. Deguchi, Z. Mao, and Y. Maeno, "Determination of the superconducting gap structure in all bands of the spin-triplet superconductor Sr_2RuO_4," *J. Phys. Soc. Jpn.*, vol. 73, pp. 1313–1321, May 2004.

[96] H. Suhl, B. Matthias, and L. Walker, "Bardeen-Cooper-Schrieffer Theory of Superconductivity in the case of overlapping bands," *Phys. Rev. Lett.*, vol. 3, no. 12, pp. 552–554, 1959.

[97] J. Nagamatsu, N. Nakagawa, T. Muranaka, Y. Zenitani, and J. Akimitsu, "Superconductivity at 39 K in magnesium diboride," *Nature*, vol. 410, pp. 63–64, Mar 2001.

[98] W. Pickett, "Superconductivity - Mind the double gap," *Nature*, vol. 418, pp. 733–734, Aug 2002.

[99] X. X. Xi, "Two-band superconductor magnesium diboride," *Rep. Prog. Phys.*, vol. 71, Nov 2008.

[100] V. Moshchalkov, M. Menghini, T. Nishio, Q. H. Chen, A. V. Silhanek, V. H. Dao, L. F. Chibotaru, N. D. Zhigadlo, and J. Karpinski, "Type-1.5 Superconductivity," *Phys. Rev. Lett.*, vol. 102, p. 117001, Mar 20 2009.

[101] T. Nishio, V. H. Dao, Q. Chen, L. F. Chibotaru, K. Kadowaki, and V. V. Moshchalkov, "Scanning SQUID microscopy of vortex clusters in multiband superconductors," *Phys. Rev. B.*, vol. 81, p. 020506, Jan 2010.

[102] T. Nishio, R. B. G. Kramer, V. H. Dao, L. F. Chibotaru, N. D. Zhigadlo, J. Karpinski, K. Kadowaki, and V. V. Moshchalkov, "Inhomogeneity of initial flux penetration in MgB_2 single crystals," *Physica C*, vol. 470, pp. S932–S934, Dec 2010.

[103] J. Gutierrez, B. Raes, A. V. Silhanek, L. J. Li, N. D. Zhigadlo, J. Karpinski, J. Tempere, and V. V. Moshchalkov, "Scanning Hall probe microscopy of unconventional vortex patterns in the two-gap MgB_2 superconductor," *Phys. Rev. B.*, vol. 85, p. 094511, Mar 22 2012.

[104] M. Seul and D. Andelman, "Domain shapes and patterns: The phenomenology of modulated phases," *Science*, vol. 267, no. 5197, pp. pp. 476–483, 1995.

[105] E. Babaev and M. Speight, "Semi-Meissner state and neither type-I nor type-II superconductivity in multicomponent superconductors," *Phys. Rev. B.*, vol. 72, Nov 2005.

[106] V. G. Kogan and J. Schmalian, "Ginzburg-landau theory of two-band superconductors: Absence of type-1.5 superconductivity," *Phys. Rev. B*, vol. 83, p. 054515, Feb 2011.

[107] M. Eskildsen, M. Kugler, S. Tanaka, J. Jun, S. Kazakov, J. Karpinski, and O. Fischer, "Vortex imaging in the pi band of magnesium diboride," *Phys. Rev. Lett.*, vol. 89, Oct 28 2002.

[108] S. Serventi, G. Allodi, R. De Renzi, G. Guidi, L. Romano, P. Manfrinetti, A. Palenzona, C. Niedermayer, A. Amato, and C. Baines, "Effect of two gaps on the flux-lattice internal field distribution: Evidence of two length scales in $Mg_{1-x}Al_xB_2$ from μSR," *Phys. Rev. Lett.*, vol. 93, Nov 19 2004.

[109] A. Shibata, M. Matsumoto, K. Izawa, Y. Matsuda, S. Lee, and S. Tajima, "Anomalous flux flow resistivity in the two-gap superconductor MgB_2," *Phys. Rev. B*, vol. 68, Aug 1 2003.

[110] E. Babaev, J. Carlstrom, J. Garaud, M. Silaev, and J. M. Speight, "Type-1.5 superconductivity in multiband systems: Magnetic response, broken symmetries and microscopic theory - A brief overview," *Physica C*, vol. 479, pp. 2–14, Sep 2012.

[111] A. A. Shanenko, M. V. Milošević, F. M. Peeters, and A. V. Vagov, "Extended ginzburg-landau formalism for two-band superconductors," *Phys. Rev. Lett.*, vol. 106, p. 047005, Jan 2011.

[112] L. Komendova, M. V. Milosevic, A. A. Shanenko, and F. M. Peeters, "Different length scales for order parameters in two-gap superconductors: Extended Ginzburg-Landau theory," *Phys. Rev. B*, vol. 84, Aug 2011.

[113] L. Komendova, A. A. Shanenko, M. V. Milosevic, and F. M. Peeters, "The healing lengths in two-band superconductors in extended Ginzburg-Landau theory," *Physica C*, vol. 479, pp. 126–129, Sep 2012.

[114] E. H. Brandt and M. P. Das, "Attractive Vortex Interaction and the Intermediate-Mixed State of Superconductors," *J. Supercond. Nov. Magn.*, vol. 24, pp. 57–67, Jan 2011.

[115] G. Malescio and G. Pellicane, "Stripe phases from isotropic repulsive interactions," *Nature*, vol. 2, pp. 97–100, Feb 2003.

[116] M. A. Glaser, G. M. Grason, R. D. Kamien, A. Kosmrlj, C. D. Santangelo, and P. Ziherl, "Soft spheres make more mesophases," *Euro. Phys. Lett.*, vol. 78, no. 4, 2007.

[117] E. Edlund and M. N. Jacobi, "Universality of striped morphologies," *Phys. Rev. Lett.*, vol. 105, p. 137203, Sep 2010.

[118] H. J. Zhao, V. R. Misko, and F. M. Peeters, "Vortex configurations with non-monotonic interaction," *Physica C*, vol. 479, pp. 130–133, Sep 2012.

[119] C. J. O. Reichhardt, C. Reichhardt, and A. R. Bishop, "Structural transitions, melting, and intermediate phases for stripe- and clump-forming systems," *Phys. Rev. E.*, vol. 82, Oct 22 2010.

[120] C. Reichhardt, J. Drocco, C. J. O. Reichhardt, and A. R. Bishop, "The effect of pinning on vortex states with attractive and repulsive interactions," *Physica C*, vol. 479, pp. 15–18, Sep 2012.

[121] A. J. M. van Erven, T. H. Kim, M. Muenzenberg, and J. S. Moodera, "Highly crystallized as-grown smooth and superconducting MgB_2 films by molecular-beam epitaxy," *App. Phys. Lett.*, vol. 81, no. 26, pp. 4982–4984, 2002.

[122] J.-B. Laloe, T. H. Kim, and J. S. Moodera, "Molecular-Beam Epitaxially Grown MgB_2 Thin Films and Superconducting Tunnel Junctions," *Adv. Cond. Matt. Phys.*, 2011.

[123] U. Welp, A. Rydh, G. Karapetrov, W. Kwok, G. Crabtree, C. Marcenat, L. Paulius, L. Lyard, T. Klein, J. Marcus, S. Blanchard, P. Samuely, P. Szabo, A. Jansen, K. Kim, C. Jung, H. Lee, B. Kang, and S. Lee, "Superconducting phase diagram of single-crystal MgB_2," *Physica C*, vol. 385, pp. 154–161, Mar 2003.

[124] S. Lee, T. Masui, H. Mori, Y. Eltsev, A. Yamamoto, and S. Tajima, "Crystal growth and characterization of MgB_2: the relation between structural and superconducting properties," *Supercond. Sci. Technol.*, vol. 16, pp. 213–220, Feb 2003.

[125] S. Kazakov, R. Puzniak, K. Rogacki, A. Mironov, N. Zhigadlo, J. Jun, C. Soltmann, B. Batlogg, and J. Karpinski, "Carbon substitution in MgB_2 single crystals: Structural and superconducting properties," *Phys. Rev. B.*, vol. 71, p. 024533, Jan 2005.

[126] M. Badr and K. Ng, "A new heat treatment to prepare high-quality polycrystalline and single crystal MgB_2 in a single process," *Supercond. Sci. Technol.*, vol. 16, pp. 668–671, Jun 2003.

[127] P. Canfield, D. Finnemore, S. Bud'ko, J. Ostenson, G. Lapertot, C. Cunningham, and C. Petrovic, "Superconductivity in dense MgB_2 wires," *Phys. Rev. Lett*, vol. 86, pp. 2423–2426, Mar 12 2001.

[128] M. Jung, M. Jaime, A. Lacerda, G. Boebinger, W. Kang, H. Kim, E. Choi, and S. Lee, "Anisotropic superconductivity in epitaxial MgB_2 films," *Chem. Phys. Lett.*, vol. 343, pp. 447–451, Aug 10 2001.

[129] H. Yang, Y. Liu, C. Zhuang, J. Shi, Y. Yao, S. Massidda, M. Monni, Y. Jia, X. Xi, Q. Li, Z.-K. Liu, Q. Feng, and H.-H. Wen, "Fully Band-Resolved Scattering Rate in MgB_2 Revealed by the Nonlinear Hall Effect and Magnetoresistance Measurements," *Phys. Rev. Lett.*, vol. 101, p. 067001, Aug 2008.

[130] J. An and W. Pickett, "Superconductivity of MgB_2: Covalent bonds driven metallic," *Phys. Rev. Lett.*, vol. 86, pp. 4366–4369, May 7 2001.

[131] J. Kortus, I. Mazin, K. Belashchenko, V. Antropov, and L. Boyer, "Superconductivity of metallic boron in MgB_2," *Phys. Rev. Lett.*, vol. 86, pp. 4656–4659, May 14 2001.

[132] F. Bouquet, R. Fisher, N. Phillips, D. Hinks, and J. Jorgensen, "Specific heat of (MgB)-B-11: Evidence for a second energy cap," *Phys. Rev. Lett.*, vol. 87, Jul 23 2001.

[133] Y. Wang, T. Plackowski, and A. Junod, "Specific heat in the superconducting and normal state (2-300 K, 0-16 T), and magnetic susceptibility of the 38 K superconductor MgB_2: evidence for a multicomponent gap," *Physica C*, vol. 355, pp. 179–193, Jun 15 2001.

[134] E. A. Yelland, J. R. Cooper, A. Carrington, N. E. Hussey, P. J. Meeson, S. Lee, A. Yamamoto, and S. Tajima, "de Haas-van Alphen Effect in Single Crystal MgB_2," *Phys. Rev. Lett.*, vol. 88, p. 217002, May 2002.

[135] J. Cooper, A. Carrington, P. Meeson, E. Yelland, N. Hussey, L. Balicas, S. Tajima, S. Lee, S. Kazakov, and J. Karpinski, "de Haasvan Alphen effect in MgB_2 crystals," *Physica C*, vol. 385, no. 12, pp. 75 – 84, 2003.

[136] A. Carrington, P. J. Meeson, J. R. Cooper, L. Balicas, N. E. Hussey, E. A. Yelland, S. Lee, A. Yamamoto, S. Tajima, S. M. Kazakov, and J. Karpinski, "Determination of the Fermi Surface of MgB_2 by the de Haas-van Alphen Effect," *Phys. Rev. Lett.*, vol. 91, p. 037003, Jul 2003.

[137] J. D. Fletcher, A. Carrington, S. M. Kazakov, and J. Karpinski, "Damping of the de Haas-van Alphen oscillations in the superconducting state of MgB_2," *Phys. Rev. B*, vol. 70, p. 144501, Oct 2004.

[138] A. Carrington, J. D. Fletcher, J. R. Cooper, O. J. Taylor, L. Balicas, N. D. Zhigadlo, S. M. Kazakov, J. Karpinski, J. P. H. Charmant, and J. Kortus, "de Haas-van Alphen effect investigation of the electronic structure of Al-substituted MgB_2," *Phys. Rev. B*, vol. 72, p. 060507, Aug 2005.

[139] I. Horcas, R. Fernández, J. M. Gómez-Rodríguez, J. Colchero, J. Gómez-Herrero, and A. M. Baro, "Wsxm: A software for scanning probe microscopy and a tool for nanotechnology," *Rev. Sci. Instrum.*, vol. 78, no. 1, p. 013705, 2007.

[140] A. Larkin and Y. Ovchinnikov, "Pinning in Type-II Superconductors," *J. Low Temp. Phys.*, vol. 34, no. 3-4, pp. 409–428, 1979.

[141] M. Eisterer, "Magnetic properties and critical currents of MgB_2," *Supercond. Sci. Technol.*, vol. 20, pp. R47–R73, Dec 2007.

[142] E. H. Brandt, "The Flux-Line-Lattice in Superconductors," *Rep. Prog. Phys.*, vol. 58, pp. 1465–1594, Nov 1995.

[143] X. B. Xu, H. Fangohr, S. Y. Ding, F. Zhou, X. N. Xu, Z. H. Wang, M. Gu, D. Q. Shi, and S. X. Dou, "Phase diagram of vortex matter of type-ii superconductors," *Phys. Rev. B*, vol. 83, p. 014501, Jan 2011.

[144] X. B. Xu, H. Fangohr, Z. H. Wang, M. Gu, S. L. Liu, D. Q. Shi, and S. X. Dou, "Vortex dynamics for low-κ type-ii superconductors," *Phys. Rev. B*, vol. 84, p. 014515, Jul 2011.

[145] U. Krageloh, "Der zwischenzustand bei supraleitern zweiter art," *Phys. Status Solidi (b)*, vol. 42, no. 2, pp. 559–576, 1970.

[146] S.-Z. Lin and X. Hu, "Vortex states and the phase diagram of a multiple-component ginzburg-landau theory with competing repulsive and attractive vortex interactions," *Phys. Rev. B*, vol. 84, p. 214505, Dec 2011.

[147] E. Brandt, "Static properties of Type-II superconducters at arbitrary temperature and induction," *Phys. Lett. A*, vol. A 51, no. 1, pp. 39–41, 1975.

[148] M. Leung, "Attractive interaction between vortices in Type-II superconductors at arbitrary temperatures," *J. Low Temp. Phys.*, vol. 12, no. 1-2, pp. 215–235, 1973.

[149] A. Buzdin and A. Simonov, "Peculiar magnetic properties of anisotropic london superconductors," *Physica C*, vol. 168, no. 34, pp. 421 – 425, 1990.

[150] E. Brandt, R. Mints, and I. Snapiro, "Long-range fluctuation-induced attraction of vortices to the surface in layered superconductors," *Phys. Rev. Lett.*, vol. 76, pp. 827–830, Jan 29 1996.

[151] G. Blatter and V. Geshkenbein, "van der Waals attraction of vortices in anisotropic and layered superconductors," *Phys. Rev. Lett.*, vol. 77, pp. 4958–4961, Dec 9 1996.

[152] S. Mukherji and T. Nattermann, "Steric repulsion and van der Waals attraction between flux lines in disordered high T-c superconductors," *Phys. Rev. Lett.*, vol. 79, pp. 139–142, Jul 7 1997.

[153] H. Weber, E. Seidl, M. Botlo, C. Laa, E. Mayerhofer, F. Sauerzopf, R. Schalk, H. Wiesinger, and J. Rammer, "Magnetization of low-κ superconductors .1. The phase-transtion at HCL," *Physica C*, vol. 161, pp. 272–286, Nov 15 1989.

[154] G. Eilenberger and H. Buttner, "Structure of single vortices in type-2 superconductors," *Z. Phys.*, vol. 224, no. 4, pp. 335–&, 1969.

[155] M. Leung and A. Jacobs, "Asymptotic behaviour of vector potential and order parameter for an isolated vortex," *J. Low. temp. Phys.*, vol. 11, no. 3-4, pp. 395–419, 1973.

[156] A. Grigorenko, S. Bending, I. Grigorieva, A. Koshelev, T. Tamegai, and S. Ooi, "Tilt of pancake vortex stacks in layered superconductors in the crossing lattice regime," *Phys. Rev. Lett.*, vol. 94, Feb 18 2005.

[157] P. Gammel, D. Bishop, J. Rice, and D. Ginsberg, "Images of the vortex chain state in untwinned $YBa_2Cu_3O_{7-\delta}$," *Phys. Rev. Lett.*, vol. 68, pp. 3343–3346, Jun 1 1992.

[158] S. Bending and M. Dodgson, "Vortex chains in anisotropic superconductors," *J. Phys.: Condens. Matter*, vol. 17, pp. R955–R993, Sep 7 2005.

[159] M. Zehetmayer, M. Eisterer, J. Jun, S. Kazakov, J. Karpinski, A. Wisniewski, and H. Weber, "Mixed-state properties of superconducting MgB2 single crystals," *Phys. Rev. B*, vol. 66, Aug 1 2002.

[160] J. Carlstrom, E. Babaev, and M. Speight, "Type-1.5 superconductivity in multiband systems: Effects of interband couplings," *Phys. Rev. B*, vol. 83, May 11 2011.

[161] M. Tinkham, *Introduction to superconductivity*. Dover Publications, 2^{nd} ed., 2004.

[162] I. I. Mazin, O. K. Andersen, O. Jepsen, O. V. Dolgov, J. Kortus, A. A. Golubov, A. B. Kuzmenko, and D. van der Marel, "Superconductivity in MgB_2: Clean or Dirty?," *Phys. Rev. Lett.*, vol. 89, p. 107002, Aug 2002.

[163] A. Brinkman, A. A. Golubov, H. Rogalla, O. V. Dolgov, J. Kortus, Y. Kong, O. Jepsen, and O. K. Andersen, "Multiband model for tunneling in MgB_2 junctions," *Phys. Rev. B*, vol. 65, p. 180517, May 2002.

[164] G. Rubio-Bollinger, H. Suderow, and S. Vieira, "Tunneling Spectroscopy in Small Grains of Superconducting MgB_2," *Phys. Rev. Lett.*, vol. 86, pp. 5582–5584, Jun 2001.

[165] M. R. Eskildsen, M. Kugler, S. Tanaka, J. Jun, S. M. Kazakov, J. Karpinski, and O. Fischer, "Vortex imaging in the π band of magnesium diboride," *Phys. Rev. Lett.*, vol. 89, p. 187003, Oct 2002.

[166] A. A. Golubov, J. Kortus, O. V. Dolgov, O. Jepsen, Y. Kong, O. K. Andersen, B. J. Gibson, K. Ahn, and R. K. Kremer, "Specific heat of MgB_2 in a one- and a two-band model from first-principles calculations," *J. Phys. Cond. Matter*, vol. 14, no. 6, p. 1353, 2002.

[167] H. Choi, D. Roundy, H. Sun, M. Cohen, and S. Louie, "The origin of the anomalous superconducting properties of MgB_2," *Nature*, vol. 418, pp. 758–760, Aug 15 2002.

[168] M. Silaev and E. Babaev, "Microscopic derivation of two-component Ginzburg-Landau model and conditions of its applicability in two-band systems," *Phys. Rev. B*, vol. 85, Apr 16 2012.

[169] M. Silaev and E. Babaev, "Microscopic theory of type-1.5 superconductivity in multiband systems," *Phys. Rev. B*, vol. 84, Sep 15 2011.

[170] E. Babaev, J. Carlström, and M. Speight, "Type-1.5 superconducting state from an intrinsic proximity effect in two-band superconductors," *Phys. Rev. Lett.*, vol. 105, p. 067003, Aug 2010.

[171] C. P. Bean and J. D. Livingston, "Surface Barrier in Type-II Superconductors," *Phys. Rev. Lett.*, vol. 12, no. 1, p. 14, 1964.

[172] L. Burlachkov, "Magnetic-relaxation over the Bean-Livingston surface-barrier," *Phys. Rev. B.*, vol. 47, pp. 8056–8064, Apr 1993.

[173] L. Burlachkov, V. Geshkenbein, A. Koshelev, A. Larkin, and V. Vinokur, "Giant flux-creep through surface barriers and the irreversibility line in high-temperature superconductors," *Phys. Rev. B.*, vol. 50, pp. 16770–16773, Dec 1994.

[174] D. Craik, *Magnetism principles and applications.* Wiley, 1^{st} ed., 1995.

[175] S. Ooi, T. Shibauchi, and T. Tamegai, "Evolution of vortex phase diagram with oxygen-doping in $Bi_2Sr_2CaCu_2O_{8+y}$ single crystals," *Physica C*, vol. 302, pp. 339–345, Jul 1998.

[176] L. Bulaevskii, M. Ledvij, and V. Kogan, "Vortices in layered superconductors with josephson coupling," *Phys. Rev. B.*, vol. 46, pp. 366–380, Jul 1992.

[177] V. Kopylov, A. Koshelev, I. Schegolev, and T. Togonidze, "The role of surface effects in magnetization of high-Tc superconductors," *Physica C*, vol. 170, pp. 291–297, Sep 1990.

[178] M. James, S. Stoddart, S. Bending, S. Aukkaravittayapun, P. King, and M. Henini, "Field penetration and surface barriers in superconducting $Bi_2Sr_2CaCu_2O_{8+\delta}$ whiskers," *Phys. Rev. B.*, vol. 56, pp. R5771–R5773, Sep 1997.

[179] R. Doyle, S. Rycroft, C. Dewhurst, E. Zeldov, I. Tsabba, S. Reich, T. Doyle, T. Tamegai, and S. Ooi, "The effect of sample shape on the magnetisation in $Bi_2Sr_2CaCu_2O_{8+\delta}$ crystals," *Physica C*, vol. 308, pp. 123–131, Nov 1998.

[180] Lynton, *Superconductivity.* London: Methuen, 1962.

[181] Geshkenbein, VB and Larkin, AI, "Private communication."

[182] A. Aharoni, "Demagnetizing factors for rectangular ferromagnetic prisms," *J. Appl. Phys.*, vol. 83, pp. 3432–3434, Mar 1998.

[183] M. Beleggia, M. De Graef, and Y. Millev, "The equivalent ellipsoid of a magnetized body," *J. Phys. D. Appl. Phys.*, vol. 39, pp. 891–899, Mar 2006.

[184] E. Pardo, D. Chen, and A. Sanchez, "Demagnetizing factors for completely shielded rectangular prisms," *J. Appl. Phys.*, vol. 96, pp. 5365–5369, Nov 2004.

[185] D. X. Chen, E. Pardo, and A. Sanchez, "Fluxmetric and magnetometric demagnetizing factors for cylinders," *J. Magn. Magn. Mater.*, vol. 306, pp. 135–146, Nov 2006.

[186] D. Craik, "Demagnetizing fields in uniformly magnetized rectangular prismatic crystals," *Brit. J. Appl. Phys.*, vol. 18, no. 9, pp. 1355–&, 1967.

[187] G. Berdiyorov, L. Cabral, and F. Peeters, "Surface barrier for flux entry and exit in mesoscopic superconducting systems," *J. Math. Phys.*, vol. 46, Sep 2005.